

# UC Riverside

## UC Riverside Electronic Theses and Dissertations

### Title

Nanomaterials Engineering and Applications in Catalysis

### Permalink

<https://escholarship.org/uc/item/5kd4q6xc>

### Author

Zhang, Qiao

### Publication Date

2012

Peer reviewed|Thesis/dissertation

UNIVERSITY OF CALIFORNIA  
RIVERSIDE

Nanomaterials Engineering and Applications in Catalysis

A Dissertation submitted in partial satisfaction  
of the requirements for the degree of

Doctor of Philosophy

in

Chemistry

by

Qiao Zhang

June 2012

Dissertation Committee:

Dr. Yadong Yin, Chairperson

Dr. Christopher Bardeen

Dr. Leonard Mueller

Copyright by  
Qiao Zhang  
2012

This Dissertation of Qiao Zhang is approved:

---

---

---

Committee Chairperson

University of California, Riverside

## **Acknowledgements**

Though only my name appears on the cover of this dissertation, I could never have reached the heights or explored the depths and finished my Ph. D. study smoothly without the help, support, guidance and efforts of a lot of people.

First, my deepest gratitude is to my mentor Dr. Yadong Yin for his careful guidance and infectious enthusiasm. Yadong is a fantastic advisor, a perfect friend and a role model. His endless patience and strong support helped me overcome many crisis situations in both my scientific research and daily life. His insightful and knowledgeable guidance made my graduate period more productive. I hope that I can become as good an advisor to my students as Yadong has been to me in the future.

I am also thankful to my committee members Professor Christopher J. Bardeen and Professor Leonard Mueller for their help and valuable comments on my dissertation.

I am greatly indebted to many past and current members in Yin group for providing a rich working experience, intellectual stimulation and friendship: Dr. Jianping Ge, Dr. Tierui Zhang, Dr. Yongxing Hu, Zhenda Lu, Le He, Dr. Xiaogang Han, Dr. Wenshou Wang, Dr. Chuanbo Gao, Dr. Jibong Joo, James Goebel, Michael Dahl, Mingsheng Wang, Yiding Liu, Dr. Yan Wang, Dr. Miaomiao Ye, Dr. Chunguang Li, Junxiang Fu, Dr. Lei Sun, Qipeng Lu, Jiemei Lei, and Dr. Geonda Moon.

I would like to give my special thanks to those who have worked with me closely in the lab: visiting scholars Diana Q. Lima (from Brazil), Na Li and Hongxia Yu (from China), high school student Michael Janner, and undergraduate students Tri Pham and Austin Lee. I must thank Dr. Yu Lu for her kind assistance in both scientific research and daily life.

I would like to take this opportunity to thank Dr. Ilkeun Lee and Prof. Francisco Zaera for their great help in the collaboration of catalysis project at UCR. My thanks also go to Dr. Miaofang Chi for her help in some data collection and analysis in Oak Ridge National Lab. I thank Dr. Krassimir N. Bozhilov and Stephen McDaniel for their kind assistance in using facilities in CFAMM at UCR. My thanks also go to my friends Shirui Guo and Tao Wu for their valuable help.

Most importantly, none of this would have been possible without the love and patience of my family. I would like to express my heart-felt gratitude to my grandparents Jinhai Zhang and Shuzheng Deng, my parents Daogui Pan and Chenglan Zhang, my parents-in-law Xinmin Zhang and Zhenghua Xiao, my wife Xiaojie Zhang, my sister Rong Zhang, and my daughters Amanda and Elaine for everything they have done for me.

Finally, I would like to take the opportunity to thank all persons who have ever helped me before.

## **Dedication**

*To my wife Xiaojie and my little angels Amanda and Elaine.*

## ABSTRACT OF THE DISSERTATION

Nanomaterials Engineering and Applications in Catalysis

by

Qiao Zhang

Doctor of Philosophy, Graduate Program in Chemistry

University of California, Riverside, June 2012

Dr. Yadong Yin, Chairperson

Catalysis plays an essential role in industrial applications of direct relevance to many aspects in our daily lives, such as petroleum refining, fine chemical and pharmaceutical production, energy conversion and storage, and automotive emissions control. Design and fabrication of highly active catalysts in an efficient and cost-effective way is thus an important topic. This dissertation discusses our efforts in the engineering and applications of nanomaterials, which could be divided into three consecutive stages: (1) synthesis, (2) stabilization, and (3) application in catalysis.

In the first stage, by using Ag nanoplates as a model system, we attempt to outline the key components that determine the formation of nanomaterials with desired morphology, clarify the roles of each reagent, provide highly reproducible recipes for synthesis, and therefore take a significant step towards the complete understanding of the mechanism behind the experimental phenomena. Using this understanding, Ag nanoplates with various aspect ratios and widely tunable SPR bands have been successfully obtained.



One of the major challenges for the use of nanostructured materials as catalysts is their chemical and structural stability. In the second stage, by embedding nanocatalysts within a mesoporous metal oxide shell, we are able to prepare nanocatalysts with enhanced stability in both gas and aqueous phase reactions. A general strategy, called the “surface-protected etching” process, has been developed as the major synthetic tool for producing mesoporous shells for the stabilization of noble metal nanocatalysts. A sandwich-like structure was further proposed, in which multi-functional materials could be incorporated to make recyclable and highly efficient catalysts.

Finally, for practical applications, TiO<sub>2</sub>-based nanomaterials have been used as the model system to investigate the factors that determine the preparation of efficient photocatalysts. Mesoporous TiO<sub>2</sub> photocatalysts with high surface area and high photocatalytic activity have been prepared through a self-assembly approach. Based on our improved understanding of photocatalysts, we have designed and synthesized a highly efficient, stable, and cost-effective TiO<sub>2</sub>-based photocatalyst by combining both non-metal doping and noble metal decoration. The new photocatalysts show excellent performance in degradation reactions of a number of organic compounds under the irradiation of UV, visible, and direct sunlight.

## Table of Contents

Acknowledgement.....	iv
Dedication.....	vi
Abstract.....	vii
List of Tables.....	xii
List of Figures.....	xiii
List of Schemes.....	xx
<b>Chapter 1 Overview of Engineering and Applications of Nanomaterials.....</b>	<b>1</b>
1.1 Introduction.....	1
1.2 The Impact of Nanotechnology on Catalysis.....	4
1.2.1 The History of Nanotechnology.....	4
1.2.2 Physicochemical Properties of Nanostructured Materials.....	7
1.2.3 Size-Dependent Catalytic Activity of Nanomaterials.....	10
1.2.4 Shape-Dependent Catalytic Activity of Nanomaterials.....	13
1.2.5 Plasmonic Nanomaterials.....	16
1.2.6 TiO <sub>2</sub> -Based Photocatalysts.....	22
1.3 Colloidal Synthesis of Silver Nanoplates.....	26
1.5 Challenges in Utilizing Nanomaterials.....	31
1.6 Scope of This Work.....	33
1.7 References.....	36
<b>Chapter 2 Silver Nanoplates: Synthesis, Engineering, and Stabilization.....</b>	<b>44</b>
2.1 Introduction.....	44
2.2 Materials and Methods.....	49
2.3 A Systematic Study on the Synthesis of Silver Nanoplates.....	52

2.4	Seeded-Growth of Uniform Silver Nanoplates with Tunable Plasmon Band.....	74
2.5	Reconstruction of Silver Nanoplates by UV Irradiation.....	86
2.6	Conclusion.....	96
2.7	References.....	99
<b>Chapter 3</b>	<b>Surface-Protected Etching of Mesoporous Oxide Shells for the Stabilization of Noble Metal Nanocatalysts.....</b>	<b>104</b>
3.1	Introduction.....	104
3.2	Materials and Methods.....	111
3.3	Permeable Silica Shell through Surface-Protected Etching.....	117
3.4	Core–Satellite Nanocomposite Catalysts Protected by a Porous Silica Shell.....	130
3.5	Catalysis in Gas Phase.....	140
3.6	Conclusion.....	149
3.7	References.....	152
<b>Chapter 4</b>	<b>Engineering TiO<sub>2</sub> Nanomaterials for Photocatalytic Applications....</b>	<b>159</b>
4.1	Introduction.....	159
4.2	Materials and Methods.....	163
4.3	Self-Assembled TiO <sub>2</sub> Nanocrystal Cluster and Its Photocatalytic Applications.....	168
4.4	Highly Active TiO <sub>2</sub> -Based Visible-Light Photocatalyst with Nonmetal Doping and Plasmonic Metal Decoration.....	187
4.5	Conclusion.....	200
4.6	References.....	202

<b>Chapter 5 Conclusion and Outlook</b> .....	206
5.1 Conclusion of this Dissertation.....	206
5.2 Outlook and Future Work.....	209
5.3 References.....	210

## **List of Tables**

- Table 1.1** Surface area and surface energy as a function of particle size.
- Table 2.1** Carboxyl compounds with different numbers of carboxylate groups and chain lengths that have been used as the capping agent to prepare silver nanoplates.

## List of Figures

- Figure 1.1** Digital images of the Lycurgus Cup at the British Museum, lit from the outside (a) and from the inside (b).
- Figure 1.2** The percentage of surface atoms changes with the palladium cluster diameter.
- Figure 1.3** CO oxidation turnover frequencies (TOFs) at 300 K as a function of the average size of the Au clusters supported on a high surface area TiO<sub>2</sub> support. The Au/TiO<sub>2</sub> catalysts were prepared by deposition-precipitation method, and the average cluster diameters were measured by TEM. The solid line serves merely to guide the eye.
- Figure 1.4** Image showing the shape-dependent catalytic selectivity using the catalytic isomerization of 2-butenes in the presence of Pt nanocatalysts as the model system.
- Figure 1.5** Digital image of colloidal silver nanoplates with different colors.
- Figure 2.1** (a) UV/Vis spectra of silver nanoparticles synthesized in different conditions; (b-d) TEM images showing the morphology of products prepared in the presence of (b) PVP only, (c) PVP and H<sub>2</sub>O<sub>2</sub>, and (d) PVP, citrate, and H<sub>2</sub>O<sub>2</sub> together. The inset in (d) shows a TEM image in which Ag nanoplates stand vertically upon their edges.
- Figure 2.2** (a) UV/Vis spectra of silver nanoparticles obtained by controlling the concentration of H<sub>2</sub>O<sub>2</sub>; (b) real-time measurement of the formation of silver nanoplates with a time interval of 7.5 s. The inset in (b) shows the UV/Vis spectra of the initiation stage during the synthesis of silver nanoplates with a time interval of 0.75 s.
- Figure 2.3** UV/Vis spectra and TEM images showing that both (a-c) silver nanowires with lengths of up to 10 μm and (d-f) silver nanoparticles with irregular shapes can be converted to silver nanoplates in the presence of H<sub>2</sub>O<sub>2</sub>.
- Figure 2.4** The yield of silver nanoplates as a function of the number of carbon atoms between two nearest carboxylate groups when carboxyl compounds are used as the capping agent.

- Figure 2.5** (a) UV/Vis spectra and (b) TEM image showing the preparation of silver nanoplates by using citrate as the sole surfactant; (c) UV/Vis spectra of Ag nanoplates prepared by using PVP as an additional stabilizing agent; (d, e) UV/Vis spectra and digital image of silver nanoplates prepared in the presence of glycerol by tuning the synthetic conditions.
- Figure 2.6** (a) The initiation time and (b) thickness and aspect ratio of as-obtained silver nanoplates as a function of the concentration of  $\text{NaBH}_4$ .
- Figure 2.7** (a) TEM image of the original silver nanoplate seeds; (b-f) SEM images showing the evolution process of Ag nanoplates during the step-wise growth process.
- Figure 2.8** Plots of the standard deviation of the size distribution as a function of the edge length. The inset shows the plots of edge length of Ag nanoplates as a function of the number of cycles of seeded growth.
- Figure 2.9** (a-d) TEM images showing the size evolution process of Ag nanoplates. The insets show the corresponding selected area electron diffraction (SAED) patterns obtained by aligning the electron beam perpendicular to the basal surfaces of an individual nanoplate.
- Figure 2.10** AFM images showing the thickness evolution of representative samples, (a)  $\sim 570$  nm and (b)  $\sim 4$   $\mu\text{m}$ , during the seeded growth process; (c, d): The plots of the change in thickness (c) and aspect ratio (d) as a function of the change in edge length.
- Figure 2.11** UV-Vis-NIR spectra showing the size evolution process of Ag nanoplates.
- Figure 2.12** (a) Schematic illustration of the evolution process of Ag nanoplates under UV-light irradiation: the sharp corner of triangular plates disappears, while the thickness of the nanoplates increases. (b, c) Digital photographs and extinction spectra showing the backward tuning of the optical property of the silver nanoplates by irradiation under UV light for different times. From right to left, the samples displayed in the photo were irradiated for 0, 60, 70, 80, 90, 100, 110, and 125 min, while the spectra were taken after irradiating the nanoplate solutions for 0, 20, 40, 60, 70, 80, 90, 100, 110, and 125 min.

- Figure 2.13** TEM images showing the shape evolution of Ag nanoplates upon UV irradiation for (a) 0 min, (c) 40 min, (d) 80 min, and (e) 125 min. Images of (b) and (f) are selected area electron diffraction patterns taken from a single particle (inset) corresponding to samples of (a) and (e), respectively. Scale bars are 50 nm.
- Figure 2.14** (a-e) TEM images showing the thickness evolution of Ag nanoplates upon UV irradiation for (a) 0 min,  $3.08 \pm 0.57$  nm; (b) 30 min,  $4.15 \pm 0.52$  nm; (c) 60min,  $5.16 \pm 0.47$  nm; (d) 90 min,  $7.24 \pm 0.78$  nm; (e) 125 min,  $8.6 \pm 1.08$  nm. All scale bars are 50 nm. (f) Summary plot showing the change of nanoplate thickness over irradiation time.
- Figure 2.15** Comparison of the stability in optical property for nanoplates with and without UV irradiation: (a) The plasmon bands of Ag nanoplates without UV treatment blue-shift over time. The synthetic condition was altered to obtain samples with four different plasmon bands. (b) The plasmon bands of the UV-irradiated Ag nanoplates remain stable over time. The samples with different plasmon bands were produced by irradiating the same original plate solution for different periods.
- Figure 3.1** (a) Dependence of PVP loading (left) and the relative stability against NaOH etching (right) of SiO<sub>2</sub> spheres on the refluxing time of SiO<sub>2</sub>/PVP mixture. (b) The weight loss of the PVP treated SiO<sub>2</sub> spheres after etching with NaOH for various periods. (c) TGA curves of pure silica (blue), PVP treated silica (red), and silica spheres after protected etching for 3hrs (green). The PVP treated silica particles used in (b) and (c) have been refluxed in an aqueous solution of PVP for 3hrs.
- Figure 3.2** TEM images showing the morphology of PVP-treated SiO<sub>2</sub> particles after etching by NaOH for (a) 0hr; (b) 1hr; (c) 2hr 45min; and (d) 3hr. Before etching, the silica particles have been refluxed in an aqueous solution of PVP for 3hrs. The outer diameter of the particles changes only slightly from  $436 \pm 16$  nm in sample (a) to  $430 \pm 22$  nm in sample (d).
- Figure 3.3** TEM images showing the structure evolution of Au@SiO<sub>2</sub> core-shell particles: (a) the original samples; and (b-d) the samples after etching by NaOH for (b) 2hr; (c) 2hr 45min; and (d) 3hr. The average outer diameters of the particles are: (a)  $180 \pm 12$ nm, (b)  $180 \pm 16$ nm; (c)  $180 \pm 16$ nm, and (d)  $178 \pm 24$  nm. Before etching, the silica particles have been refluxed in an aqueous solution of PVP for 3hrs. All scale bars are 200 nm.



- Figure 3.4** (a) UV-Vis spectra showing reduction of 4-NP. (b) Conversion of 4-NP using Au@SiO<sub>2</sub> catalyst after etching for: ■ 0 min; ● 90 min; ▲ 2 hr; ▼ 150 min; ◆ 165 min; and ◀ 3 hr. (c) Conversion of 4-NP in twelve successive cycles of reduction with: ★Au@SiO<sub>2</sub>; and ● bare Au nanoparticles.
- Figure 3.5** (a) Schematic illustration of the synthetic procedure used for the formation of SiO<sub>2</sub>/Au/SiO<sub>2</sub> sandwiched nanoreactor structures. (b, c) TEM images of the sandwiched structures (b) before, and (c) after surface-protected etching. Note that superparamagnetic Fe<sub>3</sub>O<sub>4</sub> particles were included at the core of the samples in (b) and (c) for enhanced recyclability.
- Figure 3.6** TEM images of Fe<sub>3</sub>O<sub>4</sub>/SiO<sub>2</sub>/Au/porous-SiO<sub>2</sub> composite colloids collected after different periods: a) 50; b) 65; c) 85; and d) 95 min.
- Figure 3.7** N<sub>2</sub> adsorption/desorption isotherms for the nanocomposite particles displayed in 5 b) and 5 c), respectively. Insets show the corresponding BJH pore size distributions.
- Figure 3.8** (a-e) TEM images of Au nanoparticles supported on Fe<sub>3</sub>O<sub>4</sub>@SiO<sub>2</sub> core-shell spheres without (a, b) and with (d, e) porous SiO<sub>2</sub> shells before (a, d) and after (b, e) catalyzing the liquid-phase reduction reaction of 4-NP by NaBH<sub>4</sub>. (c, f) Conversion of 4-NP as a function of reaction time in six successive cycles of reduction and magnetic recycling using Fe<sub>3</sub>O<sub>4</sub>/SiO<sub>2</sub>/Au (c) and Fe<sub>3</sub>O<sub>4</sub>/SiO<sub>2</sub>/Au/porous SiO<sub>2</sub> (f) core-satellite composite catalysts.
- Figure 3.9** (a-c) TEM images of SiO<sub>2</sub>/Pt/SiO<sub>2</sub> composite particles after etching for (a, d) 0 min, (b, e) 40 min, and (c, f) 60 min, before (a-c) and after (d-f) pretreatment following three oxidation-reduction cycles at 350 °C.
- Figure 3.10** (a-c) Transmission IR absorption spectra of CO adsorbed on Pt nanoparticles dispersed on silica beads and coated with a layer of mesoporous silica deposited afterwards, as explained in the text. Data are reported for the catalysts before etching (a, **E0**) and after etching for 40 min (b, **E40**) and 60 min (c, **E60**), respectively. (d) Peak areas of the peak due to the C–O stretching vibrational mode,  $\nu(\text{CO})$ , of CO adsorbed linearly on-top of single Pt atoms within the Pt nanoparticles. The peak area data are reported for all three catalysts as a function of catalyst temperature.

- Figure 3.11** Kinetics of hydrogenation for (a) *cis*-2-butene and (b) *trans*-2-butene to butane with our Pt catalysts, in the form of product accumulation in the batch reactor as a function of time of reaction. Data are provided for SiO<sub>2</sub>/Pt/SiO<sub>2</sub> catalysts unetched (**E0**), and after etching for 40 min (**E40**), and 60 min (**E60**), respectively.
- Figure 3.12** TEM images of Pt nanoparticle/SiO<sub>2</sub> bead catalysts, "naked" (i. e., uncovered, top row) and covered with a layer of mesoporous silica (bottom row) after calcination at, from left to right, 300, 875, 975, and 1075 K. Sintering is already significant by 875 K in the naked samples, whereas no appreciable sintering is observed in the encapsulated samples even after calcination at 1075 K.
- Figure 4.1** TEM images showing the preparation process of TiO<sub>2</sub> nanocrystal clusters: (a) TiO<sub>2</sub> nanoparticles; (b) self-assembled TiO<sub>2</sub> clusters; (c) SiO<sub>2</sub> coated TiO<sub>2</sub> clusters; (d) TiO<sub>2</sub> clusters after calcination of (c) at 400 °C for 1 hour and subsequently removal SiO<sub>2</sub> shell by etching in NaOH. The insets in b and d are higher magnification images of nanocrystal clusters.
- Figure 4.2** (a) XRD patterns of self-assembled TiO<sub>2</sub> clusters after calcination at different temperatures: 350 °C (TC350), 400 °C (TC400), 450 °C (TC450), and 500 °C (TC500). The black curve was measured from a sample prepared without calcination. All samples were prepared by sequential steps of self-assembly in emulsion droplets, silica coating, calcination, and silica etching. (b) XRD patterns of self-assembled TiO<sub>2</sub> clusters calcined at different temperatures without silica protection.
- Figure 4.3** Nitrogen adsorption-desorption isotherms of TiO<sub>2</sub> clusters after calcination at 400 °C: (a) a layer of silica was coated on the clusters before calcination, and removed afterwards; (b) clusters were calcined without the silica treatment. The insets show the BJH pore size distribution of the corresponding samples.
- Figure 4.4** (a) Nyquist plots for each photocatalyst nanoparticle in aqueous solution of RhB under UV light illumination. Symbols and lines indicate the experimental data and fitted curves, respectively. (b) Chronoamperometry study of P25 and TiO<sub>2</sub> clusters calcined at different temperatures.

- Figure 4.5** (a) Absorption spectra showing the decomposition of RhB under UV irradiation. (b, c) Photocatalytic conversion of RhB under UV irradiation using TiO<sub>2</sub> clusters and P25 as the photocatalysts. The TiO<sub>2</sub> clusters in (b) were coated with a layer of silica before calcination, while the clusters in (c) were calcined without the silica treatment.
- Figure 4.6** UV–Vis diffusive reflectance absorption spectra of P25, TiO<sub>2</sub> clusters (TC400), and N-doped TiO<sub>2</sub> clusters (calcined at 400 °C, named NTC400).
- Figure 4.7** Photocatalytic conversion of RhB under (a) visible light irradiation ( $\lambda > 400$  nm) and (b) direct sunshine illumination by using no catalyst, P25 aerioxide and N-doped TiO<sub>2</sub> cluster as the photocatalysts.
- Figure 4.8** Seven cycles of photocatalytic degradation of RhB in the presence of NTC400 clusters under direct irradiation of sunshine.
- Figure 4.9** (a) Schematic illustration of the fabrication process of the sandwich-structured SiO<sub>2</sub>/Au/TiO<sub>2</sub> photocatalyst. (b) Typical TEM image of the composite photocatalyst. (c) Elemental mapping of a single particle with the distribution of individual elements shown in the bottom row.
- Figure 4.10** (a) XRD patterns of the SiO<sub>2</sub>/Au/TiO<sub>2</sub> photocatalyst, commercial anatase TiO<sub>2</sub> and P25 aerioxide. The star "\*" denotes rutile phase TiO<sub>2</sub>. (b) UV-visible diffuse reflectance spectra of the three TiO<sub>2</sub>-based photocatalysts and a control sample of AuNP-decorated silica particles.
- Figure 4.11** XPS measurements for the as-obtained SiO<sub>2</sub>/Au/TiO<sub>2</sub> photocatalyst: (a) Ti 2p, and (b) N 1s. All the XPS data have been calibrated with the binding energy of Si-O from SiO<sub>2</sub> at 103.4 eV.
- Figure 4.12** (a) Photodegradation of RhB using anatase, SiO<sub>2</sub>/TiO<sub>2</sub>, P25, SiO<sub>2</sub>/APTES/TiO<sub>2</sub> and SiO<sub>2</sub>/Au/TiO<sub>2</sub> under visible light. (b) Chronoamperometry measurements of P25, SiO<sub>2</sub>/APTES/TiO<sub>2</sub>, and SiO<sub>2</sub>/Au/TiO<sub>2</sub> under periodic illumination of visible light. (c) The influence of AuNPs loading on the catalytic activity of SiO<sub>2</sub>/Au/TiO<sub>2</sub> sandwich structures studied by using the decomposition of RhB as the model system.

**Figure 4.13** (a) Photodegradation of RhB without catalyst and with anatase, P25, and  $\text{SiO}_2/\text{Au}/\text{TiO}_2$  under direct sunlight. (b) Photodegradation of various organic dyes, including RhB, R6G, methylene blue, and 2,4-dichlorophenol with sandwich-structured catalyst under direct sunlight. (c) 7 cycles of the degradation of RhB with  $\text{SiO}_2/\text{Au}/\text{TiO}_2$  photocatalyst under sunlight illumination, demonstrating the stability and recyclability of the catalyst. The duration of sunlight exposure in each cycle is 30 min.

## List of Schemes

- Scheme 1.1** Schematic of plasmon oscillation for a sphere, showing the displacement of the conduction electron charge cloud relative to the nuclei.
- Scheme 1.2** Schematic representation of the resonance plasmon modes involved in the nanodisks. The dipolar in-plane mode and the dipolar out-of-plane mode are represented on (A) and (B), respectively. The corresponding quadrupolar modes are represented on (C) and (D), respectively.
- Scheme 1.3** Schematic illustration of a typical photocatalytic reaction using  $\text{TiO}_2$  as the catalyst: upon irradiation of light, an electron jumps from valence band to conduction band, leaving a hole behind. Since the electron is reductive, it can be used as a reducing agent to produce hydrogen, while the hole is oxidative and can be used as an oxidative agent to remove organic compound and produce carbon dioxide and water.s
- Scheme 2.1** (a) Schematic illustration of the anisotropic seeded growth of Ag nanoplates based on selective ligand adhesion: The citrate ions selectively protect the  $\{111\}$  basal facets of Ag nanoplates and only allow lateral overgrowth; and (b) Schematic illustration of the consequences of seeded growth at different reaction rates: in this work, Ag-citrate complexes ( $\text{Ag}^+\text{-Cit}$ ) are used as the precursors, which can effectively slow down the reaction rate and minimize the self-nucleation events.
- Scheme 3.1** Schematic illustration of the concept of “surface-protected etching” for transforming solid structures into hollow structures with permeable shells. Etching of silica ( $\text{SiO}_2$ ) colloids with NaOH under the protection of PVP is used as an example to describe the process.
- Scheme 3.2** Schematic illustration of the procedures for the fabrication of Au nanoshells containing superparamagnetic  $\text{Fe}_3\text{O}_4$  cores. A unique porous silica layer is produced by a surface-protected etching process, and then utilized to control the seeded growth of Au nanoshells with enhanced reproducibility and structural and optical stability. The TEM images show the  $\text{Fe}_3\text{O}_4@\text{SiO}_2$  cores loaded with Au seeds (left) and then further over-coated with an additional layer of silica (right). Scale bars are 200 nm.

# Chapter 1

## Overview of Engineering and Applications of Nanomaterials

### 1.1 Introduction

Catalysis is of crucial importance to our modern society. Although the earliest observations of catalytic reactions can be dated back to the 19<sup>th</sup> century when chemistry first came into being, it is widely accepted that the first industrialized catalytic process is the synthesis of ammonia in 1913. After nearly a century of development, catalysis has become a complicated science, integrating materials science, chemistry, physics, biology etc. Nowadays, catalysis plays an essential role in industrial applications of direct relevance to many aspects in our daily lives such as petroleum refining, food processing, fine chemical and pharmaceutical production, energy conversion and storage, and automotive emission control.<sup>1-11</sup> It has been pointed out that currently one-third of the material gross national product in the United States involves a catalytic process somewhere in the production chain.<sup>12</sup>

Generally, a catalyst is a special substance that can speed up a specific chemical reaction by lowering its activation energy without itself being consumed in the reaction process. Depending on whether or not it exists in the same phase as the reactants, a catalyst is considered to be either heterogeneous or homogeneous. Heterogeneous

catalysts are mostly solid materials that act on reactants in a liquid or gaseous reaction mixture. As the reaction occurs only when the reactants are adsorbed onto the catalyst surface, the total surface area of the solid has an important effect on the reaction rate. Long before the term "nanotechnology" was introduced, great effort had already been made in the field of catalysis to synthesize catalyst particles with sizes down to the nanometer scale in order to enhance their specific surface area and, consequently, their catalytic activity.

Since the rise of nanotechnology in the 1990s, greater attention has been paid to the structural details of the nanoparticles, including their size, shape and surface properties. The new nanotechnology is helping improve the understanding of reaction mechanisms in industrial catalysis and develop a new-generation of nanostructured catalysts with high catalytic performance.<sup>13-16</sup> Nanostructures of transition metals, for instance, have been recognized as promising catalysts due to their high surface-to-volume ratio, high catalytic selectivity, and relative ease of recycling.<sup>15,17-19</sup> In particular, the rational design and synthesis of nanocrystals with specific shapes leads to the relative enrichment of surface atom ensembles with specific desirable local bonding geometries and has brought about the creation of new catalysts with enhanced activity and selectivity.<sup>20-23</sup> New selective catalysis with these new solution-dispersed or supported metal nanocatalysts has already been demonstrated, and in some cases applied to new types of reactions.<sup>24-37</sup>

In this chapter, I would like to focus on the recent progress in the field of colloidal synthesis of nanomaterials, especially noble metal nanoparticles, and their application in catalysis. We start with a brief introduction to the rise of nanotechnology and the novel physicochemical properties which have arisen from the extremely small size of nanomaterials, as described in **Section 1.2**. Compared to their bulk counterparts, nanomaterials have exhibited some advantages, including large surface area and high surface energy. More importantly, when the size of particle is shrunk to nanometer scale, the materials could show distinctively different properties, such as localized surface plasmon resonances (LSPRs) and novel catalytic properties, which may give rise to many new applications. Then, **Section 1.3** will be focused on the synthesis of nanomaterials through colloidal synthetic techniques. In this section, the colloidal synthesis of two-dimensional silver nanoplates will be used as a model system to demonstrate some fundamentals of colloidal synthetic approaches. Although impressive progress has been achieved in nanotechnology, there are some great challenges facing the research community, which will be discussed in **Section 1.4**. Finally, the scope of this dissertation will be displayed in **Section 1.5**.



## **1.2 The Impact of Nanotechnology on Catalysis**

### **1.2.1 The History of Nanotechnology**

Nanotechnology is a complex and highly interdisciplinary science: it integrates chemistry, physics, materials science, engineering, biology, medicine, etc. Generally, nanotechnology deals with materials at the atomic, molecular or macromolecular level in the length scale of approximately 1-100 nanometers range. A nanometer (nm) is one billionth of a meter, or  $10^{-9}$  m, and a sheet of paper is about 100,000 nanometers thick, according to the U.S. National Nanotechnology Initiative. Although “nanotechnology” is modern terminology, the use of nanotechnology was set into motion a long time ago, mainly based on empirical understanding and manipulation of materials. For example, in the 4<sup>th</sup> century, Romans fabricated the dichroic Lycurgus Cup in which gold and silver nanoparticles were used to allow it to look opaque green when lit from outside but translucent red when light shines through the inside, as shown in Figure 1.1. In about 6<sup>th</sup>-15<sup>th</sup> century, gold chloride nanoparticles have been used to make vibrant stained glass windows with rich colors, which have been used to decorate the cathedrals in European. The first scientific description of nanotechnology is the preparation of “ruby” gold colloids, which was reported by Michael Faraday in 1857.<sup>38</sup> Inspired by the first lecture on technology and engineering at the atomic scale, “There’s Plenty of Room at the Bottom”, presented by Richard Feynman, researchers started to investigate the fabulous

small world. The term “nanotechnology” was then introduced by Norio Taniguchi in 1974 to describe precision machining of materials to within atomic-scale dimensional tolerances.<sup>39</sup> The rise of nanotechnology was greatly inspired by the first discovery of carbon nanotubes in the 1990s and boosted by well developed characterization techniques, especially electron microscopy techniques, including transmission electron microscopy (TEM), scanning electron microscopy (SEM), atomic force microscopy (AFM) etc.<sup>40</sup> Since then, the research in this field has rapidly grown with novel ideas appearing at a swift pace. Over the past two decades, the research in nanotechnology has achieved impressive progress. For instance, nanotechnology has been used to prepare many commercialized products, including nano-silver antibacterial socks and ties, wrinkle- and stain-resistant clothing, clear sunscreens, deep-penetrating therapeutic cosmetics, scratch-resistant glass coatings, self-cleaning paintings, and colorful displays, etc. Nowadays, nanotechnology is attracting more and more attention. It is believed that nanotechnology is a key technology for the future.



**Figure 1.1** Digital images of the Lycurgus Cup at the British Museum, lit from the outside (a) and from the inside (b). Reprinted with permission from British Museum. Copyright © Trustees of the British Museum.

## 1.2.2 Physicochemical Properties of Nanostructured Materials

When the size of particles is reduced dramatically to nanometer range, the surface area to volume ratio would be increased significantly. Table 1.1 describes how the specific surface area and total surface energy of 1g of sodium chloride vary with particle size. The result was calculated based on some assumptions: (1) the original 1g cube was successively divided into smaller cubes; (2) the surface energy is  $2 \times 10^{-5}$  J/cm<sup>2</sup>; and (3) the edge energy is  $3 \times 10^{-13}$  J/cm.<sup>41</sup> For the large cubes, the specific surface area and the surface energy are almost negligible, but become significant when the particle size is reduced to nanometer scale. At the same time, as the size of a particle decreases, the fraction of atoms on particle surfaces also increases dramatically, providing more active sites for catalytic reactions. The ratio of surface atoms to interior atoms changes significantly if one could successively divide a macroscopic object into smaller parts. Figure 1.2 indicates the percentage of surface atoms change with the palladium cluster diameter. When the particle size is  $\sim 63$   $\mu\text{m}$ , the ratio is almost negligible. However, when the particle is reduced to 7 nm in size, about 35% of the atoms will be surface atoms. Further decreasing the size to 1.2 nm, over 76% of the atoms will be exposed. Such a dramatic increase in the surface atoms and surface energy illustrate why changes in the size range of nanometers are expected to lead to great changes in the physical and chemical properties of the materials.

**Table 1.1** Surface area and surface energy as a function of particle size. Adapted with permission from Ref. 41. Copyright © 1976 Elsevier.

Side (cm)	Total Surface Area (cm <sup>2</sup> )	Surface Energy (J/g)
0.77	3.6	$7.2 \cdot 10^{-5}$
0.1	28	$5.6 \cdot 10^{-4}$
0.01	280	$5.6 \cdot 10^{-3}$
0.001	$2.8 \cdot 10^3$	$5.6 \cdot 10^{-2}$
$10^{-4}$ (1 $\mu\text{m}$ )	$2.8 \cdot 10^4$	0.56
$10^{-7}$ (1 nm)	$2.8 \cdot 10^7$	560

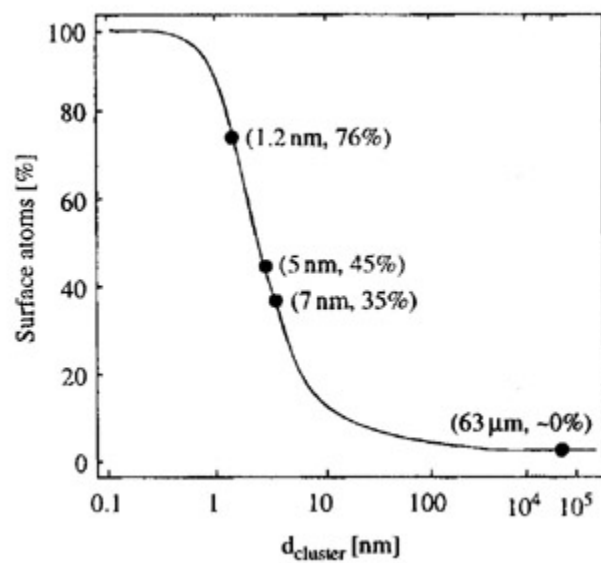


**Figure 1.2** The percentage of surface atoms changes with the palladium cluster diameter. Reproduced with permission from Ref. 42. Copyright © 2000, Società Italiana di Fisica Springer-Verlag.

### 1.2.3 Size-Dependent Catalytic Activities of Nanomaterials

As mentioned above, the development of nanotechnology has significantly changed both research and application of nanomaterials in catalysis. As the particle shrinks to nanoscale range, the surface atoms will experience distinctive changes in atomic arrangement as well as in surface electronic properties. For example, the small particles possess a higher degree of curvature, which could be beneficial for surface-sensitive reactions.<sup>43</sup> Additionally, the advanced nanotechnology allows us to rationally design and prepare nanomaterials with optimized composition and geometry as well as desired physical and chemical properties. With well-defined metal nanocatalysts, many important issues are expected to be understood much deeper, such as the nature of the catalytic active sites, the metal-support interactions, the effect of surface atom arrangement, and the structure-activity and structure-selectivity relationships, which could, in turn, help to prepare nanomaterials with desired morphology as well as desired properties.

It has been widely accepted that the high surface-to-volume ratio of nanomaterials is beneficial for their application in catalysis, which might greatly improve the atom efficiency and reduce the cost of precious metal catalysts. In addition to the enhanced catalytic efficiency, some nanomaterials show completely different activities compared to their bulk counterparts. For example, bulk gold is well known as a chemically inert

material and thus never used as a catalyst. However, Haruta demonstrated in 1997 that gold nanoparticles could be active catalysts in the oxidation of carbon monoxide (CO) when Au nanoparticles are deposited on some oxides substrates, such as  $\text{Fe}_2\text{O}_3$ , NiO and  $\text{MnO}_2$ ,  $\gamma$ -alumina, and titania.<sup>44-47</sup> Further studies revealed that Au nanoparticles are also active catalysts for many other reactions, including partial oxidation of hydrocarbons, hydrogenation of unsaturated hydrocarbons, and reduction of nitrogen oxides.<sup>44,48</sup> Goodman and co-workers have systematically studied the effect of particle size using CO oxidation as the model system.<sup>45</sup> As shown in Figure 1.4, Au particles with sizes over 3.5 nm are almost inactive in catalytic action. However, when the size of gold particle is reduced to ~3 nm, it shows excellent catalytic activity even at low temperature. Additionally, a further decrease in particle diameter below 3 nm will lead to a decrease in the activity of the Au. It is believed that the excellent catalytic property of gold nanoparticles is a combination of size effect and the unusual properties of individual gold atoms.



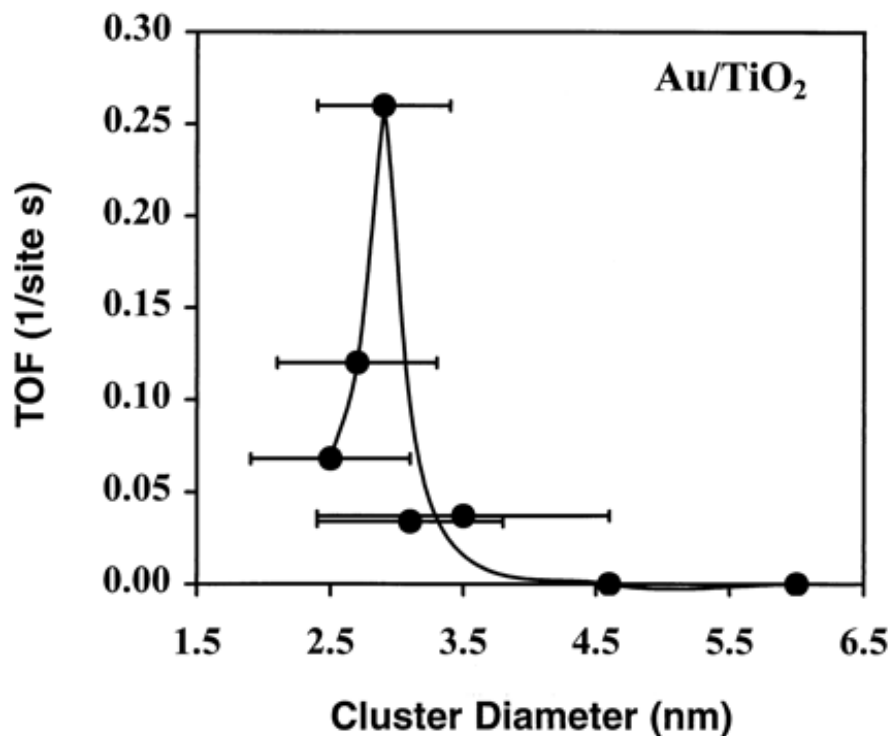


**Figure 1.3** CO oxidation turnover frequencies (TOFs) at 300 K as a function of the average size of the Au clusters supported on a high surface area TiO<sub>2</sub> support. The Au/TiO<sub>2</sub> catalysts were prepared by deposition-precipitation method, and the average cluster diameters were measured by TEM. The solid line serves merely to guide the eye. Reprinted with permission from Ref. 45. Copyright © 1998 The American Association for the Advancement of Science.

### 1.2.4 Shape-Dependent Catalytic Properties

It has long been believed that the structure of the surface of solid catalysts affects their performance.<sup>49,50</sup> However, until recently, the evidence for this has been indirect.<sup>51,52</sup> It has been repeatedly shown that, with catalysts where the active phase is dispersed as fine particles on high-surface-area supports, changes in the load of that active phase lead to variations in specific activity and/or selectivity. In many instances, electron microscopy has been used to show that higher loads also lead to particles with broader size distributions and increased average diameters. It has been assumed that larger particles are likely to display a larger fraction of flat, thermodynamically stable, terraces, whereas smaller particles are expected to have more low-coordination atoms and more defects. Hence, the inference has been that if the performance of supported catalysts changes with the loading of the active phase, it must be because the reactions are sensitive to the structure of the surfaces involved. More recent studies using single-crystal surfaces<sup>53,54</sup> and other model systems<sup>55,56</sup> have conclusively corroborated that, indeed, the structure of the surface can exert great influence on the performance of catalysts. This is particularly true for so-called demanding reactions such as ammonia synthesis and the water-gas shift reactions, which operate at high pressure and temperature,<sup>57,58</sup> but this has also been recently proven for milder hydrocarbon conversions,<sup>59,60</sup> even for reactions previously considered structure insensitive.<sup>61</sup>

The advances in nanotechnology enabled the synthesis of well-defined nanocrystals with desired structure as well as desired exposed facets, which further propelled the research in the shape-dependent catalytic activities. For example, Zaera and co-workers have prepared platinum nanoparticles with different shapes: spherical, tetrahedral, and cubic, which could preferentially expose (111) or (100) facets (size and shape could be controlled independently with the colloidal approach). Based on the previous surface-science work with model single-crystal surfaces and quantum mechanical calculations, it has been pointed out that while (111) facets of platinum favor the formation of cis-olefins, more open surface structures promote the formation of the trans isomers instead.<sup>61-70</sup> That difference was explained by the combined effect of co-adsorbed hydrogen and an adsorption-induced reconstruction, which appears to be more severe with the trans-isomer and with close-packed surfaces. It was shown that the selectivity of the olefin isomerization reactions could indeed be controlled by using supported catalysts with appropriate metal nanoparticle shapes. Furthermore, as presented in Figure 1.5, they demonstrated that dispersed tetrahedral Pt nanoparticles with exposed (111) facets were shown to preferentially promote the conversion of trans-2-butene to cis-2-butene,<sup>61</sup> whereas either cubic<sup>69</sup> or spherical<sup>61</sup> nanoparticles were identified as better promoters for the formation of the trans-isomer.

## 2-Butene Isomerization on Pt/SiO<sub>2</sub>

Initial Rate versus Particle Shape

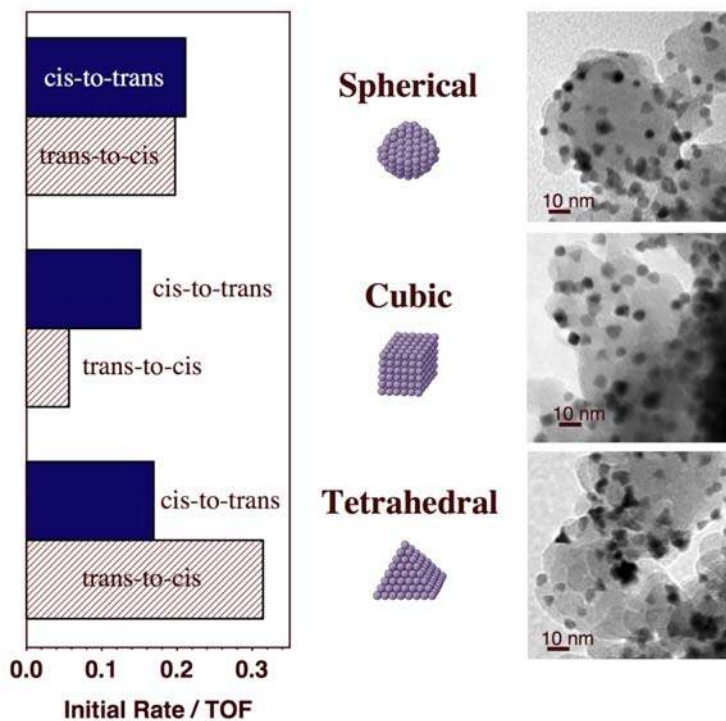


**Figure 1.4** Image showing the shape-dependent catalytic selectivity using the catalytic isomerization of 2-butenes in the presence of Pt nanocatalysts as the model system. Reprinted with permission of the PCCP Owner Societies from Ref. 71. Copyright © 2010 Royal Society of Chemistry.

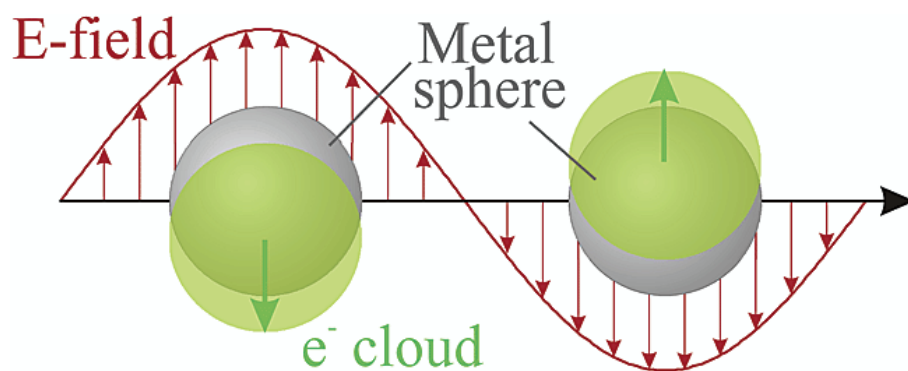
### 1.2.5 Plasmonic Nanomaterials

When the particle size is shrunk to nanometer range, the product can show distinctively different properties from their bulk counterparts. For example, the color of bulk gold is gold, while the color of bulk silver is silver. However, when the size of gold or silver is reduced to nanometer size, they can show different amazing colors: gold can be red, while silver can be yellow. As we mentioned above, the Lycurgus Cup can show different colors, which could be attributed to the usage of gold and silver nanoparticles. With the development of nanotechnology, people now can prepare gold or silver nanoparticles with different colors by simply tuning their size, shape or composition. Figure 1.3 shows a digital image of colloidal silver nanoplates, from which one can clearly see different shining colors, ranging among yellow, red, purple, green and blue.

The elegant colors of such colloids arise from surface plasmon resonances, which are oscillation modes arising from the coupling between an electromagnetic field (in the visible range for Au, Ag) and the collective oscillations of conduction electrons. In more detail, when a small spherical metal nanoparticle is irradiated by light, the conduction electron oscillates coherently due to the oscillating electric field, as illustrated in Scheme 1.1. When the electron cloud is displaced relative to the nuclei, a restoring force arises from Coulomb attraction between electrons and nuclei that results in oscillation of the electron cloud relative to the nuclear framework.



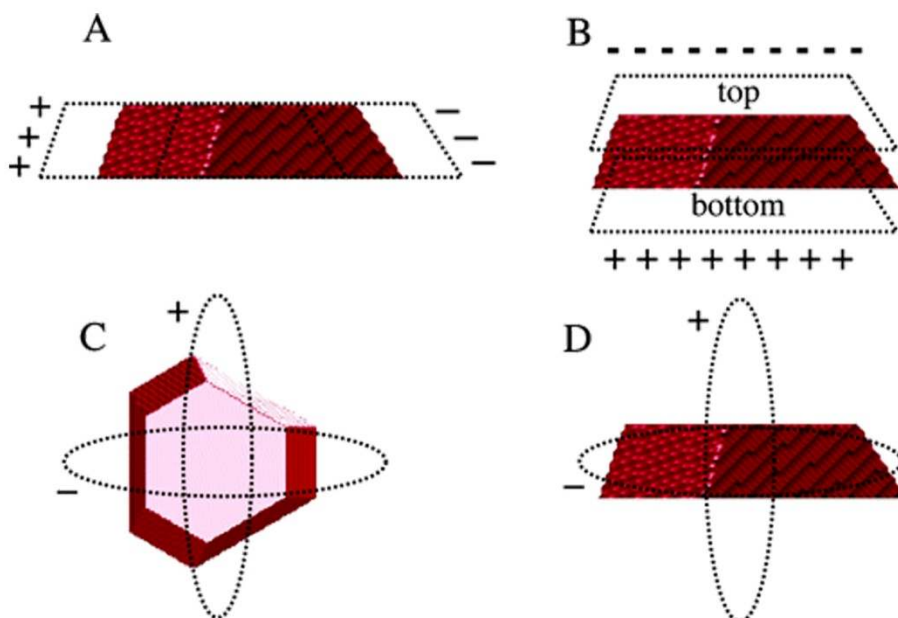
**Figure 1.5** Digital image of colloidal silver nanoplates with different colors. Adapted with permission from Ref. 72. Copyright © 2012 WILEY-VCH Verlag GmbH & Co. KGaA, Weinheim



**Scheme 1.1** Schematic of plasmon oscillation for a sphere, showing the displacement of the conduction electron charge cloud relative to the nuclei. Reprinted with permission from Ref. 73. Copyright © 2003 American Chemical Society.

Although such plasmon resonances do occur in bulk metals and in metal films, they are much weaker than the other effects, such as scattering, and thus cannot be presented. Only when the particles are significantly smaller than the incident wavelength, e.g., in nanometer size, the contribution from scattering is significantly eliminated, and the resonance condition is only fulfilled within a narrow spectral range, which is reflected in well-defined bands in UV-vis spectra. In this condition, SPR is called localized surface plasmon resonances (LSPRs). There are several different modes of LSPR. When the particles are very small, there is only the collective oscillation of the electrons, which is called the dipole plasmon resonance. Higher modes of plasmon excitation can occur when the particle size becomes bigger, such as the quadrupole mode where half of the electron cloud moves parallel to the applied field and half moves antiparallel. In addition to the size effect, nonspherical particles can present various different LSPR modes as a result of the different possible oscillations that can arise from different orientations with respect to the electric field of the incident electromagnetic radiation. In the case of triangular nanoplates, Schatz et al have demonstrated theoretically that both in-plane and out-of-plane excitations can lead to dipolar and quadrupolar resonances, as depicted in Scheme 1.2. It has been reported that the LSPR frequency is sensitive toward changes in various parameters including particle composition, size and shape, interparticle spacing and dielectric properties of the surrounding medium.





**Scheme 1.2** Schematic representation of the resonance plasmon modes involved in the nanodisks. The dipolar in-plane mode and the dipolar out-of-plane mode are represented on (A) and (B), respectively. The corresponding quadrupolar modes are represented on (C) and (D), respectively. Reprinted with permission from Ref. 74. Copyright © 2005 American Chemical Society.

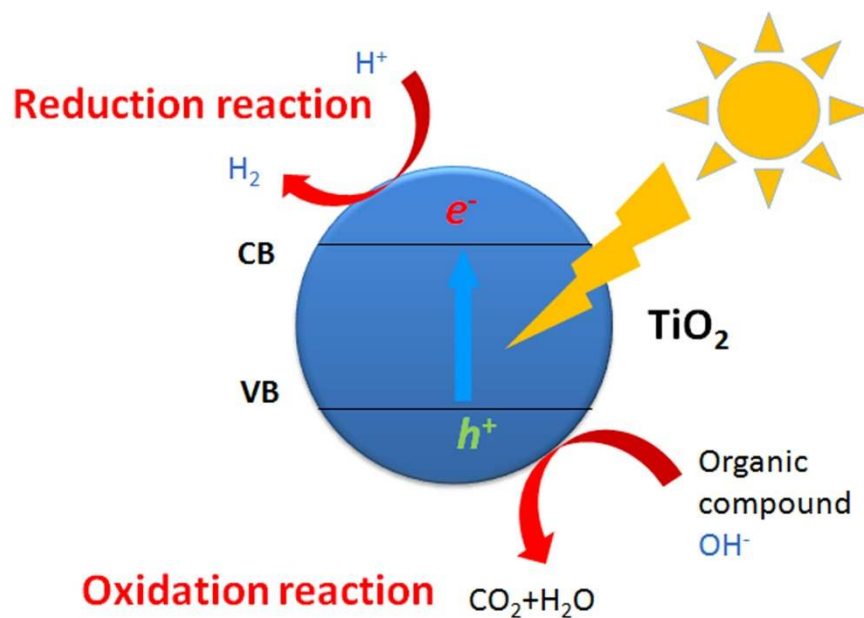
There are some unique features of the LSPR, such as narrow and sensitive bands, and strong field enhancement, making it an interesting property for many applications. For example, it was believed that metals could not be used as efficient photocatalysts due to their low efficiencies of energetic charge-carrier formation and short lifetime, although they have high inherent chemical activity and ability to selectively activate numerous chemical transformations. However, it was recently realized that some noble metals, such as gold and silver, could be used as efficient photocatalysts owing to their surface plasmon resonances. For instance, Linic and co-workers have demonstrated that Ag nanoparticles could be directly used as an efficient catalyst for oxidation reactions, such as ethylene epoxidation, CO oxidation, and NH<sub>3</sub> oxidation, by utilizing their plasmonic property.<sup>75</sup> Although direct photocatalysis utilizing such plasmonic nanostructures is still limited so far, it has drawn much more attention due to its potential applications in many fields. Another important approach to utilize their SPR property in catalysis is to make plasmonic metal/semiconductor composites to enhance the activity of photocatalysts in visible light,<sup>76-78</sup> as plasmonic metals can absorb visible light and inject electrons to semiconductors, e.g., anatase TiO<sub>2</sub>.

### 1.2.6 TiO<sub>2</sub>-Based Photocatalysts

Clean and sustainable solar energy has been extensively explored in order to overcome the increasingly serious energy and environmental challenges. Among numerous approaches, chemical utilization of solar energy through photo-catalysis has been recognized as one of the most promising methods.<sup>79-83</sup> Since the discovery of water splitting on the surface of titanium dioxide (TiO<sub>2</sub>) electrode under UV light irradiation,<sup>84</sup> TiO<sub>2</sub> has been the most widely used photocatalyst in practical applications, including water splitting, water purification, carbon dioxide conversion, etc, due to its favorable features such as low cost, good chemical and mechanical stability, high photocatalytic activity, and non-toxic nature.<sup>2,85-93</sup> There are three polymorphs of crystalline TiO<sub>2</sub>, including rutile, anatase, and brookite in nature, among which anatase and rutile are usually employed as photocatalysts, while the photocatalytic activity of brookite has been little investigated. In photocatalysis research, anatase TiO<sub>2</sub> is considered to be more active than rutile crystalline form because of its lower charge recombination rate and higher surface adsorptive affinity for organic compounds.<sup>94-96</sup> Anatase TiO<sub>2</sub> is thermodynamically metastable and transforms to rutile phase at high temperature (~ 600 °C). The harvest of solar energy through TiO<sub>2</sub> photocatalyst can be roughly described in three sequential steps: (1) generation of electron-hole (e<sup>-</sup>-h<sup>+</sup>) pairs upon the absorption of photons; (2) charge separation and migration to the catalyst surface; and (3) surface redox

reactions, as depicted in Scheme 1.3. Much effort has been devoted to developing highly active TiO<sub>2</sub>-based photocatalysts, all of which was trying to improve the performance in one or all of these three steps.<sup>97-101</sup> For example, the main drawback of pristine anatase TiO<sub>2</sub> photocatalyst is the large band gap energy (~ 3.2 eV) which allows it to absorb only UV light. As a result, many researchers have focused on developing visible light active TiO<sub>2</sub> photocatalysts that can make use of both UV (290-400 nm) and visible (400-700 nm) radiation to enhance process efficiencies. Dye-sensitization has been employed to extend the absorption from UV range to visible range. Organic dyes are usually transition metal complexes with low lying excited states, including polypyridine complexes, phthalocyanine, and metalloporphyrins.<sup>102-105</sup> However, the promise of such dye-sensitized TiO<sub>2</sub> materials and devices for practical applications are still under debate because of the instability of organic dyes upon light irradiation.<sup>106</sup> Metal-ion doping is another popular method to make visible-light-active TiO<sub>2</sub>-based photocatalysts, which, however, in many cases suffer from serious deterioration in their photocatalytic performance because metal ions themselves can act as the recombination centers of e<sup>-</sup> and h<sup>+</sup>.<sup>107-109</sup> It has been demonstrated recently that non-metal doping, including N, C, P and S, could be useful in preparing visible-light-active TiO<sub>2</sub>-based photocatalysts, even though the understanding on the origin of the enhanced activity is still controversial.<sup>106,110-113</sup> Additionally, so far new materials have typically suffered

from low doping concentration and/or low stability against photo-corrosion.<sup>114-117</sup> On the other hand, the improved absorption of photon may not necessarily guarantee better photocatalytic performance because the efficiency of a photocatalyst is also determined by the charge separation and transportation step during the photo-excitation process. Due to the fast recombination of  $e^-h^+$  pairs, most excited charges have recombined and quenched before they can reach the surface. From this point of view, small crystal size and high crystallinity would be desirable for enhancing charge separation efficiency; that would result in a reduced migration distance of charges and, consequently, in a lower recombination rate.<sup>118,119</sup> Another favorable consequence of the small crystal size is the large surface area which may improve the performance in the last step because it can provide more reactive sites. High crystallinity can reduce the defects which normally act as recombination centers. Additionally, metal decoration has also been shown to enhance charge separation in  $TiO_2$  photocatalysts by serving as electron reservoirs.<sup>120</sup>



**Scheme 1.3** Schematic illustration of a typical photocatalytic reaction using  $\text{TiO}_2$  as the catalyst: upon irradiation of light, an electron jumps from valence band to conduction band, leaving a hole behind. Since electron is reductive, it can be used as a reducing agent to produce hydrogen, while hole is oxidative and can be used as an oxidative agent to remove organic compound and produce carbon dioxide and water.

### 1.3 Colloidal Synthesis of Silver Nanoplates

Generally, there are two main approaches to the synthesis of nanomaterials: top-down and bottom-up approaches. A top-down approach is essentially the breaking down of a macroscopic object to get nanoparticles. Attrition or milling is a typical top-down method in making nanomaterials. Although the top-down method can produce nanomaterials in large quantity, it has some disadvantages. For instance, the top-down method cannot precisely control the final product, which are usually featured by a broad size distribution and low uniformity in shape. Additionally, the top-down method usually introduce lots of imperfection or defects into the final product. It is well known that the conventional top-down techniques such as lithography can cause significant crystallographic damage to the processed patterns,<sup>121</sup> and additional defects may be introduced during the etching steps.<sup>122</sup> The bottom-up approach is to build up small components (atoms, molecules, or clusters) into more complex objects. Compared to the traditional top-down approaches, the bottom-up approach has many advantages, such as fewer defects, more homogeneous chemical composition, more precise control over the morphology, more uniform product, and more complex architectures as well as multi-functional materials. Nowadays colloidal synthesis routes, as a typical bottom-up approach, have attracted much more attention due to rich features such as low cost, simple set-up, and large mass-production. In this section, I would like to use the

colloidal synthesis of silver nanoplates as the model system to introduce the colloidal synthetic technique.

Silver nanoplates, also referred to as nanoprisms or nanodisks, are two dimensional plasmonic nanostructures that have attracted considerable attention due to their strong shape-dependent optical properties and related applications.<sup>123-127</sup> When the lateral dimension of silver nanoplates is much larger than the thickness, they possess an extreme degree of anisotropy, which favors a high tunability of their localized surface plasmon resonance (LSPR) and therefore generates maximum electromagnetic-field enhancement.<sup>128</sup> After the seminal report by Mirkin et al. on the photo-induced synthesis of silver nanoplates in 2001,<sup>129</sup> a variety of solution based strategies have been developed by many other groups to synthesize silver nanoplates, including photochemical processes,<sup>130-135</sup> ligand-assisted chemical reductions,<sup>136-138</sup> electrochemical synthesis,<sup>139</sup> templating procedures,<sup>140</sup> and sonochemical routes.<sup>141</sup> Among all these methods, direct chemical reduction has been the most popular due to the considerably high yield and relatively simple setups and procedures which show promise for large scale production.<sup>142-146</sup> Although many mechanisms have been proposed to explain the developed synthetic strategies, most of them are empirical and lack a thorough scientific understanding.



The formation of extremely anisotropic silver nanoplates is not thermodynamically favored because it involves a competition against the desire to minimize the surface area and energy through the formation of Wulff polyhedrons (a truncated octahedron) enclosed by a mix of {111} and {100} facets.<sup>147-149</sup> Much effort has been made to understand the mechanism, and many hypotheses have been proposed to explain the formation of such highly anisotropic structures. The most popular theory at the early stages of research was the “face-blocking theory”, in which a capping agent selectively adheres to a particular crystal facet of the growing nanocrystal and thus slows the growth rate of that facet relative to the others.<sup>123,124</sup> However, it has been gradually realized that preferential anisotropic growth is dependent not only upon the selective adhesion of capping ligands but also on the crystal symmetry of the starting nuclei.<sup>142,150</sup> For materials with isotropic crystal structures, anisotropic growth cannot be guaranteed by simply introducing selective binding ligands into the reaction. Instead, it is usually facilitated by breaking the isotropic symmetry with the formation of twin or other defect planes during the nucleation stage, which is, however, still a great challenge to control during synthesis. Based on crystallographic arguments, it is believed that the final morphology of the nanostructure is determined by the internal crystal structure of the original seed particle because of the limited number and variety of crystal facets available for growth.<sup>151-153</sup> Pileni et al. have attributed the  $1/3\{422\}$  reflections observed in silver

and gold nanoplates, which should be forbidden for a perfect fcc structure, to parallel stacking faults in the  $\langle 111 \rangle$  direction,<sup>154</sup> and further pointed out that these stacking faults should be responsible for the formation of plate structures by providing low-energy reentrant grooves which energetically favor lateral crystal growth. The fact that plate structures are more often observed in silver and gold than other metals is due to their lowest stacking fault energies.<sup>148</sup> Based on high-resolution transmission electron microscopy (HRTEM) and X-ray diffraction (XRD) studies, Rocha and Zanchet found that the internal structure of silver nanoplates is indeed very complex containing many twins and stacking faults.<sup>155</sup> In their studies, planar defects in the  $\langle 111 \rangle$  direction have been found to give rise to local hcp regions, which can also be used to explain the existence of forbidden 2.50 Å fringes that are observed in  $\langle 111 \rangle$  orientated nanoplates. Kelly et al. further elucidated the formation mechanism of the hcp layer which was used to explain the evolution of silver nanoplates.<sup>156</sup> Xia et al. have recently pointed out the importance of interweaving both crystallographic and surface chemistry arguments in order to discern the overall mechanism of nanoplate formation.<sup>126,157</sup>

Despite the continuously improving understanding of the cause of plate formation by defects, the chemical origin of these defects has remained largely unknown. This is mainly due to the lack of systematic studies to clarify the role of each reagent in determining the structure of seeds and their growth process, which often leads to

contradictory conclusions that make it difficult to ascertain the true cause of defect formation. For example, while many prior works have deemed some chemicals such as citrate and/or polyvinylpyrrolidone (PVP) to be critically important components in a given reaction, a number of researchers have attributed their success in nanoplate synthesis to the presence of other chemical species or reaction conditions.<sup>155</sup> In addition, other researchers have demonstrated the production of silver nanostructures with different morphologies by starting with the same seeds but under slightly altered synthetic conditions, such as seed concentration, surfactants, pH value, and reaction temperature.<sup>124</sup> The lack of deep understanding of the specific contributions of the reaction components also makes it difficult to reproduce many of the reported results with satisfactory yield and quality because some minor unintentional alterations to the reaction conditions may easily disturb nanoplate formation.

## 1.4 Challenges in Utilizing Nanomaterials

One of the major challenges in the use of nanostructured materials as catalysts is their chemical and structural stability. For example, without sufficient surface passivation, nanoparticles with high surface energy may rapidly grow larger, thus reducing the active surface area for catalysis. This process, often referred to in catalysis as sintering, occurs with catalysts both dispersed in solution and immobilized on solid supports.<sup>158</sup> It is generally accepted that two mechanisms are responsible for the catalyst growth: Ostwald ripening and particle coalescence, both of which are driven by the reduction of total surface energy. Ostwald ripening involves the leaching of atoms from small particles and their subsequent transport and re-deposition onto larger particles, while coalescence involves the migration and merging of entire particles. In principle, the particle growth mechanism operative in specific cases can be deduced from the changes of the skewness of the particle size distribution with time.<sup>159</sup> In reality, however, unambiguous correspondence with theory remains difficult to achieve, as in many cases both mechanisms operate simultaneously, making data interpretation quite complicated.<sup>160</sup>

These types of particle instabilities may also induce shape changes in the nanocatalysts during reactions. In principle, the shape of nanostructures may be chosen deliberately to enhance the exposure of certain high-energy facets, corners, and edges, which may be particularly active in catalyzing reactions. However, in practice, nanocatalysts may

rapidly evolve toward lower-energy shapes, an evolution that may lead to a significant reduction in activity even during the initial stages of reactions.<sup>35,161</sup> This problem is particularly true for so-called demanding reactions, which require high pressures and/or temperatures.<sup>16,162</sup> It is therefore important to study the mechanisms of shape change and explore methods for improving the shape stability of metal nanoparticles. To date, there are only a few studies reported in the literature addressing the shape changes of the nanocrystals following catalytic reactions, in part perhaps because such shape changes are usually accompanied by sintering of the particles. Prevention of catalyst nanoparticles from sintering is critical to the production of stable catalysts, and is the first requirement to be able to fully take advantage of the many merits of the new synthetic methodology available for the making of nanostructured catalysts.

Besides the possible loss of active surface area due to coagulation, nanoparticles may also undergo shape changes during catalytic processes.<sup>35,163</sup> Because molecules actively interact with the surface of the catalyst during catalytic reactions, the surface protection afforded by the original surfactants is usually weakened, after which the shape changes may occur rather quickly. Such changes lead to significant alternations of the activity and selectivity of metallic catalysts.<sup>164</sup> These issues have limited the lifetime of nanoparticle-based catalysts, preventing their direct reuse and leading to the need to implement costlier measures associated with the disposal and recycling of spent catalysts.

## **1.5 Scope of This Dissertation**

The design and fabrication of highly active catalysts in an efficient and cost-effective way is an important topic due to their practical applications in various fields. This dissertation discusses our efforts in the engineering of nanomaterials and their application in catalysis. It can be divided into three consecutive stages: (1) controllable synthesis of nanomaterials with desired morphology and physiochemical properties; (2) stabilization of nanomaterials by embedding nanoparticles into a mesoporous oxide shell; and (3) design and fabrication of nanomaterials for practical applications based on the improved understanding and advanced synthetic techniques obtained from stage (1) and (2).

Chapter 2 represents a systematic study on the colloidal synthesis of silver nanoplates. First, to get deeper understanding of the colloidal synthetic strategies, we have identified the specific roles of each reagent in the direct chemical reduction route to silver nanoplates. This work outlines the key components that determine the formation of Ag nanoplates, clarifies the roles of each reagent, provides highly reproducible recipes for synthesis, and therefore represents a significant step towards the complete understanding of the mechanism behind the experimental phenomena. Additionally, Ag nanoplates with extremely high aspect ratios (up to over 400) and widely tunable SPR bands have been successfully obtained through a two-step seeded growth process. We believe the concept can be well applied to many other materials. Finally, we have demonstrated

that the optical properties of Ag nanoplates can be precisely tuned over a wide range through a UV light induced reconstruction process, in which the morphology of the nanoparticles is changed from thin triangular plates to thick round plates. Stabilized with PVP, the as-obtained Ag nanoplates remain stable for long time without any noticeable changes in their optical properties.

Due to their large surface area and high surface energy, one of the major challenges in the use of nanostructured materials as catalysts is their chemical and structural stability. Chapter 3 will be focused on the stabilization of metallic nanocatalysts using porous oxide shells for catalytic applications in both the liquid and gas phases. First, a general strategy, called the “surface-protected etching” process, will be introduced as the major synthetic tool for producing mesoporous shells for the stabilization of noble metal nanocatalysts. Its feasibility and flexibility in controlling the pore size and architecture of the oxide shell will be illustrated. Then, a sandwich-like structure has been prepared based on the “surface-protected etching” process. Multi-functional materials could be incorporated to make recyclable and highly efficient catalysts. The as-prepared sandwich structure could be further used in gas phase reaction, which shows improved stability against high temperature sintering.

Based on the improved understanding on the shape-dependent properties and the advanced synthetic techniques in colloidal nanomaterials, we now are able to design and fabricate novel catalysts for practical applications. Chapter 4 will display the engineering of TiO<sub>2</sub>-based nanomaterials for photocatalytic applications. First, we report a general strategy for the fabrication of mesoporous TiO<sub>2</sub> photocatalysts based on the self-assembly of TiO<sub>2</sub> nanocrystals. By optimizing the synthesis condition, i.e., calcination temperature, TiO<sub>2</sub> clusters with good photocatalytic activity have been obtained. Then, we present the design and synthesis of a highly efficient, stable, and cost-effective TiO<sub>2</sub>-based photocatalyst with the desired properties by combining simple sol-gel and calcination processes. The new catalyst has a sandwich structure that comprises a SiO<sub>2</sub> core, a layer of gold nanoparticles (AuNPs), and a doped-TiO<sub>2</sub> nanocrystalline shell. The new photocatalysts shows excellent performance in degradation reactions of a number of organic compounds under UV, visible light, and direct sunlight.



## 1.6 References

- (1) Lewis, L. N. *Chem. Rev.* **1993**, *93*, 2693.
- (2) Hoffmann, M. R.; Martin, S. T.; Choi, W. Y.; Bahnemann, D. W. *Chem. Rev.* **1995**, *95*, 69.
- (3) Britovsek, G. J. P.; Gibson, V. C.; Wass, D. F. *Angew. Chem. Int. Ed.* **1999**, *38*, 428.
- (4) Derouane, E. G. *Cattech* **2001**, *5*, 214.
- (5) Noyori, R. *Angew. Chem. Int. Ed.* **2002**, *41*, 2008.
- (6) Lindstrom, B.; Pettersson, L. J. *Cattech* **2003**, *7*, 130.
- (7) Benkovic, S. J.; Hammes-Schiffer, S. *Science* **2003**, *301*, 1196.
- (8) Astruc, D.; Lu, F.; Aranzaes, J. R. *Angew. Chem. Int. Ed.* **2005**, *44*, 7852.
- (9) Poliakoff, M.; Licence, P. *Nature* **2007**, *450*, 810.
- (10) Schmidt, L. D.; Dauenhauer, P. J. *Nature* **2007**, *447*, 914.
- (11) Wittstock, A.; Zielasek, V.; Biener, J.; Friend, C. M.; Baumer, M. *Science* **2010**, *327*, 319.
- (12) *Chem. Ind.* **2002**, *21*, 22.
- (13) Pernicone, N. *Cattech* **2003**, *7*, 196.
- (14) Rolison, D. R. *Science* **2003**, *299*, 1698.
- (15) Somorjai, G. A.; Tao, F.; Park, J. Y. *Top. Catal.* **2008**, *47*, 1.
- (16) Albiter, M.; Crooks, R.; Zaera, F. *J. Phys. Chem. Lett.* **2010**, *1*, 38.
- (17) Bell, A. T. *Science* **2003**, *299*, 1688.
- (18) Grunes, J.; Zhu, J.; Somorjai, G. A. *Chem. Commun.* **2003**, 2257
- (19) Xiong, Y.; Wiley, B. J.; Xia, Y. *Angew. Chem. Int. Ed.* **2007**, *46*, 7157.
- (20) Lee, I.; Zaera, F. *J. Am. Chem. Soc.* **2005**, *127*, 12174.
- (21) Bratlie, K. M.; Lee, H.; Komvopoulos, K.; Yang, P.; Somorjai, G. A. *Nano Lett.* **2007**, *7*, 3097.
- (22) Lee, I.; Morales, R.; Albiter, M. A.; Zaera, F. *Proc. Nat. Acad. Sci. USA* **2008**, *105*, 15241.

- (23) Lee, I.; Delbecq, F.; Morales, R.; Albiter, M. A.; Zaera, F. *Nature Mater.* **2009**, *8*, 132.
- (24) Freund, P. L.; Spiro, M. *J. Phys. Chem.* **1985**, *89*, 1074.
- (25) Somorjai, G. A. *Appl. Surf. Sci.* **1997**, *121/122*, 1.
- (26) Shiraishi, Y.; Toshima, N. *J. Mol. Catal. A* **1999**, *141*, 187.
- (27) Spiro, M.; de Jesus, D. M. *Langmuir* **2000**, *16*, 2464.
- (28) Li, Y.; Petroski, J.; El-Sayed, M. A. *J. Phys. Chem. B* **2000**, *104*, 10956.
- (29) Yeung, L. K.; Crooks, R. M. *Nano Lett.* **2001**, *1*, 14.
- (30) Anderson, M. L.; Stroud, R. M.; Rolison, D. R. *Nano Lett.* **2002**, *2*, 235.
- (31) Gopidas, K. R.; Whitesell, J. K.; Fox, M. A. *Nano Lett.* **2003**, *3*, 1757.
- (32) Yoo, J. W.; Hathcock, D. J.; El-Sayed, M. A. *J. Catal.* **2003**, *214*, 1.
- (33) Narayanan, R.; El-Sayed, M. A. *J. Am. Chem. Soc.* **2003**, *125*, 8340.
- (34) Na, Y.; Park, S.; Han, S. B.; Han, H.; Ko, S.; Chang, S. *J. Am. Chem. Soc.* **2004**, *126*, 250.
- (35) Narayanan, R.; El-Sayed, M. A. *J. Am. Chem. Soc.* **2004**, *126*, 7194.
- (36) Adlim, M.; Abu Bakar, M.; Liew, K. Y.; Ismail, J. *J. Mol. Catal. A* **2004**, *212*, 141.
- (37) Chen, Z.; Waje, M.; Li, W.; Yan, Y. *Angew. Chem. Int. Ed.* **2007**, *46*, 4060.
- (38) Faraday, M. *Philos. Trans. Royal Soc. London* **1857**, *147*, 145.
- (39) Taniguchi, N. In *Proc. Intl. Conf. Prod. Eng.* Tokyo, 1974.
- (40) Iijima, S. *Nature* **1991**, *354*, 56.
- (41) Ivanov, V. P.; Boreskov, G. K.; Savchenko, V. I. *Surf. Sci.* **1976**, *61*, 207.
- (42) Nutzenadel, C.; Zuttell, A.; Chartouni, D.; Schmid, G.; Schlapbach, L. *Eur Phys J D* **2000**, *8*, 245.
- (43) Jin, R. *Nanotechnol. Rev.* **2012**, *1*, 31.
- (44) Haruta, M. *Catal. Today* **1997**, *36*, 153.
- (45) Valden, M.; Lai, X.; Goodman, D. W. *Science (Washington, D. C.)* **1998**, *281*, 1647.
- (46) Bondzie, V. A.; Parker, S. C.; Campbell, C. T. *J Vac Sci Technol A* **1999**, *17*, 1717.

- (47) Grisel, R. J. H.; Nieuwenhuys, B. E. *J Catal* **2001**, *199*, 48.
- (48) Zhang, Q.; Zhang, T.; Ge, J.; Yin, Y. *Nano Lett.* **2008**, *8*, 2867.
- (49) Thomas, J. M.; Thomas, W. J. *Introduction to the Principles of Heterogeneous Catalysis*; Academic Press: London, 1967.
- (50) Boudart, M. *Adv. Catal.* **1969**, *20*, 153.
- (51) Anderson, J. R. *Sci. Prog. (St. Albans, U. K.)* **1985**, *69*, 461.
- (52) Bond, G. C. *Acc. Chem. Res.* **1993**, *26*, 490.
- (53) Somorjai, G. A.; Zaera, F. *J. Phys. Chem.* **1982**, *86*, 3070.
- (54) Rodriguez, J. A.; Goodman, D. W. *Surf. Sci. Rep.* **1991**, *14*, 1.
- (55) Gates, B. C. *Top. Catal.* **2001**, *14*, 173.
- (56) Freund, H. J.; Libuda, J.; Baumer, M.; Risse, T.; Carlsson, A. *Chem. Rec.* **2003**, *3*, 181.
- (57) Zaera, F.; Gellman, A. J.; Somorjai, G. A. *Acc. Chem. Res.* **1986**, *19*, 24.
- (58) Ertl, G. *Angew. Chem., Int. Ed.* **2008**, *47*, 3524.
- (59) Davis, S. M.; Zaera, F.; Somorjai, G. A. *J. Am. Chem. Soc.* **1982**, *104*, 7453.
- (60) Davis, S. M.; Zaera, F.; Somorjai, G. A. *J. Catal.* **1984**, *85*, 206.
- (61) Lee, I.; Delbecq, F.; Morales, R.; Albitzer, M. A.; Zaera, F. *Nat. Mater.* **2009**, *8*, 132.
- (62) Lee, I.; Zaera, F. *J. Phys. Chem. B* **2005**, *109*, 2745.
- (63) Lee, I.; Zaera, F. *J. Am. Chem. Soc.* **2005**, *127*, 12174.
- (64) Lee, I.; Zaera, F. *J. Phys. Chem. C* **2007**, *111*, 10062.
- (65) Delbecq, F.; Zaera, F. *J. Am. Chem. Soc.* **2008**, *130*, 14924.
- (66) Lee, I.; Nguyen, M. K.; Morton, T. H.; Zaera, F. *J. Phys. Chem. C* **2008**, *112*, 14117.
- (67) Brandt, B.; Fischer, J.-H.; Ludwig, W.; Schauermaun, S.; Libuda, J.; Zaera, F.; Freund, H.-J. *J. Phys. Chem. C* **2008**, *112*, 11408.
- (68) Brandt, B.; Ludwig, W.; Fischer, J. H.; Libuda, J.; Zaera, F.; Schauermaun, S. *J. Catal.* **2009**, *265*, 191.
- (69) Lee, I.; Zaera, F. *J. Catal.* **2010**, *269*, 359.

- (70) Lee, I.; Hong, J.; Zaera, F. *J. Phys. Chem. C* **2010**, submitted.
- (71) Lee, I.; Albiter, M. A.; Zhang, Q.; Ge, J. P.; Yin, Y. D.; Zaera, F. *Phys Chem Chem Phys* **2011**, *13*, 2449.
- (72) Li, N.; Zhang, Q.; Quinlivan, S.; Goebel, J.; Gan, Y.; Yin, Y. *ChemPhysChem* **2012**, n/a.
- (73) Kelly, K. L.; Coronado, E.; Zhao, L. L.; Schatz, G. C. *J. Phys. Chem. B* **2003**, *107*, 668.
- (74) Brioude, A.; Pileni, M. P. *J Phys Chem B* **2005**, *109*, 23371.
- (75) Christopher, P.; Xin, H. L.; Linic, S. *Nat Chem* **2011**, *3*, 467.
- (76) Furube, A.; Du, L.; Hara, K.; Katoh, R.; Tachiya, M. *J. Am. Chem. Soc.* **2007**, *129*, 14852.
- (77) Naya, S.; Inoue, A.; Tada, H. *J. Am. Chem. Soc.* **2010**, *132*, 6292.
- (78) Awazu, K.; Fujimaki, M.; Rockstuhl, C.; Tominaga, J.; Murakami, H.; Ohki, Y.; Yoshida, N.; Watanabe, T. *J. Am. Chem. Soc.* **2008**, *130*, 1676.
- (79) Fox, M. A.; Dulay, M. T. *Chem. Rev.* **1993**, *93*, 341.
- (80) Kamat, P. V. *Chem. Rev.* **1993**, *93*, 267.
- (81) Legrini, O.; Oliveros, E.; Braun, A. M. *Chem. Rev.* **1993**, *93*, 671.
- (82) Kudo, A.; Miseki, Y. *Chem. Soc. Rev.* **2009**, *38*, 253.
- (83) An, C. H.; Peng, S. N.; Sun, Y. G. *Adv. Mater.* **2010**, *22*, 2570.
- (84) Fujishima, A.; Honda, K. *Nature* **1972**, *238*, 37.
- (85) Kormann, C.; Bahnemann, D. W.; Hoffmann, M. R. *Environ. Sci. Tech.* **1991**, *25*, 494.
- (86) Prairie, M. R.; Evans, L. R.; Stange, B. M.; Martinez, S. L. *Environ. Sci. Tech.* **1993**, *27*, 1776.
- (87) Linsebigler, A. L.; Lu, G. Q.; Yates, J. T. *Chem. Rev.* **1995**, *95*, 735.
- (88) Herrmann, J. M. *Catal. Today* **1999**, *53*, 115.
- (89) Tan, S. S.; Zou, L.; Hu, E. *Catal. Today* **2006**, *115*, 269.
- (90) Li, H. X.; Bian, Z. F.; Zhu, J.; Zhang, D. Q.; Li, G. S.; Huo, Y. N.; Li, H.; Lu, Y. F. *J. Am. Chem. Soc.* **2007**, *129*, 8406.

- (91) Chen, X. B. *Chi. J. Catal.* **2009**, *30*, 839.
- (92) Chen, S. F.; Li, J. P.; Qian, K.; Xu, W. P.; Lu, Y.; Huang, W. X.; Yu, S. H. *Nano Res.* **2010**, *3*, 244.
- (93) Ye, M.; Zhang, Q.; Hu, Y.; Ge, J.; Lu, Z.; He, L.; Chen, Z.; Yin, Y. *Chem. Eur. J.* **2010**, *16*, 6243.
- (94) Stafford, U.; Gray, K. A.; Kamat, P. V.; Varma, A. *Chem. Phys. Lett.* **1993**, *205*, 55.
- (95) Riegel, G.; Bolton, J. R. *J. Phys. Chem.* **1995**, *99*, 4215.
- (96) Hurum, D. C.; Agrios, A. G.; Gray, K. A.; Rajh, T.; Thurnauer, M. C. *J. Phys. Chem. B* **2003**, *107*, 4545.
- (97) Zhang, Z. Y.; Zuo, F.; Feng, P. Y. *J. Mater. Chem.* **2010**, *20*, 2206.
- (98) Zhang, L. W.; Fu, H. B.; Zhu, Y. F. *Adv. Funct. Mater.* **2008**, *18*, 2180.
- (99) Yun, H. J.; Lee, H.; Joo, J. B.; Kim, W.; Yi, J. *J. Phys. Chem. C* **2009**, *113*, 3050.
- (100) Joo, J. B.; Zhang, Q.; Lee, I.; Dahl, M.; Zaera, F.; Yin, Y. D. *Adv. Funct. Mater.* **2012**, *22*, 166.
- (101) Joo, J. B.; Zhang, Q.; Dahl, M.; Lee, I.; Goebel, J.; Zaera, F.; Yin, Y. D. *Energ. Environ. Sci.* **2012**, *5*, 6321.
- (102) Ferrere, S.; Gregg, B. A. *J. Am. Chem. Soc.* **1998**, *120*, 843.
- (103) Adachi, M.; Murata, Y.; Takao, J.; Jiu, J. T.; Sakamoto, M.; Wang, F. M. *J. Am. Chem. Soc.* **2004**, *126*, 14943.
- (104) Argazzi, R.; Bignozzi, C. A.; Yang, M.; Hasselmann, G. M.; Meyer, G. J. *Nano Lett.* **2002**, *2*, 625.
- (105) Granados-Oliveros, G.; Paez-Mozo, E. A.; Ortega, F. M.; Ferronato, C.; Chovelon, J. M. *Appl. Catal. B* **2009**, *89*, 448.
- (106) Emeline, A. V.; Kuznetsov, V. N.; Rybchuk, V. K.; Serpone, N. *Int. J. Photoenergy* **2008**, *1*.
- (107) Anpo, M.; Takeuchi, M. *J. Catal.* **2003**, *216*, 505.
- (108) Choi, W. Y.; Termin, A.; Hoffmann, M. R. *J. Phys. Chem.* **1994**, *98*, 13669.
- (109) Li, F. B.; Li, X. Z.; Hou, M. F. *Appl. Catal. B* **2004**, *48*, 185.
- (110) Sato, S. *Chem. Phys. Lett.* **1986**, *123*, 126.

- (111) Asahi, R.; Morikawa, T.; Ohwaki, T.; Aoki, K.; Taga, Y. *Science* **2001**, *293*, 269.
- (112) Sakthivel, S.; Kisch, H. *Angew. Chem. Int. Ed.* **2003**, *42*, 4908.
- (113) Khan, S. U. M.; Al-Shahry, M.; Ingler, W. B. *Science* **2002**, *297*, 2243.
- (114) Graciani, J.; Alvarez, L. J.; Rodriguez, J. A.; Sanz, J. F. *J. Phys. Chem. C* **2008**, *112*, 2624.
- (115) Emeline, A.; Kuznetsov, V.; Rybchuk, V.; Serpone, N. *Int. J. Photoenergy* **2008**, *2008*, 1.
- (116) Batzill, M.; Morales, E. H.; Diebold, U. *Phys. Rev. Lett.* **2006**, *96*, 026103.
- (117) Nambu, A.; Graciani, J.; Rodriguez, J. A.; Wu, Q.; Fujita, E.; Sanz, J. F. *J. Chem. Phys.* **2006**, *125*, 094706.
- (118) Ye, M.; Zhang, Q.; Hu, Y.; Ge, J.; Lu, Z.; He, L.; Chen, Z.; Yin, Y. *Chem. Eur. J.* **2010**, *16*, 6243.
- (119) Zhang, Q.; Joo, J.-B.; Lu, Z.; Dahl, M.; Oliveira, D.; Ye, M.; Yin, Y. *Nano Res.* **2011**, *4*, 103.
- (120) Corma, A.; Serna, P. *Science (Washington, DC, U. S.)* **2006**, *313*, 332.
- (121) Das, B.; Subramaniam, S.; Melloch, M. R. *Semicond Sci Tech* **1993**, *8*, 1347.
- (122) Vieu, C.; Carcenac, F.; Pepin, A.; Chen, Y.; Mejias, M.; Lebib, A.; Manin-Ferlazzo, L.; Couraud, L.; Launois, H. *Appl Surf Sci* **2000**, *164*, 111.
- (123) Pastoriza-Santos, I.; Liz-Marzan, L. M. *J. Mater. Chem.* **2008**, *18*, 1724.
- (124) Millstone, J. E.; Hurst, S. J.; Metraux, G. S.; Cutler, J. I.; Mirkin, C. A. *Small* **2009**, *5*, 646.
- (125) Mayer, K. M.; Hafner, J. H. *Chem Rev* **2011**, *111*, 3828.
- (126) Jones, M. R.; Osberg, K. D.; Macfarlane, R. J.; Langille, M. R.; Mirkin, C. A. *Chem. Rev.* **2011**, *111*, 3736.
- (127) Rycenga, M.; Cobley, C. M.; Zeng, J.; Li, W. Y.; Moran, C. H.; Zhang, Q.; Qin, D.; Xia, Y. N. *Chem. Rev.* **2011**, *111*, 3669.
- (128) Kelly, K. L.; Coronado, E.; Zhao, L. L.; Schatz, G. C. *J. Phys. Chem. B* **2003**, *107*, 668.
- (129) Jin, R. C.; Cao, Y. W.; Mirkin, C. A.; Kelly, K. L.; Schatz, G. C.; Zheng, J. G. *Science* **2001**, *294*, 1901.

- (130) Jin, R. C.; Cao, Y. C.; Hao, E. C.; Metraux, G. S.; Schatz, G. C.; Mirkin, C. A. *Nature* **2003**, *425*, 487.
- (131) Maillard, M.; Huang, P. R.; Brus, L. *Nano Lett.* **2003**, *3*, 1611.
- (132) Xue, C.; Mirkin, C. A. *Angew Chem Int Edit* **2007**, *46*, 2036.
- (133) Sun, Y. G.; Xia, Y. N. *Adv Mater* **2003**, *15*, 695.
- (134) Xue, C.; Metraux, G. S.; Millstone, J. E.; Mirkin, C. A. *J. Am. Chem. Soc.* **2008**, *130*, 8337.
- (135) Zhang, J.; Langille, M. R.; Mirkin, C. A. *J. Am. Chem. Soc.* **2010**, *132*, 12502.
- (136) Chen, S. H.; Carroll, D. L. *Nano Lett.* **2002**, *2*, 1003.
- (137) Sun, Y. G.; Mayers, B.; Xia, Y. N. *Nano Lett.* **2003**, *3*, 675.
- (138) Xiong, Y.; Siekkinen, A. R.; Wang, J.; Yin, Y.; Kim, M. J.; Xia, Y. *J. Mater. Chem.* **2007**, *17*, 2600.
- (139) Sun, Y. G.; Wiederrecht, G. P. *Small* **2007**, *3*, 1964.
- (140) Hao, E. C.; Kelly, K. L.; Hupp, J. T.; Schatz, G. C. *J. Am. Chem. Soc.* **2002**, *124*, 15182.
- (141) Jiang, L. P.; Xu, S.; Zhu, J. M.; Zhang, J. R.; Zhu, J. J.; Chen, H. Y. *Inorg. Chem.* **2004**, *43*, 5877.
- (142) Zhang, Q.; Hu, Y.; Guo, S.; Goebel, J.; Yin, Y. *Nano Lett.* **2010**, *10*, 5037.
- (143) Jiang, X. C.; Chen, C. Y.; Chen, W. M.; Yu, A. B. *Langmuir* **2010**, *26*, 4400.
- (144) Zeng, J.; Tao, J.; Li, W.; Grant, J.; Zhu, Y.; Xia, Y. *Chem. Asian J.* **2011**, *6*, 376.
- (145) Zeng, J.; Xia, X.; Rycenga, M.; Henneghan, P.; Li, Q.; Xia, Y. *Angew Chem Int Edit* **2011**, *50*, 244.
- (146) Frank, A. J.; Cathcart, N.; Maly, K. E.; Kitaev, V. *J. Chem. Educ.* **2010**, *87*, 1098.
- (147) Wulff, G. Z. *Kristallogr.* **1901**, *34*, 449.
- (148) Elechiguerra, J. L.; Reyes-Gasga, J.; Yacaman, M. J. *J. Mater. Chem.* **2006**, *16*, 3906.
- (149) Leontidis, E.; Kleitou, K.; Kyprianidou-Leodidou, T.; Bekiari, V.; Lianos, P. *Langmuir* **2002**, *18*, 3659.
- (150) Tao, A. R.; Habas, S.; Yang, P. D. *Small* **2008**, *4*, 310.

- (151) Berriman, R. W.; Herz, R. H. *Nature* **1957**, *180*, 293.
- (152) Hamilton, D. R.; Seidensticker, R. G. *J. Appl. Phys.* **1960**, *31*, 1165.
- (153) Hosoya, Y.; Urabe, S. *J Imaging Sci Techn* **1998**, *42*, 487.
- (154) Germain, V.; Li, J.; Ingert, D.; Wang, Z. L.; Pileni, M. P. *J. phys. Chem. B* **2003**, *107*, 8717.
- (155) Rocha, T. C. R.; Zanchet, D. *J. Phys. Chem. C* **2007**, *111*, 6989.
- (156) Aherne, D.; Ledwith, D. M.; Gara, M.; Kelly, J. M. *Adv. Funct. Mater.* **2008**, *18*, 2005.
- (157) Xia, Y.; Xiong, Y. J.; Lim, B.; Skrabalak, S. E. *Angew Chem Int Edit* **2009**, *48*, 60.
- (158) Gabaldon, J.; Bore, M.; Datye, A. *Top. Catal.* **2007**, *44*, 253.
- (159) Granqvist, C. G.; Buhrman, R. A. *Appl. Phys. Lett.* **1975**, *27*, 693.
- (160) Datye, A. K.; Xu, Q.; Kharas, K. C.; McCarty, J. M. *Catal. Today* **2006**, *111*, 59.
- (161) Narayanan, R.; El-Sayed, M. A. *Nano Lett.* **2004**, *4*, 1343.
- (162) Ma, Z.; Zaera, F. *Surf. Sci. Rep.* **2006**, *61*, 229.
- (163) Rioux, R. M.; Song, H.; Hoefelmeyer, J. D.; Yang, P.; Somorjai, G. A. *J. Phys. Chem. B* **2005**, *109*, 2192.
- (164) Narayanan, R.; El-Sayed, M. A. *J. Phys. Chem. B* **2005**, *109*, 12663.



## Chapter 2

### Silver Nanoplates: Synthesis, Engineering, and Stabilization

#### 2.1 Introduction

Colloidal noble metal nanoparticles, especially gold (Au) and silver (Ag), have proven to be good candidates for applications in catalysis,<sup>1,2</sup> surface-enhanced Raman scattering (SERS),<sup>3,4</sup> biosensors,<sup>5</sup> and plasmonics,<sup>6</sup> of which chemical and biological sensing are the most promising. Most of these attractive applications are based on their surface plasmon resonance (SPR) property, which strongly depends on their specific composition, size, shape, local dielectric environment, and electromagnetic interactions with proximate particles.<sup>7-13</sup> Recently, from both theoretical and experimental study, it has been realized that particle shape plays an important role in determining the wavelength of their plasmon bands. Great effort has therefore been devoted to controlling the shape of noble metal nanoparticles. For example, excellent work has been done to synthesize silver nanoparticles with shapes varying from spheres to cubes,<sup>14,15</sup> polyhedrons,<sup>16</sup> plates,<sup>17-23</sup> wires,<sup>24</sup> which greatly broaden the range of the SPR wavelength and now can extend it to near IR range.<sup>25</sup>

Silver nanoplates, also referred to as nanoprisms or nanodisks, are two dimensional plasmonic nanostructures that have attracted intensive attention due to their strong

shape-dependent optical properties and related applications.<sup>26-30</sup> When the lateral dimension of silver nanoplates is much larger than the thickness, they possess an extreme degree of anisotropy, which favors a high tunability of their localized surface plasmon resonance (LSPR) and therefore generates maximum electromagnetic-field enhancement.<sup>31</sup> After the seminal report by Mirkin et al. on the photo-induced synthesis of silver nanoplates in 2001,<sup>18</sup> a variety of solution based strategies have been developed by many other groups to synthesize silver nanoplates, including photochemical processes,<sup>32-37</sup> ligand-assisted chemical reductions,<sup>38-40</sup> electrochemical synthesis,<sup>41</sup> templating procedures,<sup>42</sup> and sonochemical routes.<sup>43</sup> Among all these methods, direct chemical reduction has been the most popular due to the considerably high yield and relatively simple setups and procedures which show promise for large scale production.<sup>44-48</sup>

However, up to date, although numerous mechanisms have been proposed to explain the experimental phenomena, there is no general understanding that can properly explain everything. The lack of deep understanding of the synthetic systems also makes it difficult to reproduce many of the reported results with satisfactory yield and quality because some minor unintentional alterations to the reaction conditions may easily disturb nanoplate formation.<sup>49</sup> It is thus highly desired to discover and clarify the underneath mechanism. Additionally, the ability to synthesize silver nanoplates with

tunable size and optical properties is also highly desirable. The concept of selective adhesion of capping ligands has been widely used for preparing inorganic colloidal nanocrystals with anisotropic shapes.<sup>9</sup> In general, the introduction of an organic molecule that selectively adheres to a particular crystal facet of a growing nanocrystal can effectively lower the energy and slow the growth rate of that facet relative to the others. This synthetic scheme has been employed for the preparation of many one- and two-dimensional nanostructures of technologically important semiconductors and metals.<sup>50-55</sup> However, it has been gradually realized that preferential anisotropic growth is not only dependent on the selective adhesion of capping ligands, but also on the crystal symmetry of the starting nuclei.<sup>56,57</sup> From this point of view, overgrowth on a pre-formed, well-defined seeds would be a good choice for the anisotropic growth because one needs to only consider the growth step. In consideration of quality of the product, seeded growth also provides much better control over conventional one-pot methods, since the separation of nucleation from growth is also favorable for kinetics control, yielding uniform nanoparticles.<sup>58,59</sup> For example, in their pioneering works, Murphy et al. have explored the multistep procedures for Au nanorods synthesis in which the nucleation and growth are performed in the presence of different reducing agents and capping ligands.<sup>60,61</sup> Since then, the seeded growth method has been successfully applied to many noble metal systems, such as Au, Ag and Pt etc.<sup>62-65</sup>

In principle, one can systematically tune the plasmon band of the nanoparticles by controlling their shape evolution during particle growth. In practice, however, it is usually difficult to quickly stop the reaction and harvest the growing particles at the desired stage. In addition, these intermediate particles are not stable and they usually change shape during storage. As a result, in most cases, to obtain multiple samples with desired plasmon bands, one has to rely on fine tuning of the synthetic conditions such as the concentration of reagents and capping ligands, temperature, etc., which usually leads to low reproducibility and poor predictability because the nucleation and growth of the nanoparticles are very sensitive to the small variations of synthetic conditions. Tailored synthesis of nanoplates with wider tuning of the optical property using a simple setup is still a great challenge. It is generally believed that the growth of nanoplates involves the gradual increase of aspect ratio. However, it is impractical to arrest the growth of nanoplates to achieve desired aspect ratio and plasmonic properties in a relatively short range because the reaction is usually so fast that the nanoparticles quickly evolve into plates with large aspect ratios. Additionally, the as-synthesized products are generally unstable, and will gradually convert to more stable forms along with a shift of the plasmon band. Achieving precise control of the synthesis, long term stability, and wide plasmon tunability of Ag nanoplates has been the subject of a number of recent studies.<sup>66,67</sup>

In this Chapter, we first reveal the specific roles of each reagent in the chemical reduction route to silver nanoplates through a comprehensive study, as described in **Section 2.3**.<sup>68</sup> This significantly refined understanding allows us to develop an efficient and highly reproducible process for making Ag nanoplates with controllable edge length and thickness as well as desired surface plasmon resonance bands. In **Section 2.4**, we report a two-step procedure for the controlled growth of silver nanoplates with extremely high aspect ratios and consequently widely tunable plasmonic bands. With the advantages of precise control and high reproducibility, this two-step procedure can conveniently produce nanoplates with high aspect ratios that have not been realized previously by using one-step reactions. In **Section 2.5**, we describe an unconventional strategy which allows convenient and precisely controlled preparation of highly stable Ag nanoplates with broad tunability in plasmonic property. With the protection from a stabilizer of PVP, the Ag nanoplates can remain stable at room temperature for at least two months without notable changes in their optical properties. And finally in **Section 2.6**, we conclude with a short summary.

## 2.2 Materials and Methods

**Materials** Hydrogen peroxide (H<sub>2</sub>O<sub>2</sub>, 30 wt-%), acetic acid (glacial), sodium hydroxide, and sodium potassium tartrate were purchased from Fisher Scientific. Silver nitrate (AgNO<sub>3</sub>, 99+%), sodium borohydride (NaBH<sub>4</sub>, 99%), ethylene glycol (EG), sodium citrate tribasic dihydrate (TSC, 99%), tricarballic acid (99%), and L-ascorbic acid were obtained from Sigma-Aldrich. Polyvinylpyrrolidone (PVP, M<sub>w</sub> ~ 29,000) was purchased from Fluka. Malonic acid disodium salt monohydrate (99%), succinic acid disodium anhydrous (99%), glutaric acid (99%), oxalic acid (98%), DL-isocitric acid trisodium hydrate (98%), 1,3,5-benzenetricarboxylic acid (98%), pimelic acid (98%) and polyethylene glycol (PEG, M<sub>w</sub> ~ 3500) were purchased from Acros Organics. Adipic acid disodium salt was purchased from TCI America. Diethylene glycol (DEG) was purchased from Alfa Aesar. All chemicals were used as received without further treatment.

**Synthesis of silver nanoplates** In a standard synthetic approach, the total volume of the reaction solution is fixed at 25.00 mL. Typically, a 24.75 mL aqueous solution combining silver nitrate (0.05 M, 50 μL), trisodium citrate (75 mM, 0.5 mL), and H<sub>2</sub>O<sub>2</sub> (30 wt %, 60 μL) was vigorously stirred at room temperature in air. Sodium borohydride (NaBH<sub>4</sub>, 100 mM, 250 μL) was rapidly injected into this mixture to initiate the reduction, immediately leading to a light yellow solution. After ~ 3 min, the colloidal solution turned to a deep

yellow due to the formation of small silver nanoparticles. Within the next several seconds, the morphology started to change from particles to nanoplates accompanied by the solution color changing from deep yellow to red, green, and blue. The entire transition from nanoparticle to nanoplates typically took 2-3 minutes. In some reactions, poly(vinylpyrrolidone) (PVP, weight-average molecular weight  $M_w \sim 29,000$  g/mol, 17.5 mM, 0.1 mL) was added to the original reaction mixture to narrow the plate size distribution and enhance their stability. In the presence of PVP, the transition from light yellow to deep yellow took  $\sim 30$  minutes to occur.

***Seeded growth of silver nanoplates*** Typically, the as-obtained silver nanoplates are centrifuged and washed with water for three times to completely remove PVP molecules and then re-dispersed in 4 mL  $H_2O$ . 1 mL of silver seeds was dispersed in 9 mL  $H_2O$  to get the seed solution. 0.375 mL L-ascorbic acid (0.1 M) and 0.125 mL trisodium citrate (0.075 M) were quickly injected into the solution under magnetic stirring. 20 mL of  $AgNO_3$  (1.0 mM) was mixed with 0.1 mL of sodium citrate (1.5 mM), and then dropwise added into the seed solution through a syringe pump with an injection rate 0.2 mL/min. After reaction for 5 min, 20 mL of the reaction solution (out of 30 mL) was taken out and the remained solution was used as the seeds for the next growth cycle. By repeating this seeded growth process, silver nanoplates with desired sizes could be easily obtained.

***Reconstruction of silver nanoplates through UV irradiation*** The freshly prepared Ag nanoplates are centrifuged and washed with DI water. Irradiating the aqueous solution using a UV light with a wavelength of 365 nm gradually blue-shifts the plasmon band of the nanoplates, which can be directly confirmed by notable color changes. The UV light source is Spectroline Model SB-100P (120 V, 1.05 amp). The solutions are placed ~3 cm away from the lamp.

***Characterization*** The morphology of Ag nanoplates was characterized by using an XL 30 SEM and a Tecnai T12 TEM. A probe-type Ocean Optics HR2000CG-UV-NIR spectrometer was used to measure the UV-Vis spectra of the reaction system to obtain the real-time spectra change during the synthesis of silver nanoplates. The measurement of optical property was conducted by using a Varian Cary 500 double beam scanning UV/Vis/NIR spectrophotometer. In the range of 300-1300 nm, D.I. H<sub>2</sub>O was used as the solvent. Due to the limit of H<sub>2</sub>O, the optical change over 1300 nm was characterized by assembling Ag nanoplates on a quartz slice to form a film. The surface of quartz slice was first treated to be hydrophilic. In detail, the quartz slice was cleaned and ultra-sonicated in ethanol for 5 min, then rinsed with D.I. water and further treated in H<sub>2</sub>SO<sub>4</sub>/H<sub>2</sub>O<sub>2</sub>(volume ratio is 7:3) at about 90 °C for 2 days, and finally washed with water and dried with acetone. The thicknesses of Ag nanoplates were characterized by using atomic force microscope (AFM, Veeco, Multiple) through the tapping mode.



### 2.3 A Systematic Study on the Synthesis of Silver Nanoplates

In the direct chemical reduction scheme, Ag nanoplates are typically prepared by reducing an aqueous solution of  $\text{AgNO}_3$  with  $\text{NaBH}_4$  in the presence of trisodium citrate (TSC), PVP, and  $\text{H}_2\text{O}_2$ .<sup>44,69,70</sup> To investigate the specific roles of each reagent in this system, we start from a simple reduction reaction by simply mixing the silver source  $\text{AgNO}_3$  and the reducing agent  $\text{NaBH}_4$ . Under magnetic stirring, the solution changed color from light yellow to brownish in about 3 min. The brownish color came from large aggregations of silver nanoparticles due to the absence of stabilizer. When PVP and citrate were added either separately or combined, the reactions produced quasi-spherical silver nanoparticles which displayed a sharp plasmon peak at around 400 nm in the extinction spectra (Figure 2.1). This phenomenon confirms the stabilizing effect of these ligands but rules out their immediate shape directing effect. In contrast, when a small amount of  $\text{H}_2\text{O}_2$  was added together with PVP to the reaction, a shoulder around 500 nm appeared, implying the formation of some anisotropic nanoparticles. As evidenced by the TEM image shown in Figure 2.1c, the as-obtained product was a mixture of spherical, rod- and plate-like nanoparticles with a nanoplate yield of  $\sim 10\%$ . These results clearly suggest that  $\text{H}_2\text{O}_2$  can promote the formation of anisotropic structures.

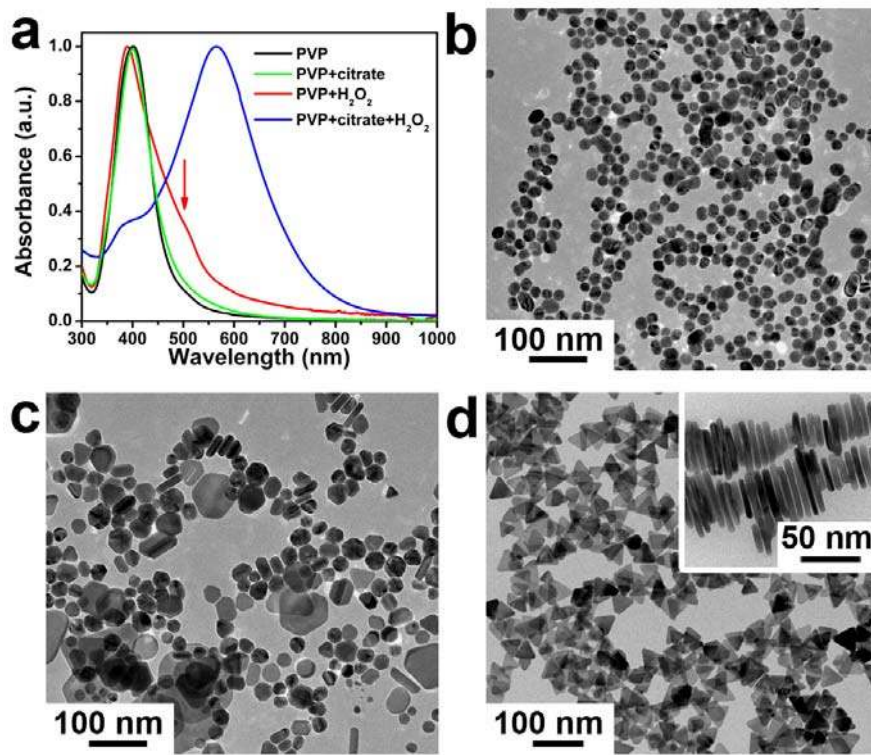


**Figure 2.1** (a) UV/Vis spectra of silver nanoparticles synthesized in different conditions; (b-d) TEM images showing the morphology of products prepared in the presence of (b) PVP only, (c) PVP and H<sub>2</sub>O<sub>2</sub>, and (d) PVP, citrate, and H<sub>2</sub>O<sub>2</sub> together. The inset in (d) shows a TEM image in which Ag nanoplates stand vertically upon their edges. Reproduced with permission from Ref. 68. Copyright © 2011 American Chemical Society.

When citrate, PVP and  $\text{H}_2\text{O}_2$  were added with an appropriate ratio into the reaction, Ag nanoplates with high yield and great uniformity can be obtained, as shown in Figure 2.1d. Such silver nanoplates tend to stack upon each other face-to-face and stand vertically on their edges, making it convenient to estimate their thicknesses (inset in Figure 2.1d). As we will discuss in more detail later, the combination of  $\text{H}_2\text{O}_2$  and citrate at the appropriate ratio can also produce silver nanoplates of similar quality and yield, suggesting that PVP is non-essential to the formation of silver nanoplates. As  $\text{H}_2\text{O}_2$  appears to be the most critical reagent for the plate formation, we have studied its role more systematically. To simplify the reaction, we prepared silver nanoplates in the presence of citrate but without PVP under the typical conditions described in the experimental section. Without the addition of  $\text{H}_2\text{O}_2$ , only quasi-spherical silver nanoparticles can be obtained after about 3 min of reaction, as indicated by the yellow color of as-prepared colloids. When the concentration of  $\text{H}_2\text{O}_2$  was increased to 5 mM, a sharp peak around 450 nm appeared along with a shoulder at around 400 nm (Figure 2.2a), suggesting the formation of both plate-like structures and spherical nanoparticles, which has also been confirmed by TEM characterization. The sharp characteristic peak of silver nanoparticles at  $\sim 400$  nm disappeared as the concentration of  $\text{H}_2\text{O}_2$  was increased to 10 mM. The weak shoulder around 380-420 nm can be attributed to the in-plane quadrupole resonance of silver nanoplates. When the concentration of  $\text{H}_2\text{O}_2$

was further increased to 20 mM, the quadrupole resonance became more pronounced and the dipole resonance red-shifted to  $\sim 600$  nm. To investigate the detailed formation process of the silver nanoplates, we monitored the change in the SPR peak during the nucleation and growth of silver nanoplates under the standard conditions with 20 mM  $\text{H}_2\text{O}_2$ . Upon the addition of  $\text{NaBH}_4$ , the originally colorless solution became light yellow immediately, suggesting the reduction of silver. However, the characteristic peak of silver nanoparticles around 400 nm is not pronounced, as shown by the bottommost curve in the inset of Figure 2.2b. Instead, there is a very strong absorption band in the short UV range ( $< 300$  nm, not shown), implying the existence of small silver nanoparticles.<sup>71,72</sup> After  $\sim 3$  min of reaction, the light yellow solution turned deep yellow in the span of several seconds, suggesting the formation of silver nanoparticles. The change in the optical property of the colloidal solution was recorded using a UV/Vis spectrometer. As shown in the inset of Figure 2.2b, once the formation of nanoparticles began, the intensity of the characteristic peak at 400 nm increased quickly. In about 5 seconds, the peak rose to the maximum. The color of the reaction solution then quickly changed from deep yellow to red, green, and finally blue, as evidenced by the UV/Vis spectra shown in Figure 2.2b. The intensity of the characteristic peak of spherical nanoparticles quickly decreased, indicating their consumption during the reaction.

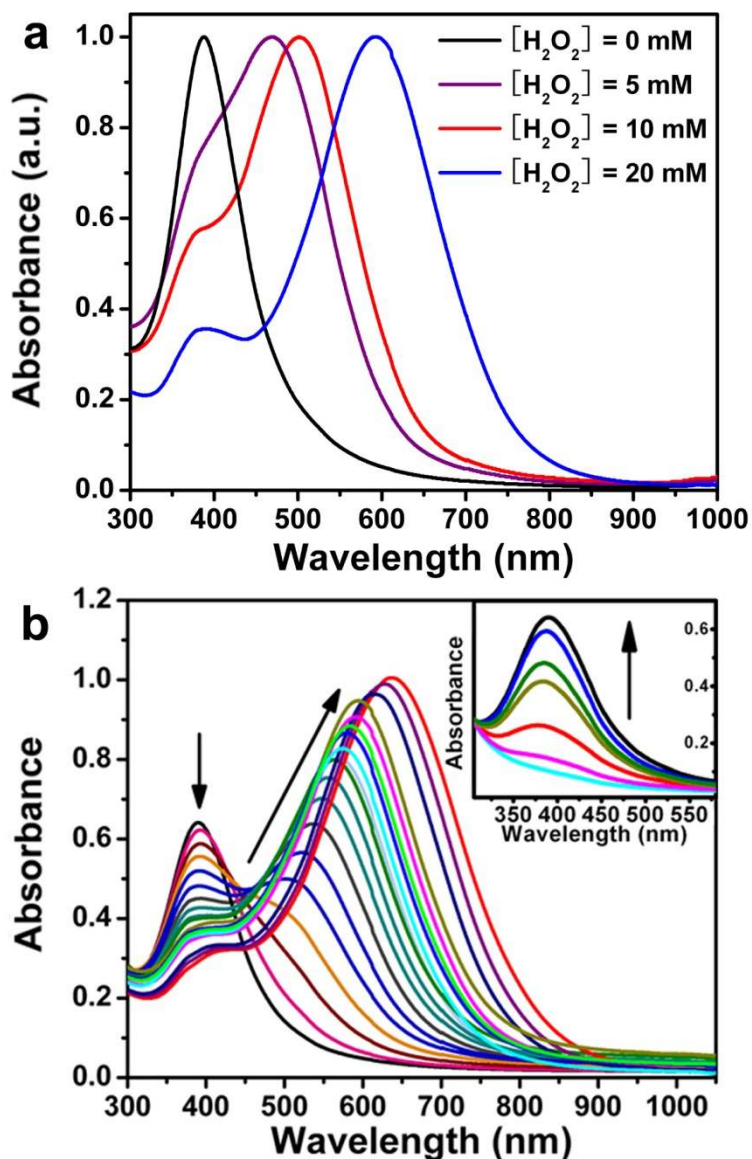
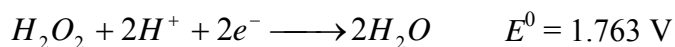


**Figure 2.2** (a) UV/Vis spectra of silver nanoparticles obtained by controlling the concentration of  $\text{H}_2\text{O}_2$ ; (b) real-time measurement of the formation of silver nanoplates with a time interval of 7.5 s. The inset in (b) shows the UV/Vis spectra of the initiation stage during the synthesis of silver nanoplates with a time interval of 0.75 s. Reproduced with permission from Ref. 68. Copyright © 2011 American Chemical Society.

At the same time, another peak at  $\sim 500$  nm emerged and gradually red-shifted to longer wavelengths, implying the formation and growth of silver nanoplates. The formation and development of silver nanoplates took about 2-3 min. To further clarify the role of  $H_2O_2$ , the reaction process in the absence of  $H_2O_2$  has also been studied. Only a small peak at around 400 nm was noticeable in the UV/Vis spectra, indicating the formation of large silver nanoparticles at the initial stage.<sup>73</sup>

It is well known that  $H_2O_2$  is a powerful oxidizing agent.<sup>74</sup> The standard potential in the peroxide-water couple is dependent on the pH value of the solution.<sup>75,76</sup> In acidic solutions:



And in alkaline solutions:



Since the potentials under both conditions are higher than that of  $Ag^+/Ag$  ( $E^0 = 0.7996$  V),  $H_2O_2$  can be used as an effective etchant to dissolve metallic silver. The results thus suggest that  $H_2O_2$  acts as an oxidant from the very beginning of the reaction and there should be a dynamic equilibrium between the reduction of silver ions by  $NaBH_4$  and oxidative dissolution of metallic silver by  $H_2O_2$ . Based on this understanding and the aforementioned experimental observations, we propose here a plausible mechanism for

the formation of nanoplates: upon the injection of  $\text{NaBH}_4$ , silver ions are partially reduced to form small silver nanoparticles, which are temporarily stabilized by the adsorption of citrate and borohydride ions. At the same time, extensive growth of the small nanoparticles to nanoparticles is inhibited due to etching by  $\text{H}_2\text{O}_2$ . As the result of dynamic equilibrium between the reduction and oxidation, silver stays in the form of small nanoparticles which appear light yellow in color. When  $\text{NaBH}_4$  is consumed over time, the protection from borohydride ions is weakened, allowing the production of silver nuclei with various structures, as supported by the rise of a sharp peak around 400 nm (inset in Figure 2.2b). Due to the Ag-citrate coordinating interaction and the presence of the powerful etchant  $\text{H}_2\text{O}_2$ , the nuclei are silver nanoparticles containing many defects, including the twinned defects that favor the planar growth into plate shapes. Although it remains an interesting assumption for future exploration, we suspect that  $\text{H}_2\text{O}_2$  can remove the relatively unstable nanoparticles at this stage, leaving only the most stable ones. With the protection of citrate ions that preferentially bind to (111) facets, plate-structured silver nuclei possess the highest relative stability because the majority of the surface is capped by ligands. Their expansion along the twin plane into high-aspect-ratio nanoplates is enhanced by the fast growth of side facets, typically (100). Thus, the net effect of  $\text{H}_2\text{O}_2$  in this reaction, in synergy with citrate ions, is to promote the nucleation of plates by removing less stable silver nanoparticles of other structures.

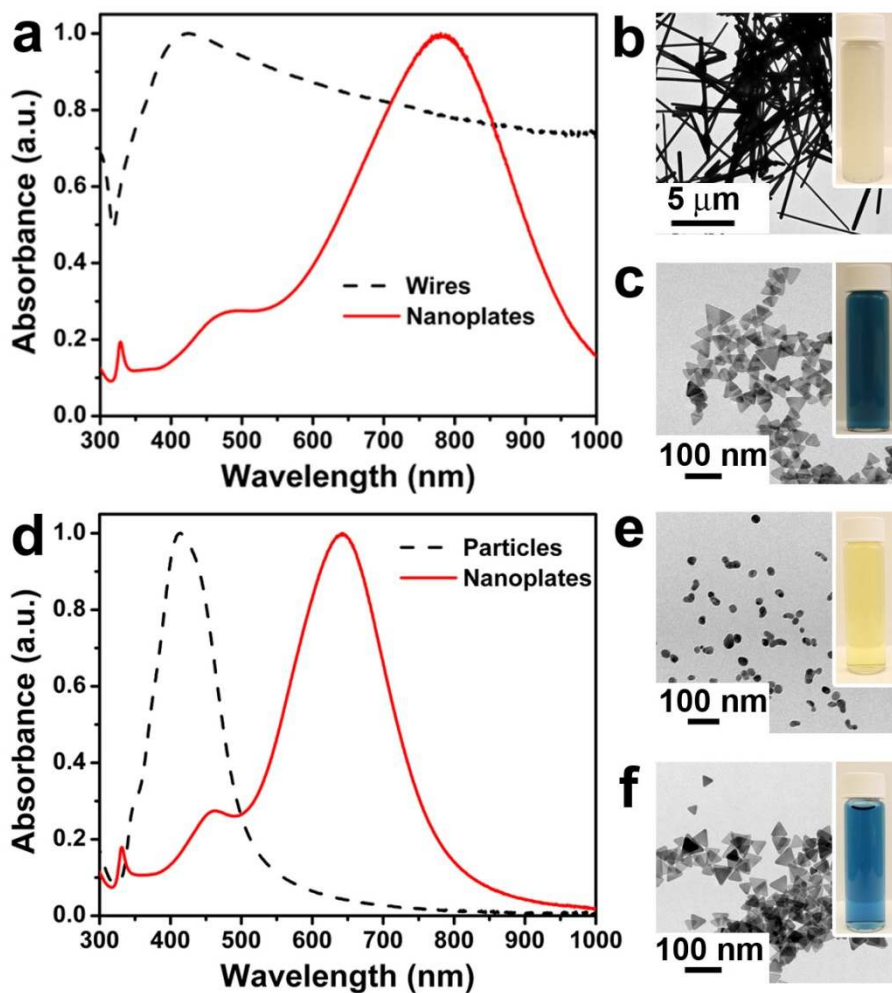
Understanding the deterministic role of  $\text{H}_2\text{O}_2$  in plate formation allows us to replace other components in the synthesis. We found it possible to use metallic silver, instead of silver salt, as the silver source for nanoplate synthesis. In their first successful preparation of silver nanoplates, Mirkin and co-workers converted silver nanospheres into triangular nanoplates through a photo-induced method.<sup>18</sup> It was later pointed out that only small nanoparticles can be converted due to their lower redox potential, while larger nanoparticles did not work well in the photo-conversion process.<sup>36</sup> Some other groups reported that silver nanoplates can also be prepared by thermally treating silver nanospheres in the presence of surfactants, typically citrate.<sup>39</sup> However, until now, conversion was believed to be limited to small nanoparticles that are unstable under the specific reaction conditions. By using  $\text{H}_2\text{O}_2$  as the etchant, we have found that all metallic silver particles, regardless of their size and shape, can be directly converted to silver nanoplates.

Figure 2.3 shows two examples of nanoplate synthesis by starting with pre-formed Ag nanowires and nanoparticles. In both cases, metallic silver is first dispersed in water, followed by the addition of citrate. Once a suitable amount of  $\text{H}_2\text{O}_2$  has been added, the reaction solution gradually becomes colorless with the appearance of small bubbles due to the partial decomposition of  $\text{H}_2\text{O}_2$ .  $\text{NaBH}_4$  is then added to reduce  $\text{Ag}^+$  back to  $\text{Ag}^0$ . The solution changes gradually from colorless to light yellow, yellow, red, and blue,



indicating the formation of silver nanoplates. As shown in Figures 2.3a-c, silver nanowires with lengths of up to tens of micrometers can be converted to silver nanoplates, as confirmed by the UV/Vis spectra and TEM image. During the conversion process, the original gray solution was changed to a dark blue solution. Figures 2.3d-f show another example, in which irregular silver nanoparticles can be converted to silver nanoplates, which is supported by the corresponding UV/Vis spectra and TEM characterization. These results rule out the possibility of an essential role for nitrate ions in the formation of silver nanoplates. From a synthesis point of view, the use of metallic silver as the source ensures a higher degree of reproducibility as there is less possibility of introducing disturbances such as the anions of the silver salt to the reaction.

Serving as a shape-directing agent and stabilizer, citrate has been widely used in the preparation of colloidal noble metal nanoparticles, particularly Au and Ag.<sup>62,77</sup> Since the first report on the synthesis of silver nanoplates,<sup>18</sup> citrate has been considered an essential component. In the photochemical synthetic strategy, Xue and Mirkin found that citrate ion serves as a bi-functional reagent: not only can it reduce  $\text{Ag}^+$  to  $\text{Ag}^0$  in the presence of light irradiation, but it also helps to form plate-structured silver nanoparticles, although the mechanism was not discussed in more depth.<sup>36</sup> They also found that citrate was an essential component in the synthesis, which could not be replaced by other carboxyl compounds, such as tricarballoylate, citramalate, and aconitate.



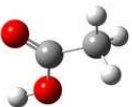
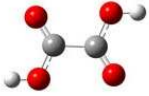





**Figure 2.3** UV/Vis spectra and TEM images showing that both (a-c) silver nanowires with lengths of up to 10  $\mu\text{m}$  and (d-f) silver nanoparticles with irregular shapes can be converted to silver nanoplates in the presence of  $\text{H}_2\text{O}_2$ . Reproduced with permission from Ref. 68. Copyright © 2011 American Chemical Society.

Isocitrate is the only other carboxyl molecule that was found to be able to replace citrate, however the resulting yield and quality was considerably lower.<sup>36</sup> Although many groups have tried to determine the role of citrate,<sup>45,46,78</sup> the nature of citrate ions in the formation of silver nanoplates is still unclear, which has made the citrate ion a “magic” ligand. It is widely accepted that citrate acts as a capping agent as it can selectively bind to {111} facets and thus effectively block the growth along the vertical axis and only allow extensive growth along the lateral direction.<sup>39</sup> Consistent with this assumption, Kiline and Xia et al. pointed out that theoretically citric acid can preferentially bind to Ag (111) facets due to the fact that the approximate 3-fold symmetry of citric acid matches that of Ag (111) and results in four Ag-O bonds, while it forms only two bonds with Ag (100) because of the geometry mismatch.<sup>79</sup> Unfortunately, no prediction was given regarding whether any other molecules could play the same role in the synthesis of silver nanoplates. Since we have determined that the key in the synthesis of silver nanoplates is the formation of plate-structured nuclei in the presence of hydrogen peroxide, we are now able to systematically vary the capping ligands and study their contribution to plate formation.

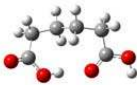
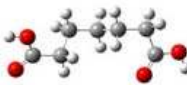





Table 2.1 lists carboxyl compounds that have been used to prepare silver nanoplates in our study and the corresponding yields. It is unsurprising that no silver nanoplates could be obtained when acetate was used as a substitute for citrate since there was no

geometric difference in its binding affinity to (111) or (100) facets. We then tested the use of dicarboxyl compounds as capping agents. Although oxalate has two carboxylate groups, no nanoplates were formed when it was used to replace citrate, which might be attributed to the size mismatch between the molecule and the atoms on the Ag (111) surface.<sup>79</sup> Surprisingly, many other dicarboxyl molecules can be used to replace citrate and yield a relatively high percentage of plate structures. For example, in the presence of malonate, a red colloid can be obtained, as evidenced by a sharp peak around 500 nm. TEM characterization also confirms the formation of silver nanoplates with a yield of ~80%. When succinate and citramalate were used as the capping agents, silver nanoplates could be achieved with a yield of 100%. To further investigate the role of such carboxyl molecules, we also used long chain carboxyl compounds as substitutes for citrate. The yield of silver nanoplates is highly sensitive to the chain length of the capping agent (Figure 2.4). As the number of carbon atoms between the two nearest carboxylate groups increases beyond 2, the yield of silver nanoplates gradually drops. Based on Kiline and co-workers' simulation, the two side methylene-carboxylate groups of citrate bind to (111) facets, while the closer carboxyl group does not directly bind to the surface. If this conclusion is correct, the ideal number of carbon atoms between two side carboxylate groups should be three.

**Table 2.1** Carboxyl compounds with different numbers of carboxylate groups and chain lengths that have been used as the capping agent to prepare silver nanoplates. Adapted with permission from Ref. 68. Copyright © 2011 American Chemical Society.

Name	Structure	Distance between two nearest carboxylic groups (Å)	Number of carbon between two nearest carboxylate groups	Yield of plates
Acetic acid		N/A	N/A	~ 0%
Oxalic acid		2.69	0	~ 0%
Malonic acid		2.68	1	~80%
Succinic acid		2.78	2	~100%
Citramalic acid		3.82	2	~100%
Tartaric acid		3.26	2	~80%
Glutaric acid		3.26	3	~50%

**Table 2.1** (Continued) Carboxyl compounds with different numbers of carboxylate groups and chain lengths that have been used as the capping agent to prepare silver nanoplates. Adapted with permission from Ref. 68. Copyright © 2011 American Chemical Society.

Name	Structure	Distance between two nearest carboxylic groups (Å)	Number of carbon between two nearest carboxylate groups	Yield of plates
Adipic acid		2.87	4	~20%
Pimelic acid		6.62	5	~ 0%
Citric acid		3.12	2	~100%
Isocitric acid		3.09	2	~90%
cis-Aconitic acid		2.82	2	~90%
Tricarballic acid		3.18	2	~85%
Trimesic Acid		4.76	3	~ 0%

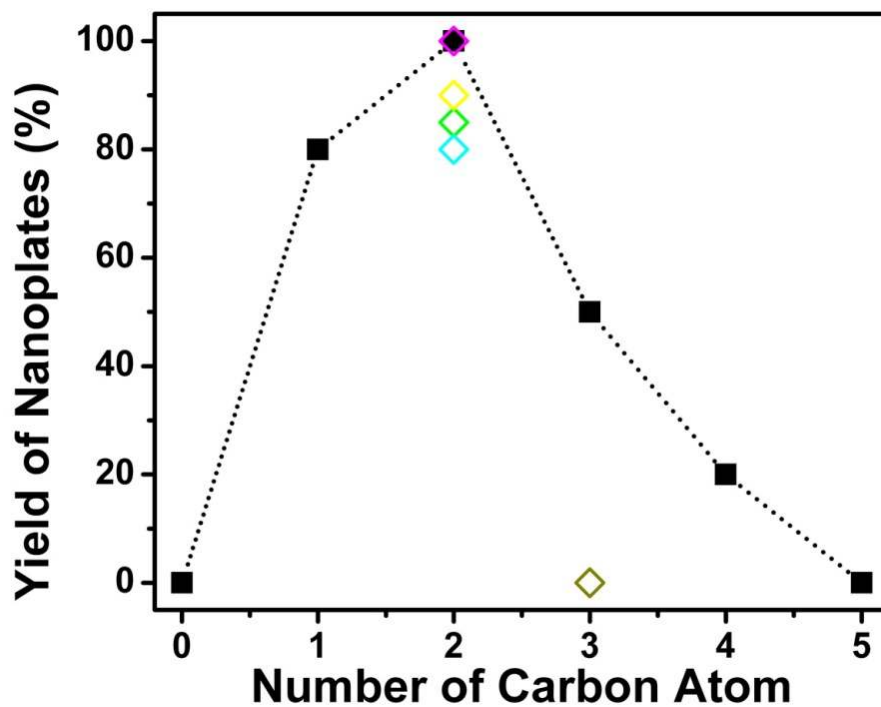


**Figure 2.4** The yield of silver nanoplates as a function of the number of carbon atoms between two nearest carboxylate groups when carboxyl compounds are used as the capping agent. Reproduced with permission from Ref. 68. Copyright © 2011 American Chemical Society.

However, in our study, glutarate, with three carbon atoms in between two side carboxylate groups, can only produce silver nanoplates with a yield around 50%. If we consider the two nearest carboxylate groups of citrate, the number of carbon atoms between each group is two, which is in great agreement with the cases of succinate and citramalate. We therefore conclude that the preferential binding of citrate to silver may come from the two nearest carboxylate groups rather than two side carboxylate groups. This was further confirmed by using tri-carboxyl compounds as the capping agent. As listed in Table 2.1, cis-aconate, tricarballylate, and isocitrate can all be used to prepare silver nanoplates with relatively high yield (85%-90%). In the case of trimesic acid, the low yield may come from its very low solubility in water, which prevents a sufficient supply of capping agent for surface protection. Although more advanced analyzing tools are still needed to probe the face-selective binding, it is now clear that citrate is not a "magic" ligand that leads to the formation of silver nanoplates, rather it can be replaced by many other compounds containing dicarboxylate groups with proper molecular structures. The 3D structure of such carboxylate compounds should be critical in determining the face-selective binding.<sup>79</sup> A theoretical simulation of such compounds has been carried out to figure out their 3D structures, as listed in Table 2.1. Although the simulation results can give us some useful information, e.g., the distance between two nearest carboxylic groups, a deeper and more comprehensive computation based on the



interaction between carboxylate groups and silver surface will be executed to study the origin of the selectivity.

We have found that citrate ions alone can stabilize the silver nanoplates in addition to their face-selective protection property. In contrast to Mirkin and co-workers' study in which only ill-defined particle aggregates could be formed without PVP or a similarly strong surfactant, BSPP, we find that there is a narrow window of synthetic conditions in which citrate can stabilize the as-obtained silver nanoplates without the help of other ligands. When the concentration of  $\text{H}_2\text{O}_2$  was 20 mM, silver nanoplates could be obtained with high yield (Figure 2.2a). However, due to the presence of excess  $\text{H}_2\text{O}_2$ , the as-obtained plates are not stable and will disappear within several hours. Reducing the concentration of  $\text{H}_2\text{O}_2$  down to 10 mM yielded stable and well-defined triangular nanoplates with a yield of  $\sim 100\%$  (Figures 2.5a, b). The stabilizing effect may come from the adsorption of citrate on the plate surface, rendering it negatively charged and preventing aggregation. Additionally, in the absence of PVP, the initiation time of the reaction is drastically decreased from  $\sim 20\text{-}30$  min to 2-3 min. In other words, PVP molecules can slow down the reaction, mainly owing to their adsorption onto the initial silver nuclei. The exclusion of PVP allows precise control of the SPR band position in a more reproducible manner, likely due to fewer disturbances over a shorter reaction time.

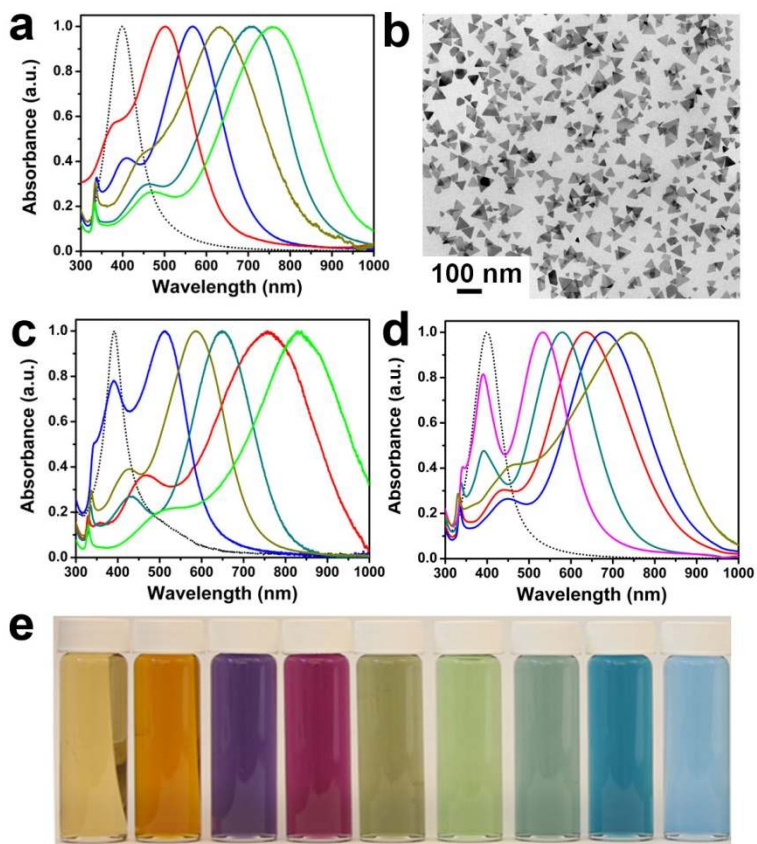


**Figure 2.5** (a) UV/Vis spectra and (b) TEM image showing the preparation of silver nanoplates by using citrate as the sole surfactant; (c) UV/Vis spectra of Ag nanoplates prepared by using PVP as an additional stabilizing agent; (d, e) UV/Vis spectra and digital image of silver nanoplates prepared in the presence of glycerol by tuning the synthetic conditions. Reproduced with permission from Ref. 68. Copyright © 2011 American Chemical Society.

The advantage of having PVP in the reaction is the improvement of the size distribution of the nanoplates. Comparing the samples obtained with/without PVP (Figures 2.1d and 2.5b), although triangular silver nanoplates can be obtained in high yield in both cases, the size distribution of the product in the presence of PVP is narrower, suggesting the size limiting effect of PVP as a typical surfactant. This effect, however, is not exclusive to PVP. We found that many hydroxyl group-containing molecules can be added to the reaction and help improve the size distribution of nanoplates. As shown in Figures 2.5d and 2.5e, in one example, colloidal silver nanoplates with various colors can be obtained in the presence of glycerol. The size distribution also appears narrower than those synthesized with citrate alone. Compared to the results in the presence of PVP (Figure 2.5d), the addition of glycerol shows a similar effect in the synthesis of silver nanoplates, further confirming that PVP is not an essential component in this synthetic strategy. An additional benefit of using the hydroxyl group-containing molecules is the relatively higher stability of the nanoplates against oxidation/ripening, probably due to the reductive nature of the hydroxyl groups. We found many hydroxyl group-containing compounds, including ethanol, ethylene glycol (EG), diethylene glycol (DEG), tetraethylene glycol (TEG), polyethylene glycol (PEG) and polyvinyl alcohol (PVA), can be used in a similar manner to glycerol for synthesizing stable colloidal silver nanoplates with a high yield. Their enhanced stability against oxidation/ripening is

supported by the small shift ( $< 20$  nm) of the plasmonic peak of the nanoplates upon storage in the reaction solution for one week, while control samples synthesized with citrate only or citrate/PVP in combination shifted  $\sim 150$  and  $\sim 100$  nm, respectively.

It has been widely accepted that  $\text{NaBH}_4$  is a relatively strong reducing agent that can be used to reduce  $\text{Ag}^+$  to  $\text{Ag}^0$ . It is usually assumed that a higher concentration of  $\text{NaBH}_4$  will lead to faster production of silver nanoparticles. However, our systematic studies show, for the first time, that borohydride ions can in fact slow down the nanoparticle formation by stabilizing the silver nanoparticles through surface binding. As a result, the initiation time required for nucleation increased with higher concentrations of  $\text{NaBH}_4$  in the reaction system. The same trend has been observed for the reactions with or without ligands and  $\text{H}_2\text{O}_2$ , as shown in Figure 2.6a. In particular, under typical reaction conditions but without any surfactant, the initiation time extended from several seconds to about 3 min with an increased concentration of  $\text{NaBH}_4$  from 0.2 mM to 1.0 mM. The protecting effect of borohydride ions plays a very important role at this nucleation stage, which may come from the adsorption of borohydride ions on silver nanoparticles so that the reaction rate is slowed down.<sup>80</sup> Likewise, the addition of citrate drastically delayed the reaction, as shown in Figure 2.6a. In the presence of citrate, the nucleation time increased from  $\sim 3$  min to  $\sim 30$  min when the concentration of  $\text{NaBH}_4$  increased from 0.2 mM to 1.0 mM. The larger slopes of the cases involving

citrate suggest a possible synergistic stabilizing effect of citrate ions and borohydride ions, which however is difficult to fully interpret at this point.

The change of the nucleation kinetics can be used to effectively control both the thickness and aspect ratio of as-obtained silver nanoplates. As shown in Figure 2.6b, the thickness of silver nanoplates decreases from  $\sim 6$  nm to  $\sim 3.5$  nm as the concentration of  $\text{NaBH}_4$  increases from 0.4 mM to 1.0 mM. This again supports the above assumption of a synergistic stabilizing effect between citrate ions and borohydride ions, where a higher concentration of borohydride ions enhances the preferential binding of citrate to the (111) facet, leading to the formation of thinner nanoplates. Likewise, the aspect ratio increases accordingly from  $\sim 3$  to  $\sim 11$ , which is consistent with the SPR band change. We can thus conclude that  $\text{NaBH}_4$  functions not only as a reducing agent but also works as a capping ligand that contributes to the reaction kinetics and morphology control. Interestingly, as a reducing agent, it does not play an essential role in the formation of silver nanoplates. For instance, we have been able to successfully produce silver nanoplates of considerably good quality by using ascorbic acid or hydrazine in place of  $\text{NaBH}_4$  as the reducing agent.

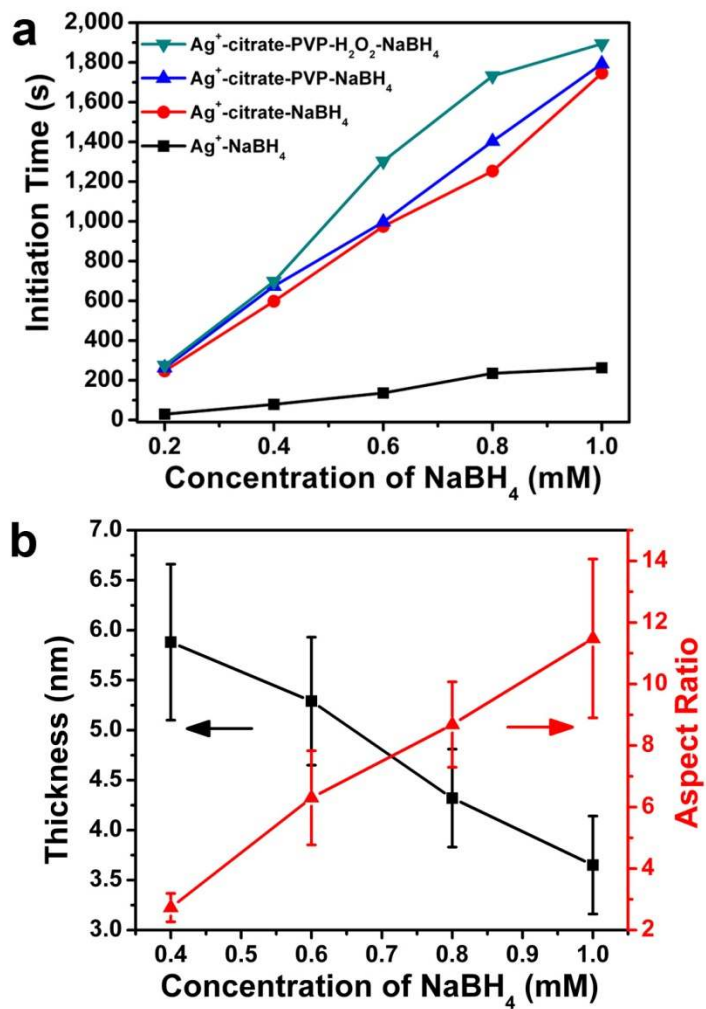
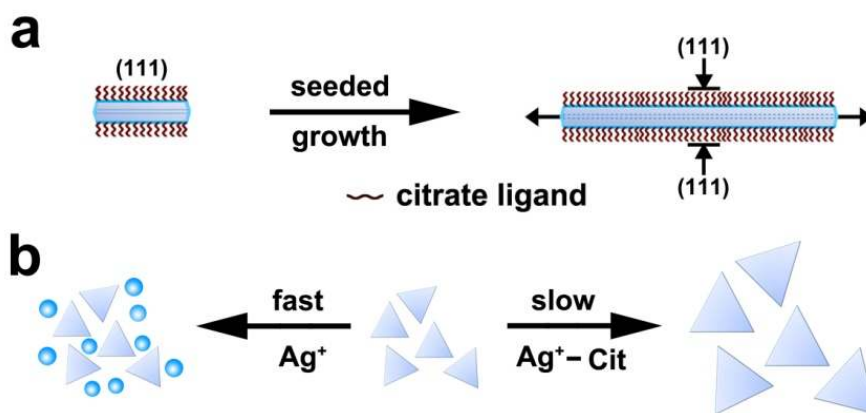


**Figure 2.6** (a) The initiation time and (b) thickness and aspect ratio of as-obtained silver nanoplates as a function of the concentration of NaBH<sub>4</sub>. Reproduced with permission from Ref. 68. Copyright © 2011 American Chemical Society.

## 2.4 Seeded-Growth of Uniform Silver Nanoplates with Tunable Plasmon Band

The selective binding of citrate ligands on (111) facets can effectively block growth along the vertical axis and only allow extensive growth along the lateral axis of the plates, as shown in Scheme 2.1. For the seeded-growth process, generally, there are two competing processes occurring: self-nucleation and epitaxial growth. Based on the Gibbs-Thomson equation, a slow reaction rate as well as a low concentration of monomer is normally favorable for seeded growth, while a fast reaction rate is favorable for the self-nucleation process.<sup>81</sup> To slow down the reaction rate, Ag ion was pretreated with citrate ion to form Ag-citrate complexes, which later can release the citrate anion to help to maintain anisotropic growth.<sup>82</sup> A typical synthesis starts with the preparation of plate-like seeds, followed by a seed-mediated growth process. Triangular Ag nanoplates were prepared through a modified thermal process.<sup>83</sup> To prepare the “seed” solution, PVP molecules were removed by centrifuging and washing with D.I. water for several times. The Ag seeds were re-dispersed in 10 mL water, followed by the addition of a certain amount of sodium citrate and L-ascorbic acid, serving as the surfactant and reducing agent, respectively. In another “growth” solution, AgNO<sub>3</sub> solution was first mixed with sodium citrate and then added dropwise into the “seed” solution using a syringe pump. With the addition of Ag precursor, the light blue solution became dark blue, cyan and finally grayish, showing the change of the Ag nanoplates.



**Scheme 2.1** (a) Schematic illustration of the anisotropic seeded growth of Ag nanoplates based on selective ligand adhesion: The citrate ions selectively protect the  $\{111\}$  basal facets of Ag nanoplates and only allow lateral overgrowth; and (b) Schematic illustration of the consequences of seeded growth at different reaction rates: in this work, Ag-citrate complexes ( $\text{Ag}^+\text{-Cit}$ ) are used as the precursors, which can effectively slow down the reaction rate and minimize the self-nucleation events. Reproduced with permission from Ref. 44. Copyright © 2010 American Chemical Society.



The original seeds are Ag nanoplates with a mean size around 25 nm. Due to the low stability of the small nanoplates, the plate seeds become non-uniform with the sharp corners converting to round ones after removal of the PVP molecules, (Figure 2.7a). After one cycle, the edge length of the silver nanoplates increases to around 130 nm and all of the grown Ag nanoplates present a triangular shape with round corners. From Figure 2.7b, one can clearly see the narrow thickness and large aspect ratio. With extended overgrowth, the edge length increases and the rounded corners became sharp. Although larger Ag nanoplates cannot stand up vertically, the fact that the electron beam can penetrate through several Ag layers reveals the thin nature of such nanoplates (Figures 2.7c-f). According to the Gibbs-Thomson effect, the sharp corners are the most energetic areas in a triangular nanoplate. As the size of the Ag plates increases, it becomes difficult to retain the sharp corners. As shown in Figures 2.7e-f, with larger particle sizes, the sharp corner is gradually truncated and the final product have some pentagonal and hexagonal nanoplates. Due to the diluted seed concentration (1/3 for each cycle), the number of available active sites in the solution dramatically decreases as the growing cycle continues. As a result, the occurrence of spherical nanoparticles from self-nucleation becomes more pronounced with increased particle size. The yield of nanoplates drops down from ~100% to ~80% with particle size increasing from ~130 nm to ~4000 nm (Figure 2.7).

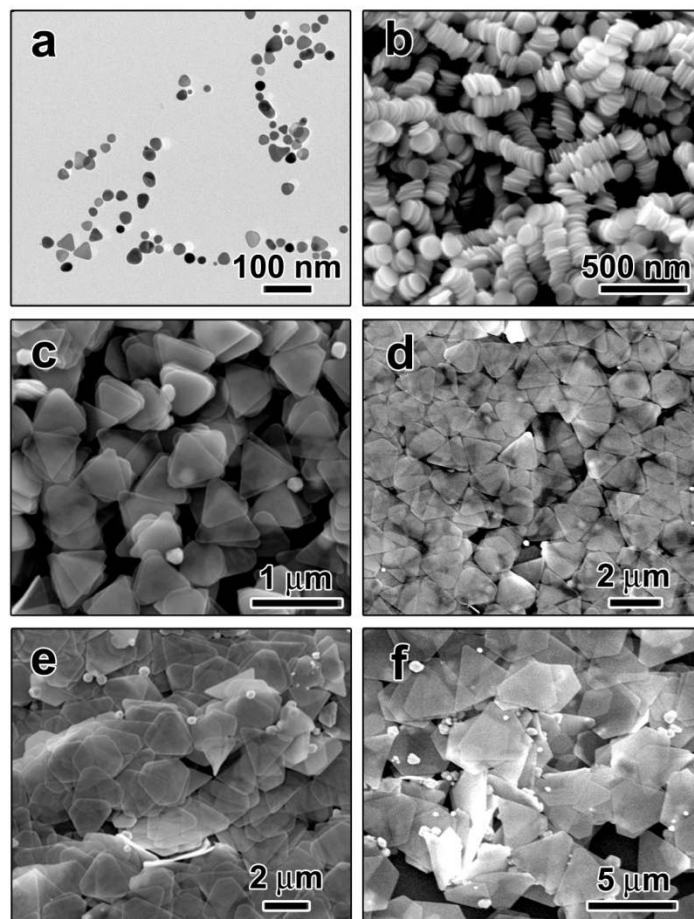


**Figure 2.7** (a) TEM image of the original silver nanoplate seeds; (b-f) SEM images showing the evolution process of Ag nanoplates during the step-wise growth process. Reproduced with permission from Ref. 44. Copyright © 2010 American Chemical Society.

More impressively, a “size focusing” effect has been observed during the seeded-growth process. The inset in Figure 2.8 summarizes the change in edge length over the number of growing cycle. The evolution of the size distribution of the Ag nanoplates during the seeded growth process is depicted in Figure 2.8. The size distribution starts out with a standard deviation of 27.9%. Over the next 7 cycles of overgrowth, the as-obtained Ag nanoplates undergo a size “focusing” and subsequent “defocusing” process. When the size of the silver nanoplates increases to  $\sim 130$  nm, the size distribution is “focused” to around 11.4 %, implying the effective “size focusing” step. After one more cycle of seeded-growth, the as-prepared silver nanoplates with a mean size of  $\sim 570$  nm show the narrowest size distribution with a standard deviation percentage of 7.9%. The size focusing effect occurs due to kinetic control: the smaller nanoparticles grow more rapidly than the larger ones because the surface energy of smaller particles is much higher. In addition, larger particles have a slower growth rate even when the deposition rates of Ag atoms are the same due to the greater ratio of volume versus size for large particles, meaning more Ag is needed to produce a net edge length increase. Further growth “defocuses” the size distribution, i.e., the standard deviations of silver nanoplates gradually increases to 8.9%, 9.8% and 10.9% for the sizes of 1400 nm, 2200 nm and  $\sim 4000$  nm, respectively. This defocusing step is mainly due to the variation of the surface energy and the occurrence of self-nucleated nanoparticles.

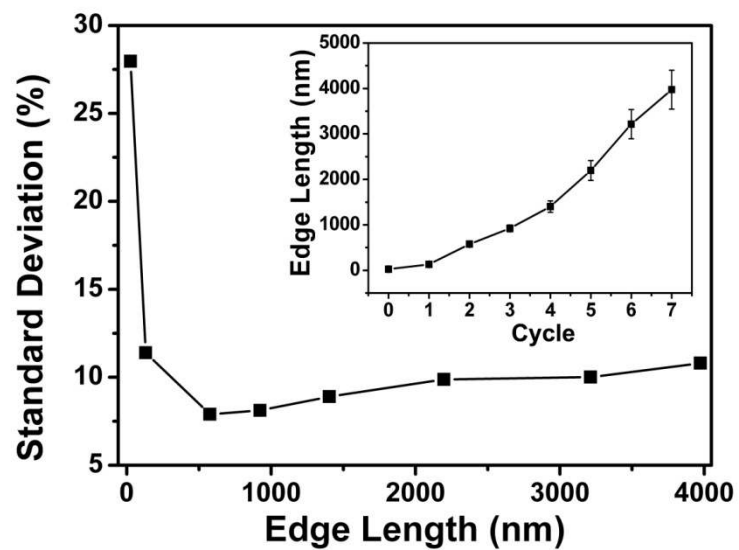


**Figure 2.8** Plots of the standard deviation of the size distribution as a function of the edge length. The inset shows the plots of edge length of Ag nanoplates as a function of the number of cycles of seeded growth. Reproduced with permission from Ref. 44. Copyright © 2010 American Chemical Society.

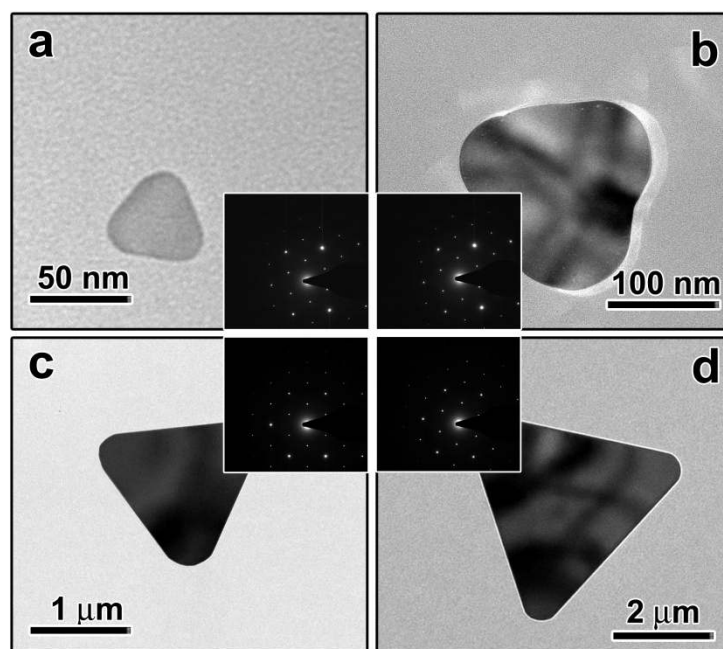


**Figure 2.9** (a-d) TEM images showing the size evolution process of Ag nanoplates. The insets show the corresponding selected area electron diffraction (SAED) patterns obtained by aligning the electron beam perpendicular to the basal surfaces of an individual nanoplate. Reproduced with permission from Ref. 44. Copyright © 2010 American Chemical Society.

Although the size of the particles changes distinctly, the particles still maintain their plate structure during the seeded-growth process. Figures 2.9a-2.9d show representative TEM images of silver nanoplates with different sizes. As shown in the inset of Figure 2.9a, the representative selected area electron diffraction (SAED) pattern indicates that the original Ag nanoplate is a face-centered cubic (*fcc*) crystal. The six bright spots with 6-fold symmetry can be indexed to the  $\{220\}$  reflections of the *fcc* crystal oriented in the  $[111]$  direction, indicating that the flat particle surface is parallel to the  $(111)$  plane. The appearance of strong diffraction spots of  $1/3(422)$  reflections that are normally forbidden for *fcc* Ag lattices indicates the existence of multiple  $(111)$  twin planes parallel to the basal surfaces of the nanoplates.<sup>84</sup> Comparing the ED patterns of isolated nanoparticles before and after seeded growth (Figure 2.9), one can notice clearly that there is no major crystal structure change during the growth process, suggesting a well-maintained single crystal structure.

As we mentioned at the beginning, it has been difficult to obtain silver nanoplates with extremely high aspect ratios because selective capping ligands cannot truly block the surface, especially when the secondary growth rate is fast. With the help of citrate anions, the reduction of silver has been successfully slowed, and hence, the thickness of the as-prepared Ag nanoplates can be maintained.

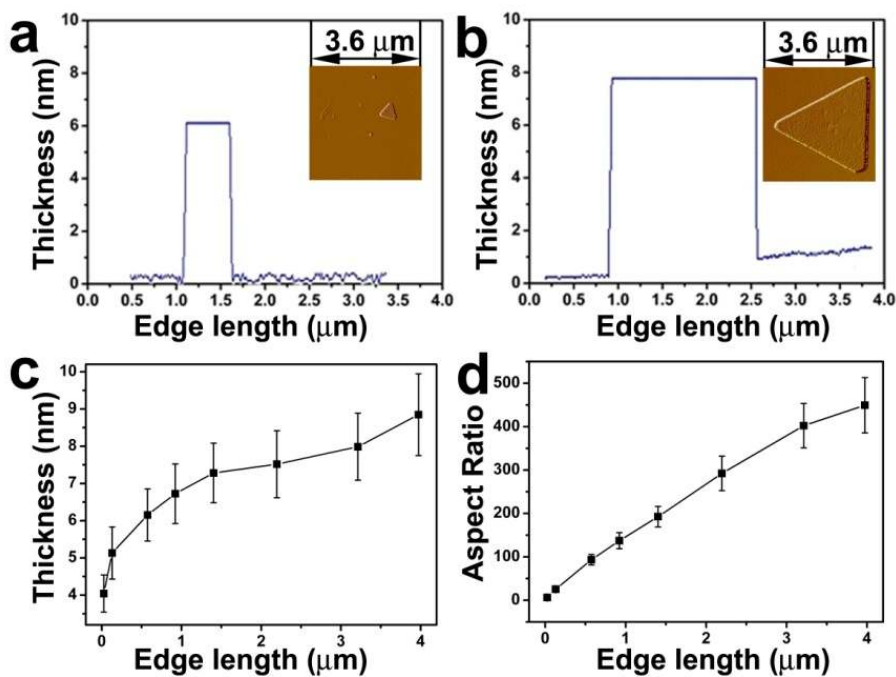


**Figure 2.10** AFM images showing the thickness evolution of representative samples, (a)  $\sim 570$  nm and (b)  $\sim 4$   $\mu\text{m}$ , during the seeded growth process; (c, d): The plots of the change in thickness (c) and aspect ratio (d) as a function of the change in edge length. Reproduced with permission from Ref. 44. Copyright © 2010 American Chemical Society.

As we pointed out previously,<sup>69</sup> the average thickness of the original colloids is about 4 nm, which increases to around 5 nm when the edge length is extended to about 50 nm. AFM measurements were used to monitor the thickness evolution during the growth process. As shown in Figure 2.10a, the thickness of Ag nanoplates becomes  $\sim 6.1$  nm with a mean edge length  $\sim 570$  nm. The thickness profile in the AFM image is very smooth, implying a flat surface. When the edge length of the nanoplates increases up to  $\sim 4$   $\mu\text{m}$ , the average thickness is still less than 10 nm (Figure 2.10b). The change in thickness of such nanoplates with the increasing edge length has been summarized in Figure 2.10c. It is well known that the aspect ratio is very important in determining the optical properties of silver, e.g., surface plasmon resonance (SPR) band. However, due to limitations of controlling both the edge length and thickness over a broad range, it remains a challenge to find a well established model system to study the influence of thickness and aspect ratio. Here, we have shown that by carefully tuning the synthesis parameters, we can precisely control both the thickness and aspect ratio of silver plates, which can be a good model system to study. With the well controlled thickness, extremely high aspect ratio silver nanoplates can be steadily obtained. The original silver nanoplates have an aspect ratio of about 6. With the fast edge length change, the aspect ratio increases almost linearly to over 400 (Figure 2.10d).



The extremely high aspect ratio ensures the widely tunable surface plasmon band of such Ag nanoplates. With the dropwise addition of Ag precursor, the intensity of the SPR band increases gradually. Figure 2.11 shows the normalized UV-vis-NIR spectra of Ag nanoplates in the range of 300-2800 nm during the seeded-growth process. The original silver nanoplates have a strong plasmon band around 630 nm and a weak shoulder around 450 nm, which can be assigned to the in-plane dipole and in-plane quadrupole plasmon resonance of triangular nanoplates, respectively. The relatively broad peak implies the broad size distribution of the Ag nanoplates. During the dropwise addition of Ag precursor, one can clearly notice a gradual red-shift of both the dipole and quadrupole resonances. The narrowing SPR band also suggests the narrower size distribution of the Ag nanoplates. No feature absorbance peak of spherical particles at ~420 nm can be observed, indicating high yield anisotropic growth. The plasmon band of the Ag nanoplates can be precisely tuned within a long range of wavelengths. The spectra over 1300 nm are taken by depositing a Ag layer on a quartz slice to avoid the overlap with the intense stretching vibrational peak of H<sub>2</sub>O. The increased intensity of quadrupole resonance in the range over 1300 nm might come from absorption by the film. Due to the limitations of the instruments and the absorption of the quartz slice, we stopped the measurements at 2800 nm but longer wavelength absorption SPR bands can be steadily obtained with larger aspect ratios.

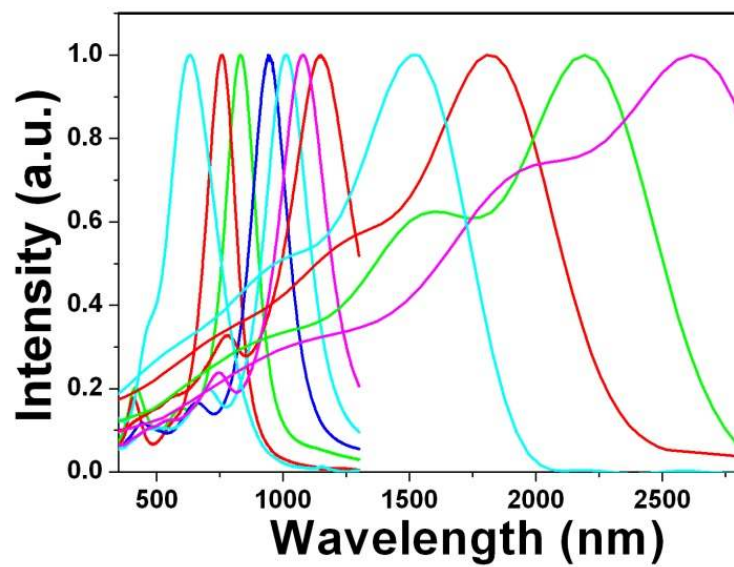


**Figure 2.11** UV-Vis-NIR spectra showing the size evolution process of Ag nanoplates. Reproduced with permission from Ref. 44. Copyright © 2010 American Chemical Society.

## 2.5 Reconstruction of Silver Nanoplates by UV Irradiation

The photo-induced reconstruction of Ag nanoplates involves the preparation of a colloidal suspension of Ag triangular nanoplates first, followed by conversion of the triangular nanoplates to round nanoplate structures using UV light irradiation, as shown in Figure 2.12a. Triangular Ag nanoplates were prepared through a modified thermal process developed by Mirkin et al. Typically, an aqueous solution of silver nitrate, trisodium citrate, PVP, and hydrogen peroxide ( $\text{H}_2\text{O}_2$ ) are mixed and vigorously stirred at room temperature in air. Sodium borohydride ( $\text{NaBH}_4$ ) is rapidly injected into this mixture, generating a pale yellow colloidal solution. After  $\sim 30$  min, the colloid turns to a deep-yellow color, due to the formation of small silver nanoparticles. Within the next several seconds, the morphology continues to change from particles to nanoplates accompanied by the solution color changing from yellow to cyan. Upon stabilization of the solution color, the as-prepared Ag nanoplates are centrifuged and washed with deionized water. Irradiating the aqueous solution using a UV light with a wavelength of 365 nm gradually blue-shifts the plasmon band of the nanoplates, which can be directly confirmed by notable color changes. Under the irradiation, the color of the colloid changes from cyan to blue, purple, red, and finally yellow, suggesting a relatively wide tuning range of the plasmon band. Throughout the process, the solution remains transparent without any aggregation, as shown in the digital photos in Figure 2.12b.

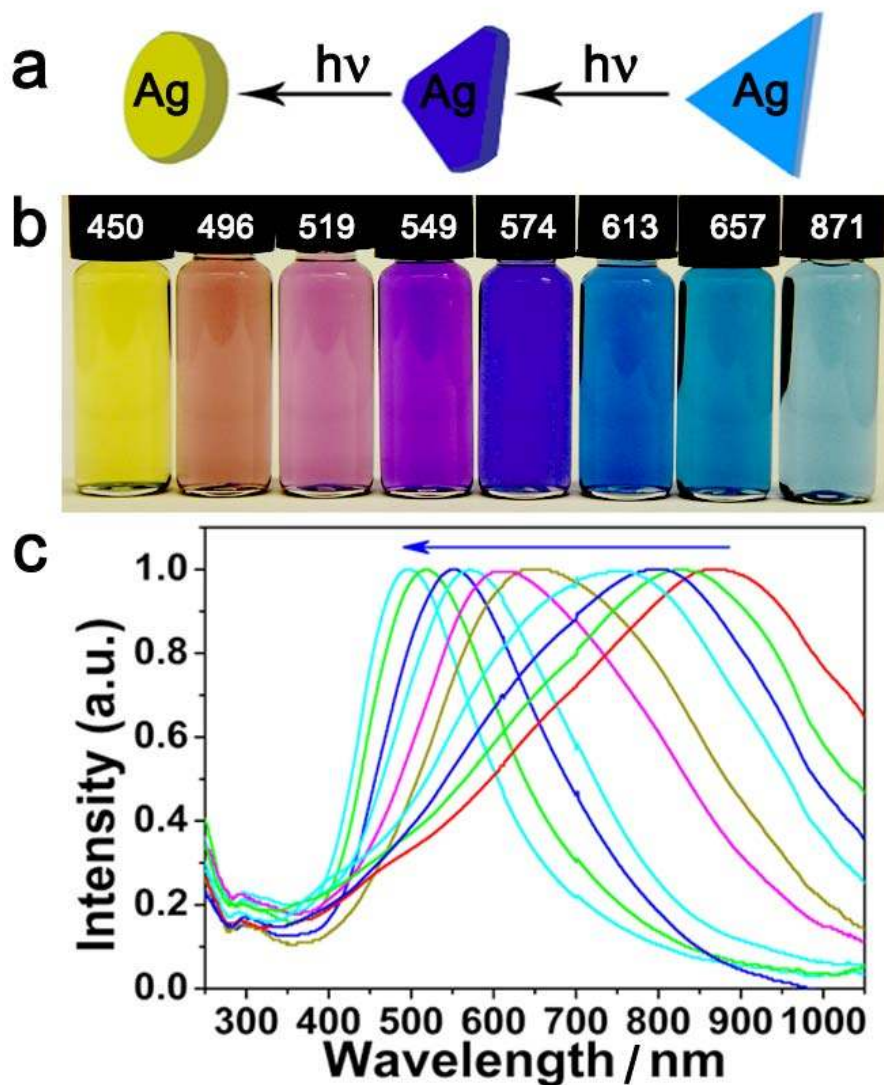


**Figure 2.12** (a) Schematic illustration of the evolution process of Ag nanoplates under UV-light irradiation: the sharp corner of triangular plates disappears, while the thickness of the nanoplates increases. (b, c) Digital photographs and extinction spectra showing the backward tuning of the optical property of the silver nanoplates by irradiation under UV light for different times. From right to left, the samples displayed in the photo were irradiated for 0, 60, 70, 80, 90, 100, 110, and 125 min, while the spectra were taken after irradiating the nanoplate solutions for 0, 20, 40, 60, 70, 80, 90, 100, 110, and 125 min. Reproduced with permission from Ref. 69. Copyright © 2009 WILEY-VCH Verlag GmbH & Co. KGaA, Weinheim.

The irradiation process was also monitored by ultraviolet-visible-near-infrared (UV-Vis-NIR) spectroscopy (Figure 2.12c). For the original cyan colloid solution, plate structure is the major morphology, as evidenced by the diagnostic plasmon bands at 305 nm, 470 nm, and 871 nm, assigned to the out-of-plane quadrupole, in-plane quadrupole, and in-plane dipole plasmon resonance of triangular nanoplates, respectively.<sup>18</sup> During the UV irradiation process, all three plasmon peaks experienced a blue-shift, with the in-plane dipole plasmon shifting fastest from 871 nm to 450 nm. The blue-shift of such as-prepared Ag nanoplates can be precisely tuned by controlling the irradiation time. At the same time, the out-of-plane quadrupole plasmon resonance experienced only a slight change, indicating the particles retained their plate structure without becoming sphere-like structures, while the in-plane quadrupole disappeared due to the overlap by the in-plane dipole resonance.

It is generally accepted that the plasmon band position of silver nanoplates is determined by their tip sharpness and aspect ratio (the ratio between edge length and thickness). Usually, sharp tips, and high aspect ratio lead to a red-shifted resonance, while round tips, and low aspect ratio exert the opposite influences.<sup>13,32</sup> As is evidenced in transmittance electron microscopy (TEM) observations (Figure 2.13), the blue-shift of the major peak of in-plane dipole plasmon resonance appears to result from the morphology change of the Ag nanoplates.

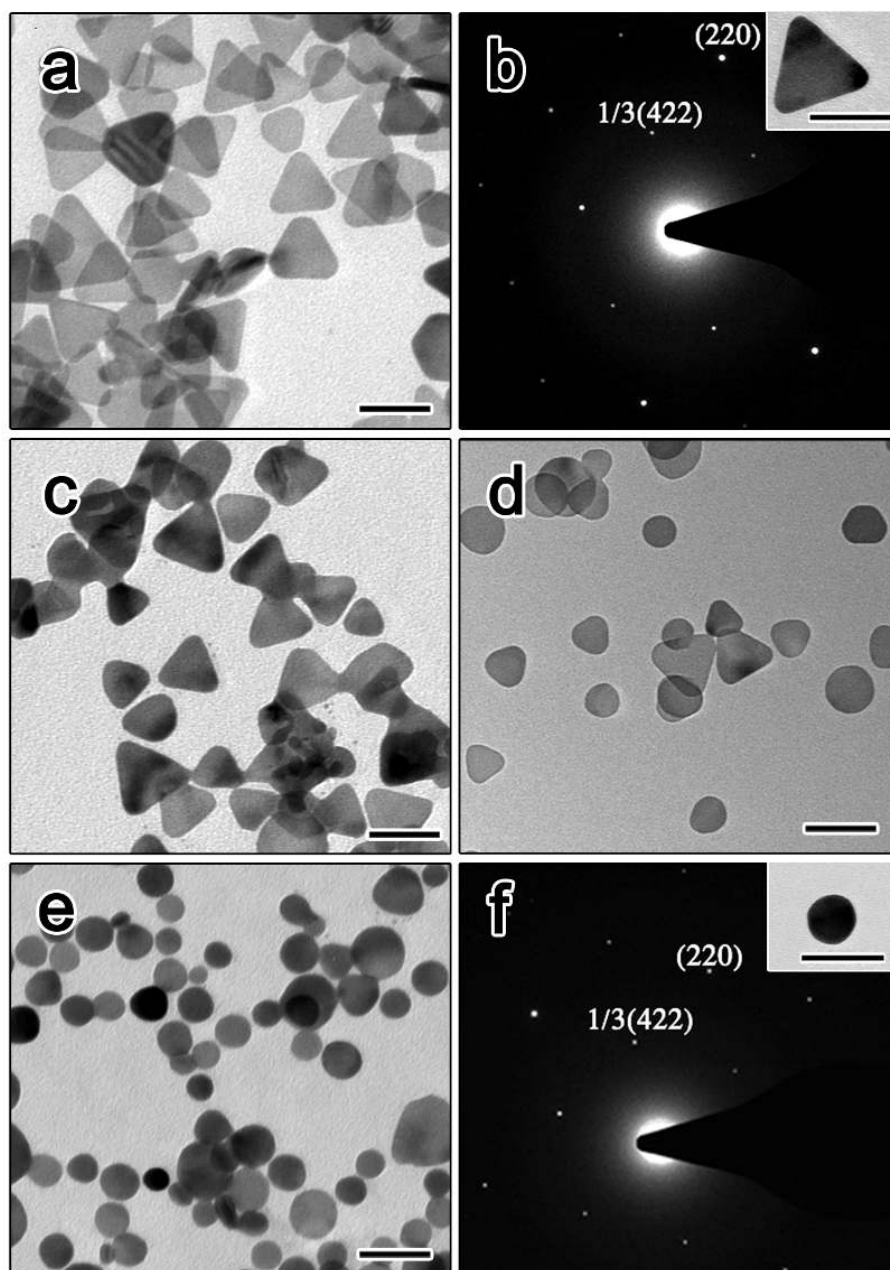


**Figure 2.13** TEM images showing the shape evolution of Ag nanoplates upon UV irradiation for (a) 0 min, (c) 40 min, (d) 80 min, and (e) 125 min. Images of (b) and (f) are selected area electron diffraction patterns taken from a single particle (inset) corresponding to samples of (a) and (e), respectively. Scale bars are 50 nm. Reproduced with permission from Ref. 69. Copyright © 2009 WILEY-VCH Verlag GmbH & Co. KGaA, Weinheim.

Upon irradiation, as shown in Figure 2.13, the sharp tips of the Ag nanoplates with edge length around  $48.52 \pm 6.27$  nm gradually evolve to be truncated, eventually resulting in round nanoplates with edge length of  $26.07 \pm 5.87$  nm. Although the morphology and size of such particles change distinctly, the particles still maintain their plate structure after irradiation. As shown in Figure 2.13b, the representative selected area electron diffraction (SAED) pattern indicates that the original Ag nanoplate is a face-centered cubic (*fcc*) crystal. The six bright spots with 6-fold symmetry can be indexed to the  $\{220\}$  reflections of the *fcc* crystal oriented in the  $[111]$  direction, indicating that the flat particle surface is parallel to the  $(111)$  plane. The forbidden  $1/3\{422\}$  reflections are also observed in the ED pattern, which is consistent with previously reported results.<sup>85</sup> Comparing the ED patterns of isolated nanoparticles before and after irradiation (Figure 2.13b, f), one can notice that there is no major crystal structure change during the shape evolution. In most of the previously reported cases, the change of edge length and tip sharpness of silver nanoplates are said to be responsible for these spectrum shifts.<sup>13,67</sup> However, we can expect only a less than 60 nm shift in the plasmon band for particles with comparable tip morphologies and thicknesses, as opposed to the more than 400 nm shift observed in our experiments.<sup>86</sup> The large shift in the plasmon band, as suggested by Mirkin et al., is induced by the increase in thickness of the plates, which can ultimately cause a sharp change in the aspect ratio.

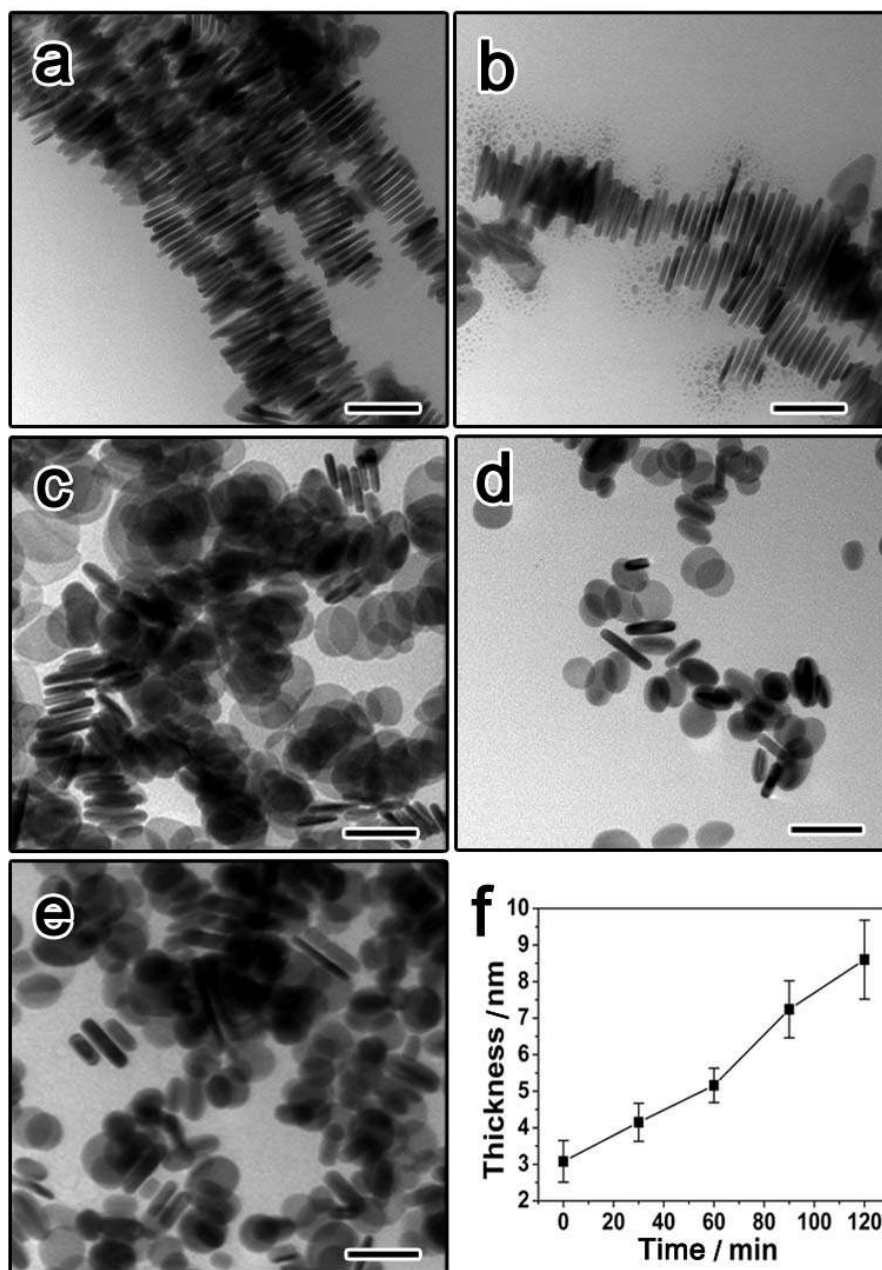


**Figure 2.14** (a-e) TEM images showing the thickness evolution of Ag nanoplates upon UV irradiation for (a) 0 min,  $3.08 \pm 0.57$  nm; (b) 30 min,  $4.15 \pm 0.52$  nm; (c) 60 min,  $5.16 \pm 0.47$  nm; (d) 90 min,  $7.24 \pm 0.78$  nm; (e) 125 min,  $8.6 \pm 1.08$  nm. All scale bars are 50 nm. (f) Summary plot showing the change of nanoplate thickness over irradiation time. Reproduced with permission from Ref. 69. Copyright © 2009 WILEY-VCH Verlag GmbH & Co. KGaA, Weinheim.



As shown in Figure 2.14, we have confirmed the gradual increase of the thickness of such Ag nanoplates as the result of UV irradiation. The average thickness of the original cyan colloids is  $\sim 3.08 \pm 0.57$  nm ( $\lambda_{\text{abs}} = 871$  nm). After 30 min irradiation, the nanoplate thickness increases to  $4.15 \pm 0.52$  nm with the extinction spectrum shifting to 757 nm. Because UV irradiation induces a decrease in diameter and an increase in thickness, the particles are less plate-like and less likely to stack. However, it is still possible to find enough vertically standing plates for thickness estimation. With longer irradiation time, the plate thickness increases to  $5.16 \pm 0.47$  nm ( $\lambda_{\text{abs}} = 657$  nm),  $7.24 \pm 0.78$  nm ( $\lambda_{\text{abs}} = 549$  nm), and  $8.6 \pm 1.08$  nm ( $\lambda_{\text{abs}} = 450$  nm). Figure 2.14f summarizes the changes in the thickness of nanoplates after different periods of UV irradiation. Accordingly, the aspect ratio of the nanoplates can be estimated to be  $\sim 15.75$  for the original cyan colloids and  $\sim 3.03$  for the final yellow colloids.

According to the Gibbs-Thomson effect, the sharp corners are the most energetic areas in a triangular nanoplate.<sup>87,88</sup> Under the irradiation of UV light, these less stable sharp energetic corners will gradually disappear.<sup>89</sup> Although the exact mechanism is still under investigation, we believe the shape transformation likely undergoes a migration process: under the irradiation, the surface atoms in the highly energetic area are forced to “migrate” to other places on the nanoplate to snip the sharp corners and form a more stable structure. They may be dissolved first (due to high energy), and then reduced

back to the two faces of the plates, thus increasing the thickness. This is possible because the UV irradiation of water produces hydrated electrons that are highly reductive.<sup>90</sup> However, it is also possible that these atoms do not dissolve in the solution, and may simply diffuse on the surface and form the final structure. The “migration” of Ag atoms from the corner to the surface is consistent with the fact that the original triangular nanoplates become rounded with reduced size and increased thickness after UV irradiation. More experiments need to be performed to fully understand the mechanism. The results of microscopic analyses and optical measurements, however, allow us to rule out the dissolution-renucleation-regrowth pathway,<sup>67</sup> in which the Ag particles completely dissolve first, followed by the secondary nucleation and growth of particles from these dissociated Ag atoms. No additional small nanoparticles are observed in the TEM during the irradiation process. Also, no representative peak at ~ 400 nm occurs, implying the absence of renucleation-regrowth of such particles.

The stability of nanostructures is critical to many practical applications. For example, plasmon-enhanced spectroscopy requires stable and well-defined resonances. When nonlinear optical enhancements are involved, the signal intensities can be reduced by orders of magnitude, even if a shift of only a few nanometers occurs.<sup>91</sup> Ag nanoplates prepared by direct synthesis often suffers from a gradual blue shift of the spectrum during storage.<sup>21,66,92</sup> The as-prepared precursor nanoplates in our case are not yet stable

because they all contain relatively sharp corners. Four samples with different plasmon band positions were taken as examples and stored at room temperature for 7 days. As Figure 2.15a shows, all of these colloids experienced a ~100 nm blue-shift. Additionally, the extinction spectra broadened during the aging process, implying the non-uniform transformation of the Ag nanoplates, which is not ideal for applications. The plates show significantly improved stability after UV irradiation. Figure 2.15b shows the evolution of the optical properties of seven irradiated samples after storage at room temperature for 7 days, after which only a marginal change happened. More importantly, no broadening of the absorption spectra is observed, implying that the size/thickness and shape of the Ag nanoplates remained the same during storage. We attribute the significantly enhanced stability of the irradiated samples to the pre-removal of highly energetic corners by UV treatment and the surface protection of PVP molecules. The UV treated samples can be stored at room temperature for at least two months without notable change in either color or extinction spectrum. Yu et al. reported previously that the shape evolution can also be prevented by modifying the particle surface with alkanethiols.<sup>66</sup> The use of PVP as the capping ligand, however, has the advantages of retaining the high water dispersity of the particles and avoiding the significant peak broadening due to oxidation of Ag surface by thiol.

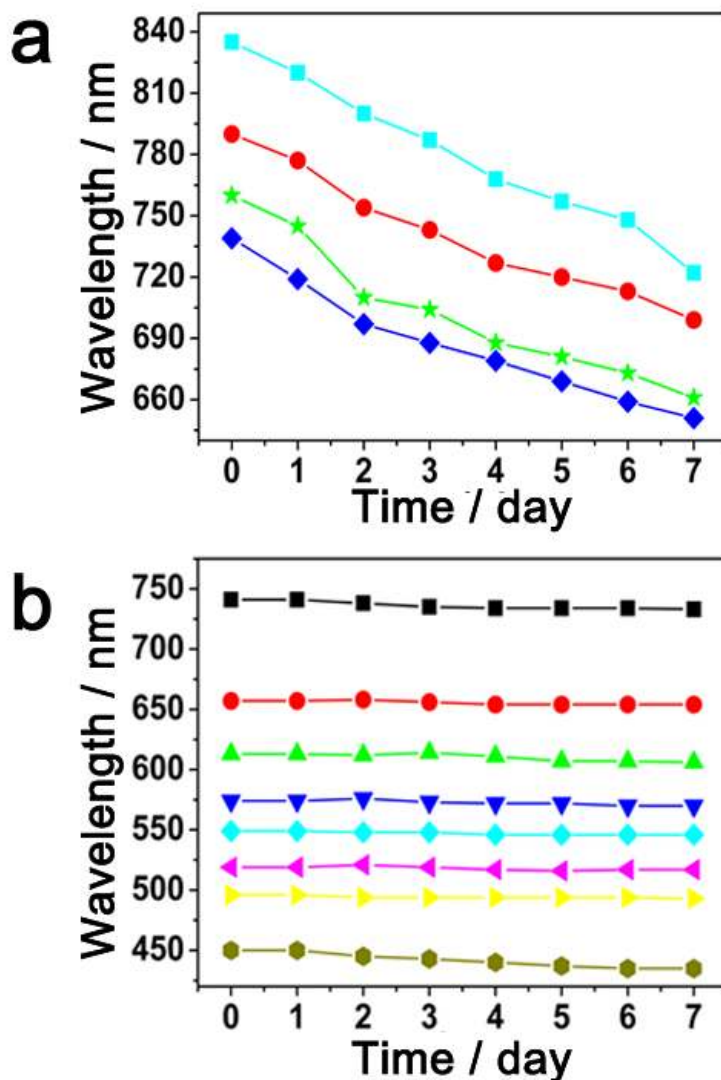


**Figure 2.15** Comparison of the stability in optical property for nanoplates with and without UV irradiation: (a) The plasmon bands of Ag nanoplates without UV treatment blue-shift over time. The synthetic condition was altered to obtain samples with four different plasmon bands. (b) The plasmon bands of the UV-irradiated Ag nanoplates remain stable over time. The samples with different plasmon bands were produced by irradiating the same original plate solution for different periods. Reproduced with permission from Ref. 69. Copyright © 2009 WILEY-VCH Verlag GmbH & Co. KGaA, Weinheim.

## 2.6 Conclusion

In summary, a systematic study on the synthesis, manipulation, and stabilization of silver nanoplates have been executed. First, we have carried out systematic studies and identified the specific roles of each reagent in the direct chemical reduction route to silver nanoplates. Contrary to the previous conclusion that citrate is the crucial component, we instead found that  $\text{H}_2\text{O}_2$  plays an irreplaceable role in determining the shape evolution into plates. As a powerful oxidant,  $\text{H}_2\text{O}_2$  favors the production of silver nanoplates by inducing the formation of planar twinned defects and removing other less stable structures. By harnessing the oxidative power of  $\text{H}_2\text{O}_2$ , various silver sources including metallic silver can now be directly converted to silver nanoplates with the assistance of an appropriate capping ligand, thus significantly enhancing the reproducibility of the nanoplate synthesis. We have also determined that the list of ligands with selective adhesion to Ag (111) facets can be expanded from citrate, which has been previously regarded as a “magic” irreplaceable ligand, to many di- and tri-carboxylate compounds whose two nearest carboxylate groups are separated with two or three carbon atoms. In contrast to traditional practice, we found that a secondary capping ligand is not needed for preparing Ag nanoplates, although its presence may help to improve the size distribution of the product. In particular, the widely used secondary ligand PVP can be replaced by many hydroxyl group-containing compounds, which produce nanoplates of

equal uniformity but superior stability against oxidation and ripening. In addition to the general understanding that  $\text{NaBH}_4$  is a reducing agent, we found it also acts as a capping agent to stabilize the Ag nanoparticles as evidenced by the prolonged initiation time required for nucleation at a higher concentration of  $\text{NaBH}_4$ . By tuning the nucleation kinetics through the concentration of  $\text{NaBH}_4$ , we are able to control the thickness as well as the aspect ratio of silver nanoplates. This work outlines the key components that determine the formation of Ag nanoplates, clarifies the roles of each reagent, provides highly reproducible recipes for synthesis, and therefore represents a significant step towards the complete understanding of the mechanism behind the experimental phenomena.

Second, Ag nanoplates with extremely high aspect ratios (up to over 400) and widely tunable SPR bands have been successfully obtained through a two-step seeded growth process. As the sole surfactant, citrate ligands can effectively block the overgrowth of Ag onto the (111) facets and ensure anisotropic growth along the lateral direction. By slowing down the reaction rate, we have successfully maintained the thin nature of the Ag nanoplates up to sizes of  $\sim 4 \mu\text{m}$ . A size focusing effect has also been observed, which can efficiently produce monodispersed Ag nanoplates with narrow and widely tunable SPR bands. The combination of seeded growth and selective ligand adhesion is

thus practically important. We believe the concept can be well applied to many other materials.

Third, we have demonstrated that the optical properties of Ag nanoplates can be precisely tuned in a wide range through a UV light induced reconstruction process, in which the morphology of the nanoparticles is changed from thin triangular plates to thick round plates. Stabilized with PVP, the as-obtained Ag nanoplates remain stable for long time without any noticeable changes in their optical properties. This unconventional “backward tuning” strategy provides a convenient method for preparing Ag nanoplates with broad tunability in plasmon resonance property, while avoiding the issues of poor reproducibility and stability in the conventional direct synthesis approaches. We believe that the convenient access to Ag nanoplates with tailored optical properties and superior stability will greatly promote their practical applications in areas such as biological and chemical sensing, Raman signal enhancement, and photothermal therapy.

## 2.7 References

- (1) El-Sayed, M. A. *Acc. Chem. Res.* **2001**, *34*, 257.
- (2) Zhang, Q.; Zhang, T. R.; Ge, J. P.; Yin, Y. *Nano Lett.* **2008**, *8*, 2867.
- (3) Sun, Y. G.; Lei, C. H.; Gosztola, D.; Haasch, R. *Langmuir* **2008**, *24*, 11928.
- (4) Nie, S.; Emory, S. R. *Science (Washington, D. C.)* **1997**, *275*, 1102.
- (5) Nicewarner-Pena, S. R.; Freeman, R. G.; Reiss, B. D.; He, L.; Pena, D. J.; Walton, I. D.; Cromer, R.; Keating, C. D.; Natan, M. J. *Science* **2001**, *294*, 137.
- (6) Tao, A. R.; Habas, S.; Yang, P. D. *Small* **2008**, *4*, 310.
- (7) Alivisatos, A. P. *Science* **1996**, *271*, 933.
- (8) Kelly, K. L.; Coronado, E.; Zhao, L. L.; Schatz, G. C. *J. Phys. Chem. B* **2003**, *107*, 668.
- (9) Yin, Y.; Alivisatos, A. P. *Nature* **2005**, *437*, 664.
- (10) Rodriguez-Fernandez, J.; Perez-Juste, J.; Mulvaney, P.; Liz-Marzan, L. M. *J. Phys. Chem. B* **2005**, *109*, 14257.
- (11) Tsung, C. K.; Kou, X. S.; Shi, Q. H.; Zhang, J. P.; Yeung, M. H.; Wang, J. F.; Stucky, G. D. *J. Am. Chem. Soc.* **2006**, *128*, 5352.
- (12) Carbo-Argibay, E.; Rodriguez-Gonzalez, B.; Pacifico, J.; Pastoriza-Santos, I.; Perez-Juste, J.; Liz-Marzan, L. M. *Angew. Chem. Int. Ed.* **2007**, *46*, 8983.
- (13) Pastoriza-Santos, I.; Liz-Marzan, L. M. *J. Mater. Chem.* **2008**, *18*, 1724.
- (14) Im, S. H.; Lee, Y. T.; Wiley, B.; Xia, Y. N. *Angew. Chem. Int. Ed.* **2005**, *44*, 2154.
- (15) Sun, Y. G.; Xia, Y. N. *Science* **2002**, *298*, 2176.
- (16) Tao, A.; Sinsersuksakul, P.; Yang, P. D. *Angew. Chem. Int. Ed.* **2006**, *45*, 4597.
- (17) Haynes, C. L.; Van Duyne, R. P. *J. Phys. Chem. B* **2001**, *105*, 5599.
- (18) Jin, R. C.; Cao, Y. W.; Mirkin, C. A.; Kelly, K. L.; Schatz, G. C.; Zheng, J. G. *Science* **2001**, *294*, 1901.
- (19) Chen, S. H.; Carroll, D. L. *Nano Lett.* **2002**, *2*, 1003.
- (20) Maillard, M.; Huang, P. R.; Brus, L. *Nano Lett.* **2003**, *3*, 1611.



- (21) Ledwith, D. M.; Whelan, A. M.; Kelly, J. M. *J. Mater. Chem.* **2007**, *17*, 2459.
- (22) Xiong, Y.; Washio, I.; Chen, J.; Sadilek, M.; Xia, Y. *Angew. Chem. Int. Ed.* **2007**, *46*, 4917.
- (23) An, J.; Tang, B.; Ning, X. H.; Zhou, J.; Xu, S. P.; Zhao, B.; Xu, W. Q.; Corredor, C.; Lombardi, J. R. *J. Phys. Chem. C* **2007**, *111*, 18055.
- (24) Sun, Y. G.; Gates, B.; Mayers, B.; Xia, Y. N. *Nano Lett.* **2002**, *2*, 165.
- (25) Bastys, V.; Pastoriza-Santos, I.; Rodriguez-Gonzalez, B.; Vaisnoras, R.; Liz-Marzan, L. M. *Adv. Funct. Mater.* **2006**, *16*, 766.
- (26) Pastoriza-Santos, I.; Liz-Marzan, L. M. *J. Mater. Chem.* **2008**, *18*, 1724.
- (27) Millstone, J. E.; Hurst, S. J.; Metraux, G. S.; Cutler, J. I.; Mirkin, C. A. *Small* **2009**, *5*, 646.
- (28) Mayer, K. M.; Hafner, J. H. *Chem Rev* **2011**, *111*, 3828.
- (29) Jones, M. R.; Osberg, K. D.; Macfarlane, R. J.; Langille, M. R.; Mirkin, C. A. *Chem. Rev.* **2011**, *111*, 3736.
- (30) Rycenga, M.; Cogley, C. M.; Zeng, J.; Li, W. Y.; Moran, C. H.; Zhang, Q.; Qin, D.; Xia, Y. N. *Chem. Rev.* **2011**, *111*, 3669.
- (31) Kelly, K. L.; Coronado, E.; Zhao, L. L.; Schatz, G. C. *J. Phys. Chem. B* **2003**, *107*, 668.
- (32) Jin, R. C.; Cao, Y. C.; Hao, E. C.; Metraux, G. S.; Schatz, G. C.; Mirkin, C. A. *Nature* **2003**, *425*, 487.
- (33) Maillard, M.; Huang, P. R.; Brus, L. *Nano Lett.* **2003**, *3*, 1611.
- (34) Xue, C.; Mirkin, C. A. *Angew Chem Int Edit* **2007**, *46*, 2036.
- (35) Sun, Y. G.; Xia, Y. N. *Adv Mater* **2003**, *15*, 695.
- (36) Xue, C.; Metraux, G. S.; Millstone, J. E.; Mirkin, C. A. *J. Am. Chem. Soc.* **2008**, *130*, 8337.
- (37) Zhang, J.; Langille, M. R.; Mirkin, C. A. *J. Am. Chem. Soc.* **2010**, *132*, 12502.
- (38) Chen, S. H.; Carroll, D. L. *Nano Lett.* **2002**, *2*, 1003.
- (39) Sun, Y. G.; Mayers, B.; Xia, Y. N. *Nano Lett.* **2003**, *3*, 675.

- (40) Xiong, Y.; Siekkinen, A. R.; Wang, J.; Yin, Y.; Kim, M. J.; Xia, Y. *J. Mater. Chem.* **2007**, *17*, 2600.
- (41) Sun, Y. G.; Wiederrecht, G. P. *Small* **2007**, *3*, 1964.
- (42) Hao, E. C.; Kelly, K. L.; Hupp, J. T.; Schatz, G. C. *J. Am. Chem. Soc.* **2002**, *124*, 15182.
- (43) Jiang, L. P.; Xu, S.; Zhu, J. M.; Zhang, J. R.; Zhu, J. J.; Chen, H. Y. *Inorg. Chem.* **2004**, *43*, 5877.
- (44) Zhang, Q.; Hu, Y.; Guo, S.; Goebel, J.; Yin, Y. *Nano Lett.* **2010**, *10*, 5037.
- (45) Jiang, X. C.; Chen, C. Y.; Chen, W. M.; Yu, A. B. *Langmuir* **2010**, *26*, 4400.
- (46) Zeng, J.; Tao, J.; Li, W.; Grant, J.; Zhu, Y.; Xia, Y. *Chem. Asian J.* **2011**, *6*, 376.
- (47) Zeng, J.; Xia, X.; Rycenga, M.; Henneghan, P.; Li, Q.; Xia, Y. *Angew Chem Int Edit* **2011**, *50*, 244.
- (48) Frank, A. J.; Cathcart, N.; Maly, K. E.; Kitaev, V. *J. Chem. Educ.* **2010**, *87*, 1098.
- (49) Li, N.; Zhang, Q.; Quinlivan, S.; Goebel, J.; Gan, Y.; Yin, Y. *ChemPhysChem* **2012**, DOI: 10.1002/cphc.201101018.
- (50) Peng, X. G.; Manna, L.; Yang, W. D.; Wickham, J.; Scher, E.; Kadavanich, A.; Alivisatos, A. P. *Nature* **2000**, *404*, 59.
- (51) Puentes, V. F.; Krishnan, K. M.; Alivisatos, A. P. *Science* **2001**, *291*, 2115.
- (52) Puentes, V. F.; Zanchet, D.; Erdonmez, C. K.; Alivisatos, A. P. *J. Am. Chem. Soc.* **2002**, *124*, 12874.
- (53) Sun, Y. G.; Mayers, B.; Herricks, T.; Xia, Y. N. *Nano Lett.* **2003**, *3*, 955.
- (54) Xia, Y.; Yang, P.; Sun, Y.; Wu, Y.; Mayers, B.; Gates, B.; Yin, Y.; Kim, F.; Yan, Y. *Adv. Mater.* **2003**, *15*, 353.
- (55) Millstone, J. E.; Park, S.; Shuford, K. L.; Qin, L. D.; Schatz, G. C.; Mirkin, C. A. *J. Am. Chem. Soc.* **2005**, *127*, 5312.
- (56) Xiong, Y.; Washio, I.; Chen, J.; Sadilek, M.; Xia, Y. *Angew. Chem. Int. Ed.* **2007**, *46*, 4917.
- (57) Xia, Y.; Xiong, Y. J.; Lim, B.; Skrabalak, S. E. *Angew. Chem. Int. Ed.* **2009**, *48*, 60.
- (58) Colvin, V. L.; Schlamp, M. C.; Alivisatos, A. P. *Nature* **1994**, *370*, 354.

- (59) Peng, X. G.; Wickham, J.; Alivisatos, A. P. *J. Am. Chem. Soc.* **1998**, *120*, 5343.
- (60) Jana, N. R.; Gearheart, L.; Murphy, C. J. *Chem. Commun.* **2001**, 617.
- (61) Murphy, C. J.; Jana, N. R. *Adv. Mater.* **2002**, *14*, 80.
- (62) Millstone, J. E.; Metraux, G. S.; Mirkin, C. A. *Adv. Funct. Mater.* **2006**, *16*, 1209.
- (63) Habas, S. E.; Lee, H.; Radmilovic, V.; Somorjai, G. A.; Yang, P. *Nat. Mater.* **2007**, *6*, 692.
- (64) Fan, F. R.; Liu, D. Y.; Wu, Y. F.; Duan, S.; Xie, Z. X.; Jiang, Z. Y.; Tian, Z. Q. *J. Am. Chem. Soc.* **2008**, *130*, 6949.
- (65) Seo, D.; Il Yoo, C.; Jung, J.; Song, H. *J. Am. Chem. Soc.* **2008**, *130*, 2940.
- (66) Jiang, X. C.; Zeng, Q. H.; Yu, A. B. *Langmuir* **2007**, *23*, 2218.
- (67) Tang, B.; An, J.; Zheng, X. L.; Xu, S. P.; Li, D. M.; Zhou, J.; Zhao, B.; Xu, W. Q. *J. Phys. Chem. C* **2008**, *112*, 18361.
- (68) Zhang, Q.; Li, N.; Goebel, J.; Lu, Z. D.; Yin, Y. D. *J Am Chem Soc* **2011**, *133*, 18931.
- (69) Zhang, Q.; Ge, J.; Pham, T.; Goebel, J.; Hu, Y.; Lu, Z.; Yin, Y. *Angew Chem Int Edit* **2009**, *48*, 3516.
- (70) Metraux, G. S.; Mirkin, C. A. *Adv Mater* **2005**, *17*, 412.
- (71) Henglein, A. *Chem. Phys. Lett.* **1989**, *154*, 473.
- (72) Belloni, J.; Mostafavi, M.; Remita, H.; Marignier, J. L.; Delcourt, M. O. *New J. Chem.* **1998**, *22*, 1239.
- (73) Van Hyning, D. L.; Zukoski, C. F. *Langmuir* **1998**, *14*, 7034.
- (74) Mulvihill, M. J.; Ling, X. Y.; Henzie, J.; Yang, P. D. *J. Am. Chem. Soc.* **2010**, *132*, 268.
- (75) Hoare, J. P. *Standard Potentials in Aqueous Solution*; Marcel Dekker: New York, 1985.
- (76) Ho, C. M.; Yau, S. K.; Lok, C. N.; So, M. H.; Che, C. M. *Chem. Asian J.* **2010**, *5*, 285.
- (77) Ledwith, D. M.; Whelan, A. M.; Kelly, J. M. *J. Mater. Chem.* **2007**, *17*, 2459.
- (78) Mpourmpakis, G.; Vlachos, D. G. *Langmuir* **2008**, *24*, 7465.
- (79) Kilin, D. S.; Prezhdo, O. V.; Xia, Y. *Chem. Phys. Lett.* **2008**, *458*, 113.

- (80) Solomon, S. D.; Bahadory, M.; Jeyarajasingam, A. V.; Rutkowsky, S. A.; Boritz, C.; Mulfinger, L. *J. Chem. Educ.* **2007**, *84*, 322.
- (81) Mullin, J. W. *Crystallization*; 1st ed.; Butterworth & Co Ltd: London, 1972.
- (82) Djokic, S. *Bioinorg. Chem. Appl.* **2008**, 436458.
- (83) Metraux, G. S.; Mirkin, C. A. *Adv. Mater. (Weinheim, Ger.)* **2005**, *17*, 412.
- (84) Sun, Y. G.; Ren, Y.; Haeffner, D. R.; Almer, J. D.; Wang, L.; Yang, W.; Truong, T. T. *Nano Lett.* **2010**, *10*, 3747.
- (85) Rocha, T. C. R.; Zanchet, D. *J. Phys. Chem. C* **2007**, *111*, 6989.
- (86) Metraux, G. S.; Mirkin, C. A. *Adv. Mater.* **2005**, *17*, 412.
- (87) Chen, S. H.; Fan, Z. Y.; Carroll, D. L. *J. Phys. Chem. B* **2002**, *106*, 10777.
- (88) Millstone, J. E.; Metraux, G. S.; Mirkin, C. A. *Adv. Funct. Mater.* **2006**, *16*, 1209.
- (89) An, J.; Tang, B.; Zheng, X. L.; Zhou, J.; Dong, F. X.; Xu, S. P.; Wang, Y.; Zhao, B.; Xu, W. Q. *J. Phys. Chem. C* **2008**, *112*, 15176.
- (90) Hart, E. J. *Science* **1964**, *146*, 19.
- (91) Genov, D. A.; Sarychev, A. K.; Shalaev, V. M.; Wei, A. *Nano Lett.* **2004**, *4*, 153.
- (92) Xiong, Y. J.; Siekkinen, A. R.; Wang, J. G.; Yin, Y.; Kim, M. J.; Xia, Y. N. *J. Mater. Chem.* **2007**, *17*, 2600.

## Chapter 3

# Surface-Protected Etching of Mesoporous Oxide Shells for the Stabilization of Noble Metal Nanocatalysts

### 3.1 Introduction

Methods for the stabilization of nanocatalysts can be roughly divided into two categories: physical and chemical. The physical approach is more straightforward: nanoparticles are separated from each other by a physical barrier so that they cannot contact each other directly. Colloidal nanoparticles dispersed in solution are usually stabilized by electrostatic forces or steric stabilizers such as surfactants, ligands, or dendrimers.<sup>1-11</sup> However, in many cases inter-particle forces and ligand binding can be easily perturbed during catalytic processes, thus leading to coagulation and the loss of the high activity associated with the state of colloidal dispersion.<sup>12</sup> Other organic functional polymers have also been used to stabilize metal nanoparticles in aqueous reaction systems. The polymer support can be a soluble linear or branched macromolecule or a micellar aggregate which wraps the metal nanoparticles in solution, thus preventing metal sintering and precipitation.<sup>13</sup> However, because of their poor thermal stability, organic polymers cannot be used when a catalytic reaction is performed at elevated temperatures or in highly oxidizing environments.

Ordered mesoporous oxides, typically  $\text{SiO}_2$ , prepared by surfactant-induced self-assembly have been regarded as ideal supports for heterogeneous catalysts. They offer high surface areas and tunable pore sizes,<sup>14-17</sup> and metal nanoparticles can be introduced into their mesopores by either *in situ* encapsulation during the growth of mesoporous silica such as SBA-15 or by sonication-aided impregnation in the presence of pre-formed mesoporous materials.<sup>18-24</sup> Nevertheless, it is still quite difficult to achieve uniform impregnation with reasonably high loadings, and also to minimize the mass transfer resistance that may be encountered in some cases, particularly with porous structures having extended channel lengths. Moreover, although significantly enhanced thermal stability has been demonstrated,<sup>21</sup> secondary particle growth can also occur under reaction conditions because nanoparticles can still migrate within the channels of the support unless they have a size equal to the diameter of the pores.<sup>25</sup> Nanoparticle ripening is another problem that can lead to dramatic reduction of specific surface area and to severely decreased catalytic activity and selectivity.<sup>14-17,25-30</sup>

Chemical approaches such as those that rely on substrate effects or on the formation of alloy or hybrid materials have also been widely studied as a means to stabilize metal nanocatalysts. Metallic nanoparticles can be immobilized on inorganic solid supports to provide the classic advantages of heterogeneous catalysis: enhanced stability of catalysts during reaction and convenient recycling by simple procedures like filtration, magnetic

separation or centrifugation.<sup>31</sup> The most widely used materials as supports in catalysis are inorganic solids with high surface areas, such as charcoal, salt, and oxides including SiO<sub>2</sub>, Al<sub>2</sub>O<sub>3</sub> and TiO<sub>2</sub>.<sup>32-36</sup> Recently, multiple-oxide supports have been utilized to obtain stable metallic nanocatalysts, by exploring synergetic effects among the different components.<sup>37</sup> For instance, by coating a thin alumina layer on anatase TiO<sub>2</sub> and subsequently depositing Au on the Al<sub>2</sub>O<sub>3</sub>/TiO<sub>2</sub> dual oxide, the Dai group has successfully produced a highly stable catalyst which retains high activity for CO oxidation even after calcination at 773 K.<sup>29,30</sup>

The stability of metal nanoparticles can also be significantly enhanced by forming alloy or hybrid materials. For example, Pt nanocatalysts are usually utilized as electro-catalysts in proton-exchange-membrane fuel cells (PEMFCs). However, the stability and durability of the Pt nanocatalysts are among the most challenging issues that must be solved in order to make PEMFCs a reality.<sup>38-42</sup> To stabilize such metal nanoparticles, some transition metals such as Ni and Co have been alloyed with Pt in order to suppress the growth of Pt nanoparticles.<sup>43-48</sup> Unfortunately, most of the additives tried so far have shown to also suffer from chemical instability during the reaction. They can, for instance, be dissolved and diffuse into the membrane of PEMFCs, a process that results in some unexpected problems and deteriorates the performance of the PEMFCs.<sup>41,49</sup>

Traditionally, the term “nanoreactor” mainly refers to systems that can provide small spaces for the controlled synthesis of new nanomaterials, thus including various nanostructures such as micelles<sup>50</sup> or reverse micelles,<sup>51</sup> liquid crystals,<sup>52</sup> microemulsions,<sup>53,54</sup> microgels,<sup>55</sup> amphiphilic polymers or block copolymers,<sup>56,57</sup> liposomes,<sup>58-60</sup> and dendrimers.<sup>9,11,61,62</sup> A wide range of nanomaterials such as metals and semiconductors with interesting physical properties have been produced this way. Recently, the concept of nanoreactors has become more widely adopted to describe systems with nanoscale spaces where catalytic reactions can occur. In particular, it has been realized that metallic nanoparticles can be significantly stabilized against coalescence by encapsulating them within inorganic layers.<sup>63-69</sup> However, dense inorganic coatings make it difficult for reactant molecules to reach buried active materials, limiting the practical use of such systems in catalysis. Several procedures, including layer-by-layer deposition techniques and sacrificial templating approaches, have been reported to encapsulate metal nanoparticles in hollow shells of inorganic materials, including oxides and carbon.<sup>67,70-75</sup> These as-obtained “yolk-shell” type nanostructures can stabilize metal nanoparticles even under harsh reaction conditions.<sup>73,76</sup> Schüth et al., for example, have prepared hollow zirconia (ZrO<sub>2</sub>) shells that each containing one Au nanoparticle by using a templating method, and demonstrated the excellent stability of the resulting material against sintering at high reaction temperatures.<sup>67</sup> The control of



the porosity of the shells is, however, still a challenge in such multi-step procedures. Many conventional procedures rely heavily on the use of molecular templates or porogens through the self-assembly process to produce porous structures. In those cases, tuning the pore size is mainly achieved by employing different porogens, many of which are relatively expensive and currently only available in small quantities. Also, the chemistry for coating individual nanoparticles with mesoporous shells must be developed separately for each porogen, making continuous tuning of the pore size inconvenient. The defect-rejecting nature of self-assembly processes makes encapsulation of metal nanoparticles into porous shells additionally complicated. In the very few reports where a successful porous coating has been realized on solid cores, the orientation of the pore channels was typically found to be parallel to the core surface, possibly making materials transfer through the channel to the catalyst core fairly limited.<sup>77,78</sup>

In view of these difficulties, it may be worthwhile to develop a facile synthetic approach to fabricating “nanoreactors” composed of nanocatalysts within porous shells. The procedures involved must be simple, scalable, cost-effective, and compatible with nanocatalysts with a wide range of compositions, sizes and shapes. In this regard, Alivisatos and co-workers have already advanced a process based on the Kirkendall effect for producing nanoreactor systems.<sup>79</sup> Pt@CoO yolk/shell structures formed upon oxidation of Pt@Co core/shell particles, with the hollow CoO shells generated by the

outward diffusion of Co, were produced. The Pt cores within the Pt@CoO particles were shown capable of catalyzing the hydrogenation of ethylene, and the surrounding polycrystalline CoO shells were proven to allow the transport of gas-phase reactants and products.<sup>80</sup> As a one-pot synthesis without the need for additional sacrificial materials, the Kirkendall effect-based process is promising for many gas- and solution-phase reactions. However, it is desirable to substitute the CoO shell with more commonly-used oxide supports such as SiO<sub>2</sub> and TiO<sub>2</sub>. Song and co-workers have fabricated a Au@SiO<sub>2</sub> yolk-shell structure through selective etching of metal cores from Au@SiO<sub>2</sub> core-shell particles.<sup>76</sup> Unfortunately, although this method allows for the altering of the size of the metal cores, there is a lack of control of the shape of such metal cores and the porosity of the shells. In their continuing work, an organosilane was introduced into the SiO<sub>2</sub> shells to create mesopores upon calcination.<sup>81</sup> In this case, the pore volume could be increased by adding more organosilane, but it was still difficult to systematically tune the pore size. Asefa and co-workers have sandwiched gold nanoparticles between a SiO<sub>2</sub> core and a SiO<sub>2</sub> shell and used KCN to etch both the metal particles and the oxide shell.<sup>82</sup> Access to the metal particles could be improved to some extent by thinning the SiO<sub>2</sub> shell, but this etching process was also proven difficult to control, because KCN etches gold nanoparticles quickly. In addition, the high toxicity of KCN is a concern for widespread industrial uses. Somorjai and co-workers have also

demonstrated a process that uses embedded surfactants to create random mesoporous structures in the SiO<sub>2</sub> shells of Pt@SiO<sub>2</sub> core-shell particles, but, again, the control over the pore size has not been fully demonstrated.<sup>83</sup> Recently, we have proposed the fabrication of metal@oxide nanoreactors by using a group of novel, etching-based strategies to controllably produce mesopores in the oxide shells.<sup>75,84-89</sup> During the etching process, the pore size can be systematically controlled while maintaining the metal catalyst particles and the overall size of the oxide shells unchanged.

In this Chapter, we will focus on the stabilization of metallic nanocatalysts using porous oxide shells for catalytic applications in both the liquid and gas phases. First, in **Section 3.3**, we introduce a general strategy, called the “surface-protected etching” process, as the major synthetic tool for producing mesoporous shells for the stabilization of noble metal nanocatalysts. Its feasibility and flexibility in controlling the pore size and architecture of the oxide shell will be illustrated. **Section 3.4** will introduce a sandwich-like structure prepared based on the “surface-protected etching” process. Multi-functional materials could be incorporated to make recyclable and highly efficient catalysts. The as-prepared sandwich structure could be further used in gas phase reaction, which shows improved stability against high temperature sintering, as depicted in **Section 3.5**. Finally, we conclude with a short summary in **Section 3.6**.

### 3.2 Materials and Methods

**Materials** Tetraethylorthosilicate (TEOS), poly(vinyl pyrrolidone) (PVP,  $M_w \sim 10,000$ ), sodium hydroxide (NaOH),  $\text{HAuCl}_4$ , sodium citrate, and ammonium hydroxide ( $\text{NH}_3 \cdot \text{H}_2\text{O}$ , 28% by weight in water) were purchased from Sigma-Aldrich. Ethanol and isopropanol were of analytical grade and obtained from Fisher. All chemicals were directly used as received without further purification.

**Synthesis of  $\text{SiO}_2$  solid spheres** In a typical synthesis, 1 mL TEOS was injected into a mixture of 4 mL of deionized  $\text{H}_2\text{O}$ , 1 mL of  $\text{NH}_3 \cdot \text{H}_2\text{O}$  and 20 mL 2-propanol at room temperature under magnetic stirring. After reacting for 2 hours, the colloidal spheres were collected by centrifugation, re-dispersed in 30 mL deionized water. The particle size could be simply tuned by changing the concentration of ammonium hydroxide.

**Synthesis of  $\text{Au}@\text{SiO}_2$  core-shell structures** A gold sol (30 mL) is prepared according to the standard sodium citrate reduction method. Briefly, a solution of hydrogen tetrachloroaurate trihydrate was prepared in water and heated to reflux with magnetic stirring, followed immediately by addition of 1 mL of 3 wt% freshly prepared trisodium citrate-water solution, which initiated the reduction of the hydrogen tetrachloroaurate trihydrate. The aurate-citrate solution was allowed to reflux for approximately 30 min. or until completion of the redox reaction as indicated by a change in solution color from faint

yellow to dark red. This method produces a stable, deep-red dispersion of gold particles with an average diameter of around 15 nm and 10% polydispersity. An aqueous solution of PVP (0.235 mL, 12.8 mg/mL) was added to the sol. The mixture was allowed to stand at room temperature for 24 hours under magnetic stirring, allowing PVP molecules to attach to Au nanoparticles, which were then separated from solution by centrifuging at 11,000 rpm for 45 min and re-dispersed in 92 mL ethanol. The as-prepared solution was then mixed with 13.2 mL of deionized H<sub>2</sub>O and 2.48 mL of NH<sub>3</sub>•H<sub>2</sub>O. TEOS (3.45 mL) was injected into the mixture at room temperature under stirring. After reacting for 4 hours, the spheres were collected by centrifugation, and finally re-dispersed in 24 mL of deionized water.

***Etching SiO<sub>2</sub> spheres*** PVP K15 (M<sub>w</sub> ~ 10,000) was added to the as-prepared solid SiO<sub>2</sub> solution (molar ratio of PVP/SiO<sub>2</sub> is 10). The mixture was heated up to 100°C for 3 hours to load PVP, and then cooled to room temperature. Under magnetic stirring, 1 mL of 0.1 g/mL sodium hydroxide (NaOH) dissolved in water was added to 4 mL of the as-prepared solution at room temperature. As more material is etched away from the silica particles, the solution becomes less and less opaque. Therefore, we were able to monitor the progress of the etching process by measuring transmission through the solution using UV-Vis spectrometry. The solution was cleaned with repeated actions of water dilution and centrifugation. The colloidal spheres were finally dispersed in polar

solvents such as deionized water or ethanol. Au@SiO<sub>2</sub> core-shell particles can be etched using a similar procedure.

***Synthesis of Fe<sub>3</sub>O<sub>4</sub>/SiO<sub>2</sub>/Au/m-SiO<sub>2</sub> Structures*** Fe<sub>3</sub>O<sub>4</sub> superparamagnetic cores with a typical diameter of 140 nm was synthesized using a high-temperature hydrolysis reaction reported previously [Ge et al., *Angew. Chem. Int. Ed.* 2007, 46, 4342]. Fe<sub>3</sub>O<sub>4</sub>/SiO<sub>2</sub> core-shell colloids were prepared through a modified Stöber process. Typically, an aqueous solution (3 mL) containing Fe<sub>3</sub>O<sub>4</sub> CNCs (~25 mg) was mixed with ethyl alcohol (20 mL), aqueous ammonia (28%, 1 mL) under vigorous magnetic stirring. Tetraethylorthosilicate (TEOS, 0.1 mL) was injected into the solution every 20 min until the total amount of TEOS reaches 0.5 mL. After washing with ethanol through centrifugation and redispersion two times, the particles were transferred into a mixture of isopropanol (20 mL) and 3-aminopropyl- triethoxysilane (APTS, 50 µL) and heated up to 80°C for 2 hours to functionalize the silica surface with amino groups. The -NH<sub>2</sub> terminated Fe<sub>3</sub>O<sub>4</sub>/SiO<sub>2</sub> colloids were washed with isopropanol and dispersed back in D.I. water (3 mL). In a separate reaction, Au nanoparticles were synthesized using the Turkevich method [Turkevich et al., *Discuss. Faraday Soc.* 1951, 11, 55]. Then, citrate stabilized Au nanoparticles (~15 nm) were adsorbed onto the -NH<sub>2</sub> functionalized Fe<sub>3</sub>O<sub>4</sub>/SiO<sub>2</sub> colloids by adding the above colloids (1.5 mL) to the Au sols (150 mL with Au concentration of  $4.8 \times 10^{-4}$  M) under sonication [Pastoriza-Santos et al., *Phys. Chem.*

Chem. Phys., 2004. 6, 5056]. The solution was allowed to equilibrate for 5min. The  $\text{Fe}_3\text{O}_4/\text{SiO}_2/\text{Au}$  colloids were centrifuged and dispersed in de-ionized water (40 mL). The second  $\text{SiO}_2$  layer was prepared using a method developed by Graf et al. [Graf et al., Langmuir, 2003, 19, 6693] The  $\text{Fe}_3\text{O}_4/\text{SiO}_2/\text{Au}$  solution (40 mL) was mixed with a PVP solution (25 mL, Mw ~55000) with a concentration of 0.02 g / mL under sonication. The mixture was further sonicated for 5min to allow adequate polymer to adsorb to the particle surface. These colloids were subsequently centrifuged to remove the unbound polymer and then dispersed in a mixture of ethanol (100 mL), water (12.5 mL), aqueous ammonia (5 mL) and 0.6 mL TEOS for the growth of silica shell wrapping the Au particles. Finally, the product colloids were washed by ethanol and dispersed in water (20 mL) PVP K15 (1 g) was dissolved in  $\text{Fe}_3\text{O}_4/\text{SiO}_2/\text{Au}/\text{SiO}_2$  solution (20 mL) by mechanical stirring. Refluxed at 100°C for 3 hours, the solution was cooled down to room temperature naturally. NaOH solution (5 mL with concentration of 0.16 g / mL) was injected into the system to start the etching, which can be monitored by the optical transmission spectrum. The original reaction solution (0.1 mL) was diluted with DI water (1 mL) for transmittance measurements. After washing with DI water several times, the particles were finally dispersed in water (25 mL, same concentration as reaction solution) and prepared for catalysis.

***Catalytic reduction of 4-nitrophenol*** The reduction of 4-NP by NaBH<sub>4</sub> was chosen as a model reaction to test the catalytic activity and stability of the Au@SiO<sub>2</sub> nanocatalysts. Aqueous solutions of 4-NP (0.03 mL, 0.01M) and NaBH<sub>4</sub> (0.20 mL, 0.1M) were added to deionized water (2.5 mL) in a quartz cuvette under magnetic stirring. After adding Au catalyst particles, the bright yellow solution gradually faded as the reaction proceeded. UV-Vis spectra were recorded at regular interval to monitor the progress of the reaction.

***Gas phase catalytic test*** The catalytic activity for the gas-phase reactions was tested in a batch reactor consisting of stainless-steel of approximately 150 cm<sup>3</sup> total volume evacuated with a mechanical pump to a base pressure of about  $5 \times 10^{-2}$  Torr.<sup>90-92</sup> 5 mg of the catalyst was sandwiched in between two quartz wool plugs and placed in one of the vertical arms of a U-shaped quartz tube cell (10 mm inner diameter), which could be heated in a furnace (Omega) to a temperature controlled by an electronic controller (Omron). After drying at 150 °C, the catalyst was activated by three oxidation-reduction cycles at 350 °C and cooled down to 100 °C; and the reactant gases added to the reactor loop, to a final pressure of 600 Torr (10 Torr 2-butene, 5 Torr hydrogen, 585 Torr Ar) and mixed using a circulation pump. Aliquots of the gas were taken periodically, every 20 min, using an 8-port valve with 10 mL sampling volumes, starting after 2 min from the beginning of the reaction, and analyzed by gas chromatography using a Varian 3700 instrument equipped with a flame ionization



detector (FID) and a 23% SP-1700 on 80/100 Chromosorb PAW column (SUPELCO).

Nitrogen (98% purity) was used as the carrier gas.

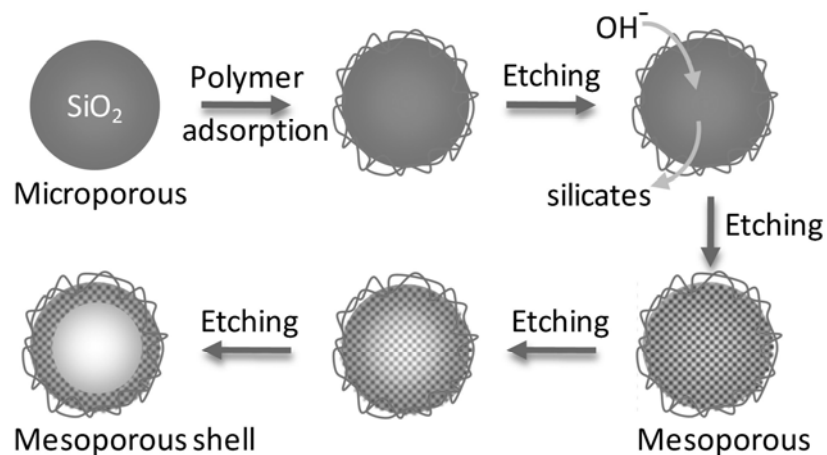
**Characterization** Morphology of the products was characterized by using a Tecnai T12 transmission electron microscope (TEM). The hollow spheres dispersed in water were cast onto a carbon-coated copper grid, followed by evaporation under vacuum at room temperature. Fourier transform infrared (FT-IR) spectra were collected with a Bruker Equinox 55 spectrophotometer scanning from 400-4000  $\text{cm}^{-1}$  with a resolution of 4  $\text{cm}^{-1}$  for 64 scans. Measurements were performed with pressed pellets, which were made by using KBr powder as diluents. Thermo-gravimetric analyses (TGA) were carried out on a Mettler Toledo TGA/SDTA 851e under  $\text{N}_2$  atmosphere in the temperature range of 40-700°C at a rate of 10°C/min. A probe-type Ocean Optics HR2000CG-UV-NIR spectrometer was used to measure the UV-Vis spectra of the solution to monitor the real-time variation of concentration of 4-NP. The integration time was set to be 3 msec. Nitrogen adsorption-desorption measurements were carried out on a Micromeritics ASAP 2010 instrument to determine the BET surface area, single point total pore volume, and BJH pore size distribution.

### **3.3 Permeable Silica Shell through Surface-Protected Etching**

Essentially, template-based approaches for the synthesis of hollow structures utilize the difference in stability between the core and shell materials against post-treatments such as etching and calcination, in which the interior part is unstable and disappears while the outer layer remains. It thus stands to reason that hollow structures can be synthesized by enhancing the relative stability of the surface layer of a single-component nanostructure to make it more stable than the interior. Before the introduction of such a strategy for materials synthesis, literature already contains reports on the synthesis of hollow iron oxide structures,<sup>93-98</sup> where inorganic anions, such as sulfates or phosphates, are believed to stabilize the outer surface through coordination by forming complex compounds. The complex compounds are stable enough to protect the outer layer from rapid dissolution so that the unprotected interior materials are dissolved preferentially, producing a hollow structure.

Since we introduced the concept of “Surface-Protected Etching” in 2007, we have been exploring its potential in producing hollow and porous nanostructures. A typical “surface-protected etching” process involves pre-coating of solid oxide particles with a protecting layer of polymeric ligands and subsequent preferential etching of material from the interior of the particles using an appropriate etching agent, as illustrated in Scheme 3.1. The protection by the polymer allows the oxide particles to retain their

original size, while selective etching at the interior produces porous structures and eventually hollow spheres. By rationally choosing the reaction components, this concept represents a general strategy for the production of porous and hollow structures. First, an etching agent is needed to effectively dissolve the oxide material. Second, the etching agent needs to be able to diffuse through the oxide structures. Sol-gel derived colloidal oxides are typically grown by the condensation of their nanoparticle precursors so that their relatively loose structure allows penetration by small dissolved chemical species.<sup>99</sup> Finally, a polymeric ligand is needed to effectively protect the colloid surface from rapid dissolution by etchant. A polymer chain containing multiple binding groups can “cross-link” near surface nanoparticles and increase their stability against etching. The relatively bulky size of the polymeric ligands means negligible infiltration of the ligand into the oxide material via grain boundaries, ensuring high selectivity of the ligand in protecting material near particle surfaces. Compared to the traditional template-based methods, the “surface-protected etching” process is inherently advantageous in many regards: without the involvement of multi-step heterogeneous nucleation and growth processes, this method is simpler and more reproducible. Because no extra template is needed, the process is cost-effective and can be easily scaled up. More importantly, this process allows convenient incorporation of functional nanomaterials into the hollow structures to form composite nanostructures.



**Scheme 3.1** Schematic illustration of the concept of “surface-protected etching” for transforming solid structures into hollow structures with permeable shells. Etching of silica ( $\text{SiO}_2$ ) colloids with  $\text{NaOH}$  under the protection of PVP is used as an example to describe the process. Reproduced with permission from Ref. 100. Copyright © 2010 WILEY-VCH.

We choose PVP as the surface protecting agent because of the strong hydrogen bonds that can form between its carbonyl groups and the hydroxyls on a silica surface.<sup>101-103</sup> Although surface adsorption of PVP on silica can readily occur at room temperature,<sup>103,104</sup> we find that a more robust coating forms upon refluxing silica colloids in an aqueous solution of PVP. At a fixed concentration of SiO<sub>2</sub>/PVP mixture, the amount of PVP adsorbed onto silica surfaces can be conveniently tuned by controlling the refluxing time. As shown in Figure 3.1a, the weight loss of the PVP-treated samples after calcination in air increases significantly with the refluxing time (from initial 7.9% to ~ 26.8% after 3 hrs of treatment), indicating that higher loadings of PVP are achieved by longer refluxing times. The formation of hydrogen bonds between PVP and silica has also been verified by the shift of C=O stretching band of PVP originally at ~1678 cm<sup>-1</sup> to a lower frequency of ~1653 cm<sup>-1</sup> in the FTIR.<sup>105</sup> The presence of PVP on the surface dramatically increases the stability of silica spheres against etching by NaOH solution. The originally turbid solution gradually becomes transparent when the silica colloids are etched with NaOH at room temperature. The transition time to the transparent state (as defined by 75% transmittance at the wavelength of 700 nm) is used to estimate the relative stability of the silica spheres with different PVP loadings. As shown in Figure 3.1a, the etching of pristine silica completes in ~ 20 min, while PVP-modified spheres survive up to 180 min in NaOH solution following prolonged (3 hrs) refluxing in PVP.

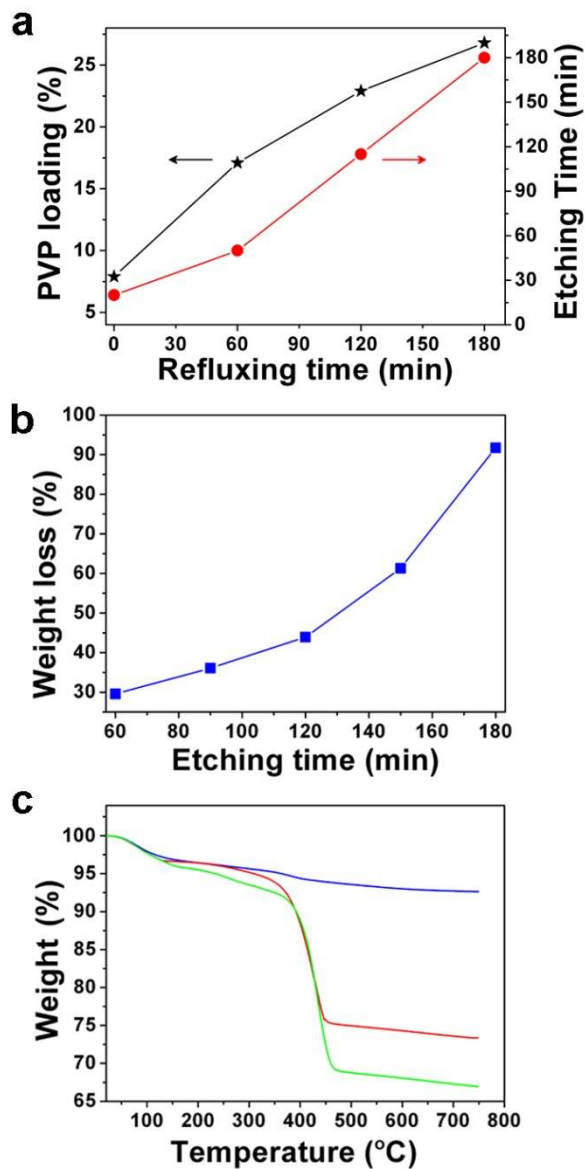


**Figure 3.1** (a) Dependence of PVP loading (left) and the relative stability against NaOH etching (right) of SiO<sub>2</sub> spheres on the refluxing time of SiO<sub>2</sub>/PVP mixture. (b) The weight loss of the PVP treated SiO<sub>2</sub> spheres after etching with NaOH for various periods. (c) TGA curves of pure silica (blue), PVP treated silica (red), and silica spheres after protected etching for 3hrs (green). The PVP treated silica particles used in (b) and (c) have been refluxed in an aqueous solution of PVP for 3hrs. Reproduced with permission from Ref. 106. Copyright © 2008 American Chemical Society.

Silica spheres lose mass during etching although their outer diameter displays almost no change, in agreement with the surface-protected etching mechanism. Figure 3.1b shows the weight loss of the samples in comparison to the pristine silica spheres after etching in NaOH solution for various periods. It is clear that more of the silica is dissolved into silicate species upon longer etching, resulting in a gradual weight loss up to 90% in 3 hours. The overall size and the particle concentration do not show apparent change during etching as confirmed by transmission electron microscopy (TEM, Figure 3.2) and dark-field optical microscopy studies, respectively, suggesting the formation of porous or hollow structure inside the spheres.

Thermogravimetric analysis (TGA) provides more quantitative information about the adsorption of PVP on silica surfaces. As shown in Figure 3.2c, heating pristine silica particles in a nitrogen flow to  $\sim 750^{\circ}\text{C}$  leads only to a small weight loss ( $\sim 7.1\%$ ) due to removal of adsorbed water and loss of water released by slow condensation of silanol groups. In contrast, a dry powder of PVP treated silica particles displays a significant weight loss of  $\sim 18.3\text{ wt}\%$  in the temperature interval between  $300$  and  $450^{\circ}\text{C}$ , which can be attributed to decomposition of the adsorbed PVP. If the same PVP-coated spheres are etched with NaOH for 3 hrs, the TGA measurement suggests a weight loss of  $23.8\%$  in the same temperature interval, consistent with a larger weight fraction of PVP resulting from partial removal of silica during etching.

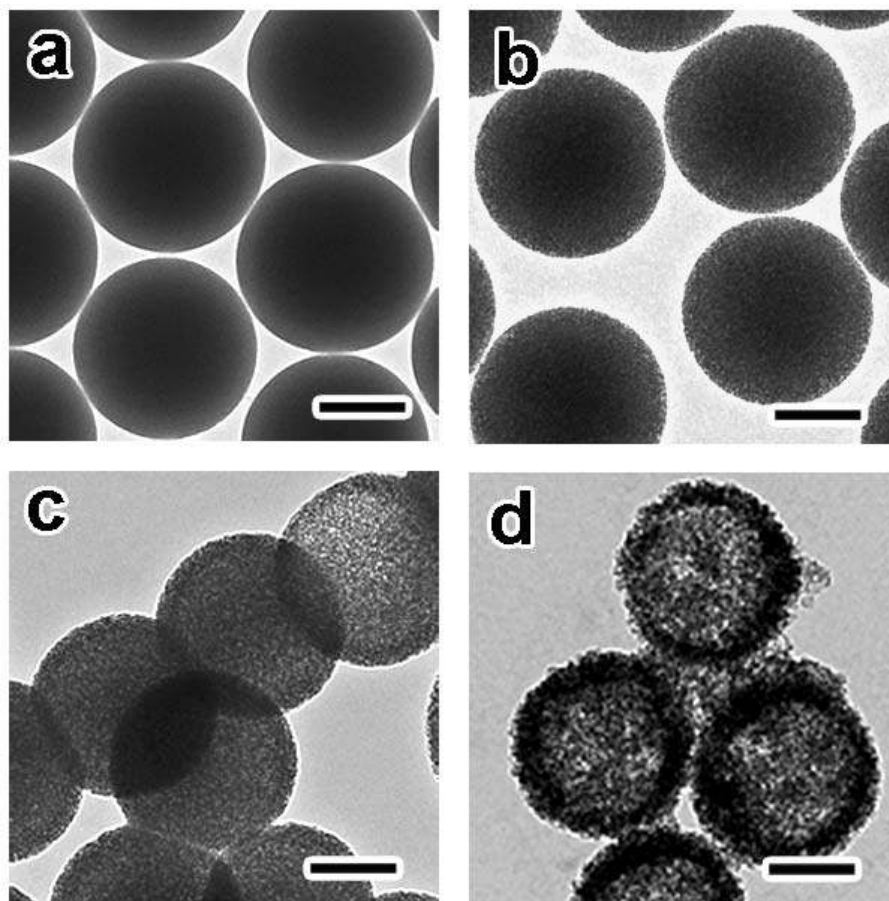


**Figure 3.2** TEM images showing the morphology of PVP-treated SiO<sub>2</sub> particles after etching by NaOH for (a) 0hr; (b) 1hr; (c) 2hr 45min; and (d) 3hr. Before etching, the silica particles have been refluxed in an aqueous solution of PVP for 3hrs. The outer diameter of the particles changes only slightly from  $436\pm 16$  nm in sample (a) to  $430\pm 22$  nm in sample (d). All scale bars are 200 nm. Reproduced with permission from Ref. 106. Copyright © 2008 American Chemical Society.



Protection by surface-bound PVP leads to the formation of silica spheres with porous shells. It is well known that pristine silica spheres shrink rapidly in strong base solution and finally dissolve into silicate oligomers.<sup>107,108</sup> Interestingly, as shown in Figure 3.2, PVP-modified spheres do not decrease in diameter during the etching process. Starting as solid spheres, the particles become porous as indicated by the lower contrast in TEM images after etching for ~ 60 min. While the average diameter of the particles remains constant, the sample loses 29.5% of its original mass upon etching. Because the silica surface is protected by PVP, OH<sup>-</sup> ions cannot dissolve the near surface layer rapidly. Instead, the small ions diffuse into the interior of silica spheres and lead to a relatively higher etching rate inside, eventually producing hollow spheres upon continued etching (Figure 3.2c). Continued reaction further removes material from particle cores, making the appearance of hollow structures more pronounced (Figure 3.2d). Simultaneously, the shells come to appear rougher and less homogenous in transmission contrast, which can be attributed to partial and localized etching of the remaining shell material. The concept for this surface-protected etching process may also account for the direct conversion of solid TiO<sub>2</sub> spheres into hollow microcapsules that we reported previously.<sup>85</sup> Interestingly, unlike the case of TiO<sub>2</sub>, in which the hollow particles deflate and collapse onto the substrate upon drying, the SiO<sub>2</sub> hollow spheres are robust enough to maintain a spherical shape upon preparation, isolation and imaging.

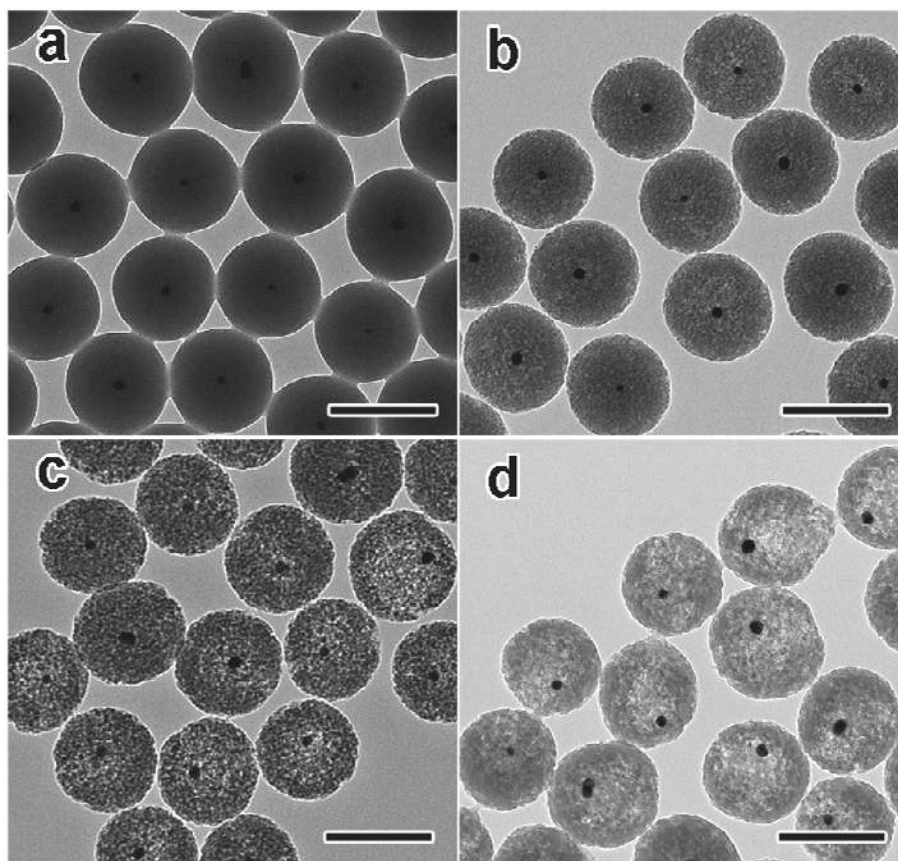


**Figure 3.3** TEM images showing the structure evolution of Au@SiO<sub>2</sub> core-shell particles: (a) the original samples; and (b-d) the samples after etching by NaOH for (b) 2hr; (c) 2hr 45min; and (d) 3hr. The average outer diameters of the particles are: (a) 180±12nm, (b) 180±16nm; (c) 180±16nm, and (d) 178±24 nm. Before etching, the silica particles have been refluxed in an aqueous solution of PVP for 3hrs. All scale bars are 200 nm. Reproduced with permission from Ref. 106. Copyright © 2008 American Chemical Society.

When placed in an etching solution for much longer times, the shells are observed to disintegrate into smaller fragments rather than shrink into thinner, deformable shells. Liz-Marzán has also reported a procedure for the formation of silica hollow nanostructures by taking advantage of the different aqueous solubility of silica grown under basic and acidic conditions.<sup>107</sup>

The simple process reported here can also be conveniently used to convert various silica-coated composite particles into porous and hollow structures. As a demonstration, we show here the formation of monodisperse Au@SiO<sub>2</sub> yolk-shell nanostructures through this surface-protected etching process and their use as nanoscale reactors for catalytic reactions. The solid Au@SiO<sub>2</sub> core-shell particles can be conveniently prepared using the modified sol-gel procedure reported previously (Figure 3.3a).<sup>109</sup> With the surface protection from PVP, the silica coating slowly becomes porous upon NaOH etching (Figure 3.3b). As shown in Figure 4c and 4d, continued etching gradually leads to the formation of yolk-shell structures as evidenced by the reduced contrast at the center and also the displacement of the Au core from the central position.

We further demonstrate that the surface-protected etching allows convenient control over the permeation of molecules through the shells. The Au catalyzed reduction of 4-nitrophenol (4-NP) by NaBH<sub>4</sub> to 4-aminophenol (4-AP) is chosen as a model reaction.<sup>76,110,111</sup> Since only a small amount of catalyst particles are used, light

scattering due to the Au particle and silica spheres is negligible in comparison to characteristic absorption by 4-NP at 400 nm and 4-AP at 295 nm. The reduction reaction does not proceed without the Au catalyst even in a large excess of NaBH<sub>4</sub>, as evidenced by a constant absorption peak at 400 nm. However, when a trace amount of Au@SiO<sub>2</sub> yolk-shell catalysts is introduced into the solution, the absorption at 400 nm decreases and absorption at 295 nm increases gradually (Figure 3.4a), indicating the reduction of 4-NP into 4-AP. The complete conversion of 4-NP can also be visually appreciated by the gradual change of the originally bright-yellow solution into a colorless one.

As shown in Figure 3.4b, the surface-protected etching process allows the precise control of the openings of the silica shells, therefore the permeability of the reagents through the shells, and eventually the kinetics of the catalytic reactions. Unetched silica shells are evidently impenetrable to 4-NP as no measurable catalytic activity can be detected over the duration of 5 hr. The sample etched with NaOH solution for 1.5 hrs shows a slow conversion of 4-NP, indicating a slightly porous silica layer. The conversion reaches ~ 50% after ~ 6hr, and completes within 2 days. As shown in Figure 3.4b, the catalytic activity increases consistently for catalysts with more extensive etching, demonstrating the degree of control over shell porosity and permeability achievable by the surface-protected etching scheme.

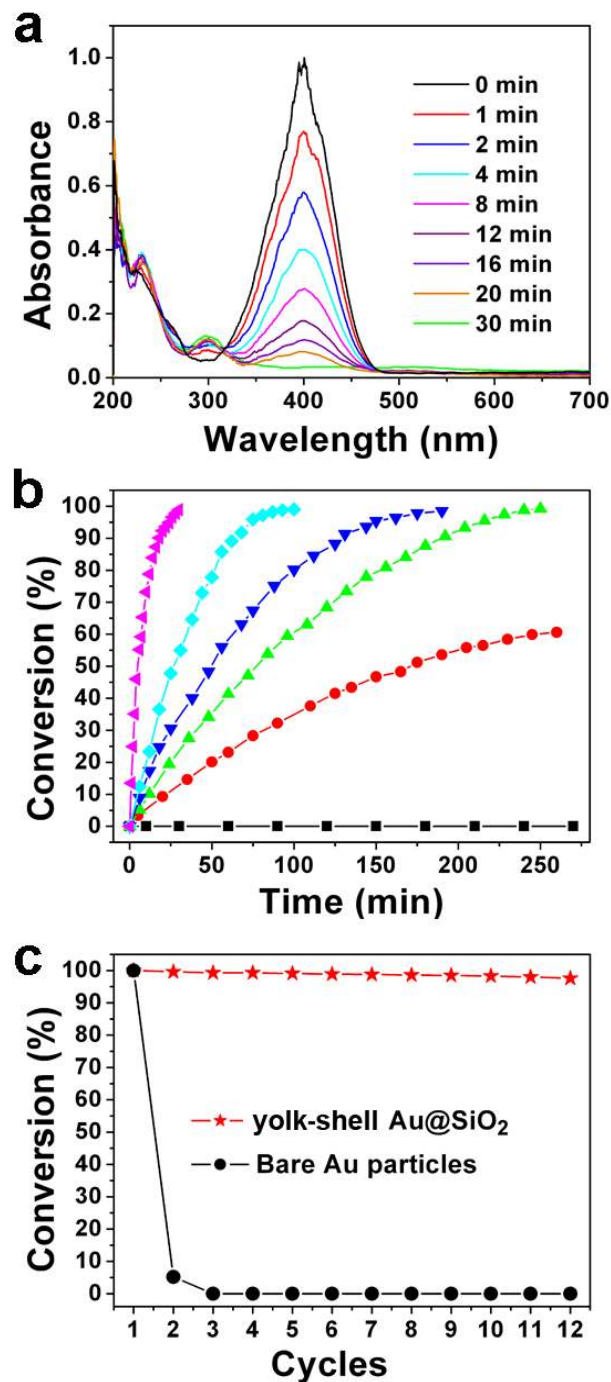
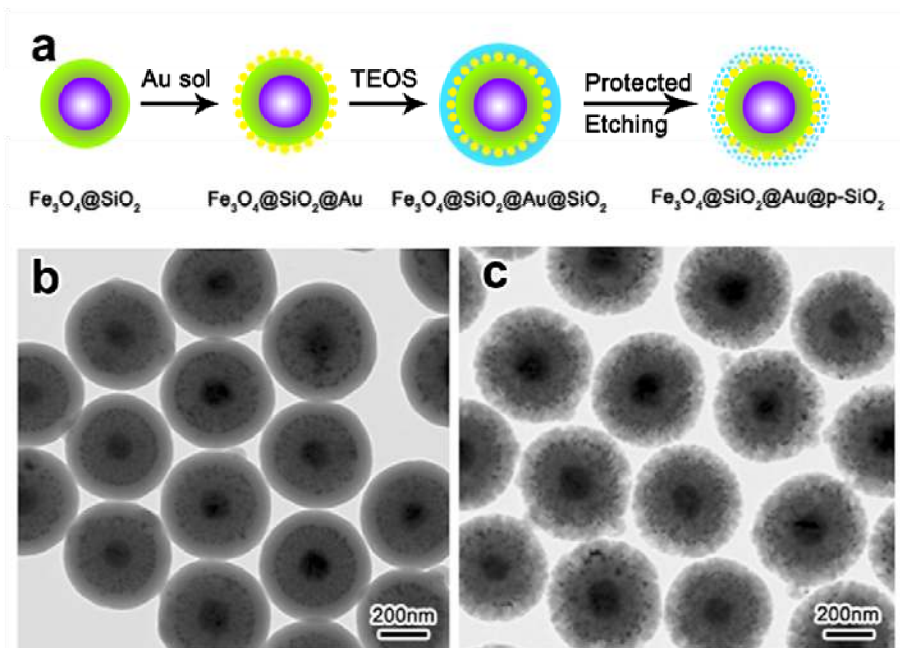


**Figure 3.4** (a) UV-Vis spectra showing reduction of 4-NP. (b) Conversion of 4-NP using Au@SiO<sub>2</sub> catalyst after etching for: ■ 0 min; ● 90 min; ▲ 2 hr; ▼ 150 min; ◆ 165 min; and ◄ 3 hr. (c) Conversion of 4-NP in twelve successive cycles of reduction with: ★ Au@SiO<sub>2</sub>; and ● bare Au nanoparticles. Reproduced with permission from Ref. 106. Copyright © 2008 American Chemical Society.

Stability against coalescence is a very important issue for nanocrystal-based catalysts.<sup>109,112,113</sup> We use the NaBH<sub>4</sub>/4-NP system to demonstrate the excellent stability of the Au@SiO<sub>2</sub> yolk-shell structures. In this case, we increase the concentration of reagents and catalysts by 20 times so that the reaction completes within ~ 10 min. In each cycle, after 5 min of reaction, the sample was rapidly diluted 20 times for UV-Vis measurements in order to determine the conversion of 4-NP. Then, catalysts were separated from solution. As shown in Figure 3.4c, the catalysts are still highly active after twelve successive cycles of reactions, with a conversion rate close to 100% within 5-min reaction periods. The optical absorption and morphology of the catalysts remained almost no change after many cycles of catalytic reactions. For comparison, uncoated Au nanoparticles were also used as the catalyst for the same reaction. Upon addition of the freshly prepared Au sol, the NaBH<sub>4</sub>/4-NP solution became dark immediately, indicating the occurrence of severe aggregation.<sup>112,114</sup> The conversion within the 5-min period drops rapidly after only one cycle, which can be naturally attributed to the significantly reduced surface area as the result of aggregation of catalyst particles. The presence of the porous silica shell is sufficient for stabilizing the catalytic nanoparticles by preventing their aggregation; at the same time, the shells are permeable enough so that catalytic surfaces remain accessible to the reactants and products.

### **3.4 Core–Satellite Nanocomposite Catalysts Protected by a Porous Silica Shell**

To achieve higher catalyst loadings, an alternative version based on core-satellite structured nanoreactors has been developed which includes multiple catalyst nanoparticles in each nanoreactor. Figure 3.5a outlines the procedures involved. A monolayer of metal nanocatalysts is first immobilized on the surface of the SiO<sub>2</sub> colloids through electrostatic interactions or chemical bonds formed through coupling agents. One typical procedure for nanoparticle immobilization involves the surface modification of plain SiO<sub>2</sub> colloids with 3-aminopropyltriethoxysilane (APTES) followed by the controlled adsorption of citrate-stabilized metal nanoparticles such as Pt and Au.<sup>88</sup> The loading of metallic nanocatalysts can be well tuned by controlling the total amount added during this step. The metal nanoparticles are then over-coated with another layer of SiO<sub>2</sub> of the desired thickness to fix them onto the surface of the initial support (Figure 3.5b). Finally, the surface-protected etching scheme is applied to transform the outer shell into a mesoporous structure, exposing the catalyst particles to outside chemical species (Figure 3.5c).





The additional incorporation of magnetic materials into the colloidal supports may offer the benefit of facile recovery and regeneration of the catalysts, particularly for liquid-phase reactions.<sup>115-119</sup> For this purpose, superparamagnetic nanocrystals are preferred, as they are not subject to strong, permanent magnetic interactions in the absence of external fields. Due to their small magnetic moment, however, it is very difficult to efficiently separate them from solution.<sup>120,121</sup> The strategy of forming clusters of magnetic nanoparticles is a way to increase the magnetic moment per colloid while avoiding the superparamagnetic-ferromagnetic transition associated with the increased domain size. Our group recently developed a high-temperature solution-phase hydrolysis approach for the synthesis of highly water-dispersible Fe<sub>3</sub>O<sub>4</sub> CNCs with uniform sizes tunable from ~30 to ~180 nm.<sup>122,123</sup> Each CNC particle is composed of many single magnetite crystallites of ~10 nm, thus retaining superparamagnetic characteristics. The resulting strong interaction of the Fe<sub>3</sub>O<sub>4</sub> particles with external magnetic fields can then be used for their easy separation from solution under relatively low magnetic field gradients. The as-synthesized Fe<sub>3</sub>O<sub>4</sub> particles can be conveniently coated with a thin transition layer of silica, which permits further immobilization of metal nanocatalysts and overcoating with another layer of silica for enhanced stability. After surface-protected etching of the surface layer, the composite nanocatalyst structures show good recyclability under external magnetic field when used in solution-phase catalysis.

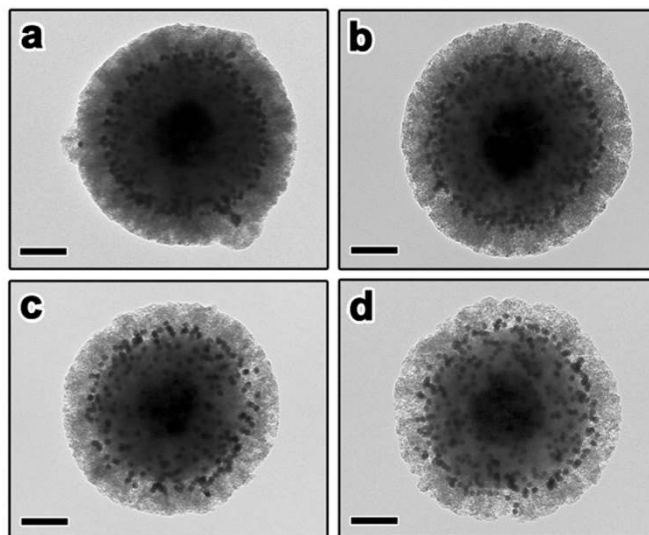


**Figure 3.6** TEM images of  $\text{Fe}_3\text{O}_4/\text{SiO}_2/\text{Au}/\text{porous-SiO}_2$  composite colloids collected after different periods of etching: a) 50 min; b) 65 min; c) 85 min; and d) 95 min. All scale bars are 100 nm. Adapted with permission from Ref. 88. Copyright © 2008 WILEY-VCH.

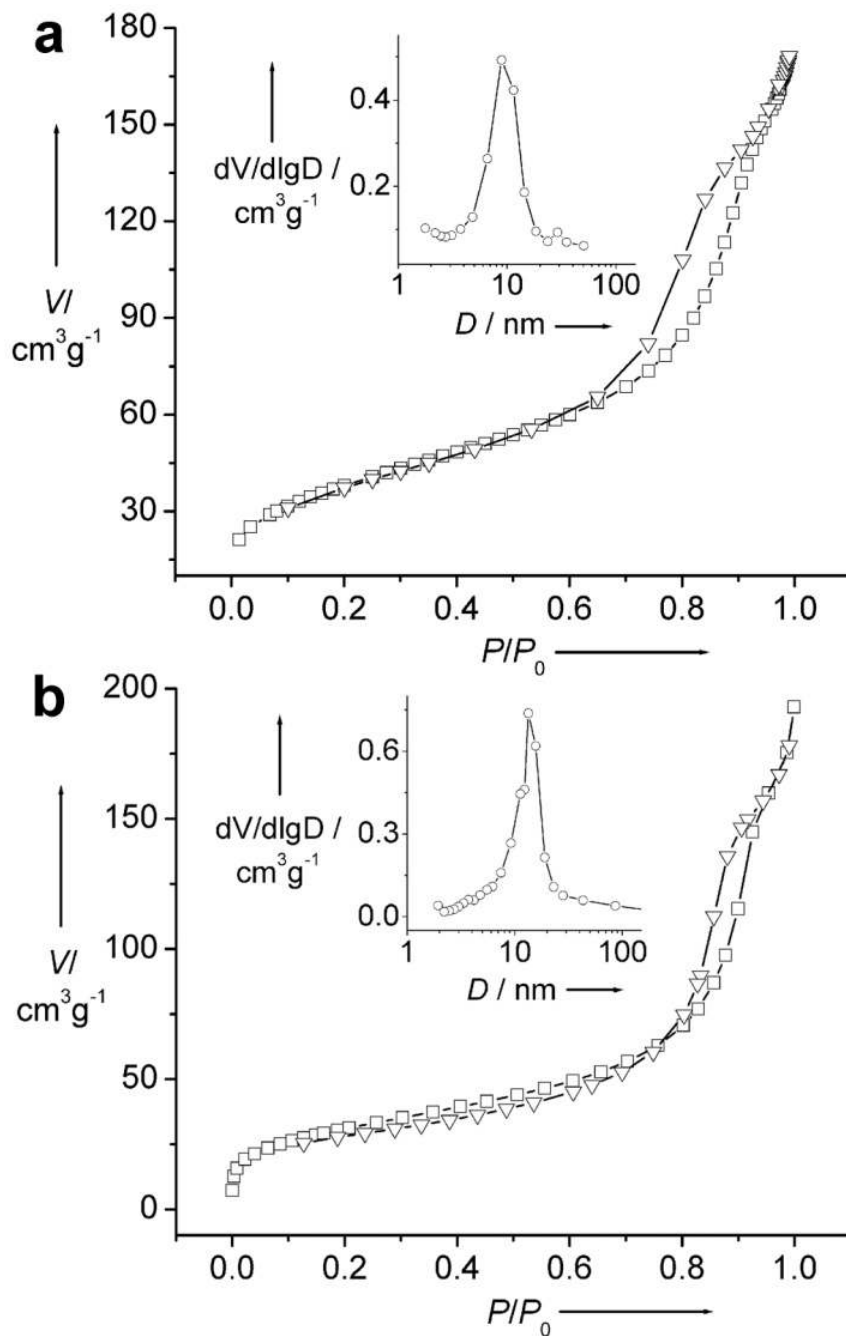
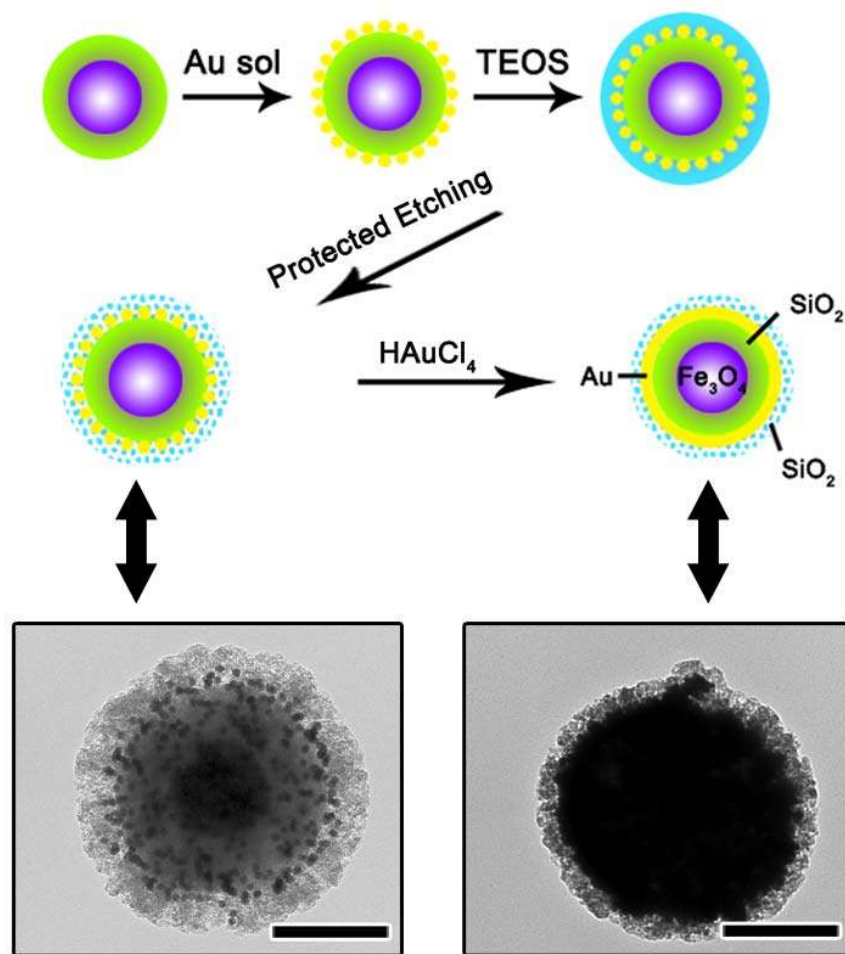


**Figure 3.7**  $N_2$  adsorption/desorption isotherms for the nanocomposite particles displayed in 5 b) and 5 c), respectively. Insets show the corresponding BJH pore size distributions. Adapted with permission from Ref. 88. Copyright 2008 © WILEY-VCH.

Both the extent of etching and the porosity of silica shell can be well controlled by monitoring the transmittance of the colloidal solution. At extended etching times, more SiO<sub>2</sub> material dissolves in the form of soluble silicate oligomers, and accordingly, the transmittance increases. Figure 3.6 shows the TEM images of four samples collected after 50, 65, 85, and 95 minutes of etching. Careful inspection of those TEM images indicates that the shells become rougher and less homogeneous with increasing etching, suggesting the formation of porous structures. Thanks to the surface protection of PVP, the shell thickness shows no apparent change after moderate etching, while the average pore size increases. Figure 3.7a shows representative nitrogen adsorption/desorption isotherms, together with the corresponding pore size distribution, of the sample displayed in Figure 3.6b. The BET surface area and the single-point total pore volume for this sample came out to be 136.6 m<sup>2</sup>g<sup>-1</sup> and 0.25 cm<sup>3</sup>g<sup>-1</sup>, respectively, both relatively large values considering the fact that the solid core and Au nanoparticles have been included in the calculations. The average BJH pore diameter calculated from the desorption branch of the isotherms was determined to be 8.8 nm. For comparison, the values for the BET surface area, total pore volume, and pore diameter of the sample displayed in Figure 3.6c were calculated at 112.8 m<sup>2</sup>g<sup>-1</sup>, 0.27 cm<sup>3</sup>g<sup>-1</sup> and 13.2 nm, respectively (Figure 3.7b). The increase in pore size and volume with etching time is consistent with TEM observations of a gradual decrease in the transmission contrast of the shells.

The tunable porosity attainable by regulating the etching time indicated above has been verified by testing the activity of the resulting catalysts toward the reduction of 4-NP. Four catalysts with different degrees of etching, as displayed in Figure 3.6, were used to catalyze this reaction. As the reaction follows first-order kinetics, the rate constant  $k$  could be easily calculated from analysis of the conversion versus time, and turnover frequencies, defined as the number of moles of reduced 4-NP per mole surface Au atoms per hour when the conversion has reached 90%, were calculated as well.<sup>88</sup> Both the rate constant and the TOF increase consistently with the degree of etching, suggesting higher catalytic efficiencies with larger mesopores. We attribute the increased catalytic efficiency to the enhanced diffusion of reactants through the larger pores. It is worth noting, however, that although mass transfer is generally enhanced with larger pores, over-etching must be avoided in order to retain the Au particles while at the same time effectively isolating neighboring Au particles from each other. Our recent work has shown that it is possible to take advantage of the tunable porosity of SiO<sub>2</sub> shells for the fabrication of Au nanoshells with controllable optical properties, as shown in Scheme 3.2.<sup>89</sup> By tuning the pore structure of the SiO<sub>2</sub> networks through etching, we have been able to control the shape/size of the Au nanoparticles and consequently the inter-particle plasmon coupling using a seeded growth process.



**Scheme 3.2** Schematic illustration of the procedures for the fabrication of Au nanoshells containing superparamagnetic Fe<sub>3</sub>O<sub>4</sub> cores. A unique porous silica layer is produced by a surface-protected etching process, and then utilized to control the seeded growth of Au nanoshells with enhanced reproducibility and structural and optical stability. The TEM images show the Fe<sub>3</sub>O<sub>4</sub>@SiO<sub>2</sub> cores loaded with Au seeds (left) and then further over-coated with an additional layer of silica (right). Scale bars are 200 nm. Adapted with permission from Ref. 124. Copyright © 2010 WILEY-VCH.

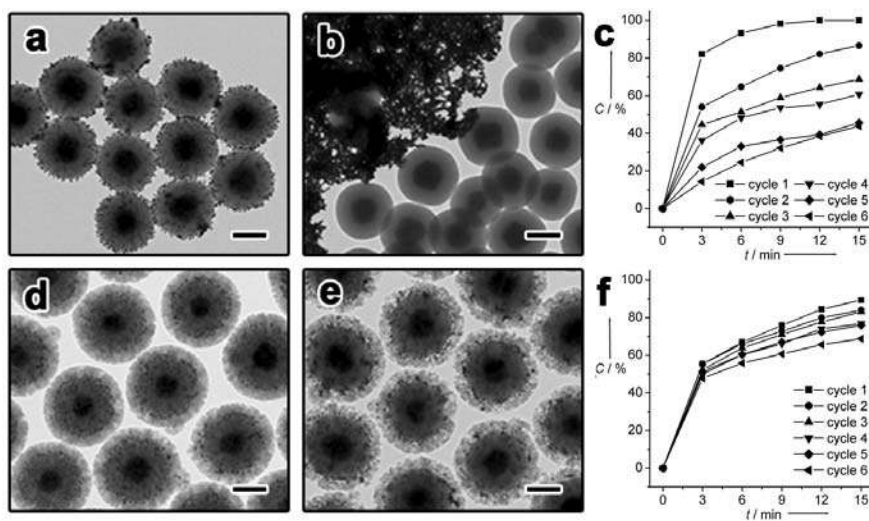


**Figure 3.8** (a-e) TEM images of Au nanoparticles supported on  $\text{Fe}_3\text{O}_4@\text{SiO}_2$  core-shell spheres without (a, b) and with (d, e) porous  $\text{SiO}_2$  shells before (a, d) and after (b, e) catalyzing the liquid-phase reduction reaction of 4-NP by  $\text{NaBH}_4$ . (c, f) Conversion (C) of 4-NP as a function of reaction time (t) in six successive cycles of reduction and magnetic recycling using  $\text{Fe}_3\text{O}_4/\text{SiO}_2/\text{Au}$  (c) and  $\text{Fe}_3\text{O}_4/\text{SiO}_2/\text{Au}/\text{porous SiO}_2$  (f) core-satellite composite catalysts. Adapted with permission from Ref. 88. Copyright © 2008 WILEY-VCH.

As mentioned before, catalysts can also be made in this case by adding  $\text{Fe}_3\text{O}_4$  particles to make them easy to recover efficiently from the reaction solution by using external magnetic fields. This separation can be performed in many cycles without significant losses. The mesoporous  $\text{SiO}_2$  framework still effectively stabilizes the catalyst nanoparticles and prevents reduction in activity caused by coagulation, helping make the catalyst reusable after multiple cycles of reactions. In Figure 3.8, the structural stability and catalytic performance of  $\text{Fe}_3\text{O}_4/\text{SiO}_2/\text{Au}$  nanocomposites are compared with versus without the protection in six successive cycles of reactions. In the first cycle, the unprotected catalysts show high activity. However, the catalytic reactions on the Au surface destabilize the Au-NH<sub>2</sub> interactions so that the particles gradually detach from the support surface and form large black aggregates (Figure 3.8b). Accordingly, the conversion rate drops rapidly in the following cycles of reactions. On the other hand, the Au catalysts protected by porous  $\text{SiO}_2$  maintain their activity well into the six successive cycles (Figure 3.8d-f), with conversion of 4-NP dropping only slightly, primarily due to the removal of a small portion (3.6%) of the solution in each cycle for sampling. The porous  $\text{SiO}_2$ -protected catalysts appear much more durable in the following cycles of reactions although the initial catalytic efficiency is slightly lower than that of the unprotected Au catalyst. As shown in Figure 3.8e, the Au catalysts protected by the porous  $\text{SiO}_2$  shell remain well-dispersed on the core surfaces after the reactions.



### 3.5 Catalysis in Gas Phase

In addition to the successful applications of our newly designed catalysts in liquid-phase catalytic reactions, we have recently tested their performance for gas-phase reactions. In this case, platinum (Pt) was chosen as the transition metal catalyst to be used because of its broad industrial applications, including oil processing, other hydrocarbon conversions, and catalytic converters in automotive exhaust emission controls. Here, we demonstrate that the core-satellite structured nanoreactors prepared through the surface-protected etching process can be used for catalyzing gas-phase reactions and preventing the coalescence of the catalyst nanoparticles.

The preparation process of these core-satellite nanocatalysts is similar to that of the previous core-satellite structures. The surface of the colloidal SiO<sub>2</sub> supports is pre-modified with aminosilane so that citrate-stabilized Pt nanoparticles can be loaded onto the surface of silica beads through the strong chemical affinity between the Pt and the primary amines. The loading of Pt nanoparticles can be well controlled by simply tuning the ratio of Pt precursor to silica beads used. In the presence of PVP, the composite colloids are then over-coated with another layer of silica to fully encapsulate the Pt nanoparticles inside the silica matrix. This robust sol-gel process allows for the precisely manipulation of the thickness of the SiO<sub>2</sub> shells by controlling the amount of TEOS precursor added. As shown in Figure 3.9a, under carefully controlled conditions,

it was possible to produce SiO<sub>2</sub> shells several nanometers (~3-4 nm) in thickness this way. Upon surface-protected etching with NaOH solution, the outer silica layer becomes mesoporous, exposing the Pt nanocatalysts to the outside chemical species.

We have noticed previously that the inner SiO<sub>2</sub> cores display enhanced stability against etching due to the presence of additional PVP molecules on their surface.<sup>86</sup> As a result, the SiO<sub>2</sub> etching is mainly limited to the outer layer unless the samples are dispersed in NaOH solution for a prolonged period. In the previous cases, the outer silica layer was relatively thick, so the changes in the thickness of the outer shell were negligible. However, in cases where the shell thickness was only several nanometers, its change became obvious, because, at least in part, to the relatively smaller amount of SiO<sub>2</sub> available for etching. As shown in Figure 3.9b, after etching for 40 min, the SiO<sub>2</sub> shell not only becomes porous, but also shows a small but discernable reduction in thickness; when the etching process is extended to 60 min, only a very thin layer of SiO<sub>2</sub> coating can be observed (Figure 3.9c). This is confirmed by the fact that although no detachment of Pt particles is observed during the etching process up to 60 min, further etching not only completely removes the SiO<sub>2</sub> shell but also causes the detachment of the Pt nanoparticles (data not shown).

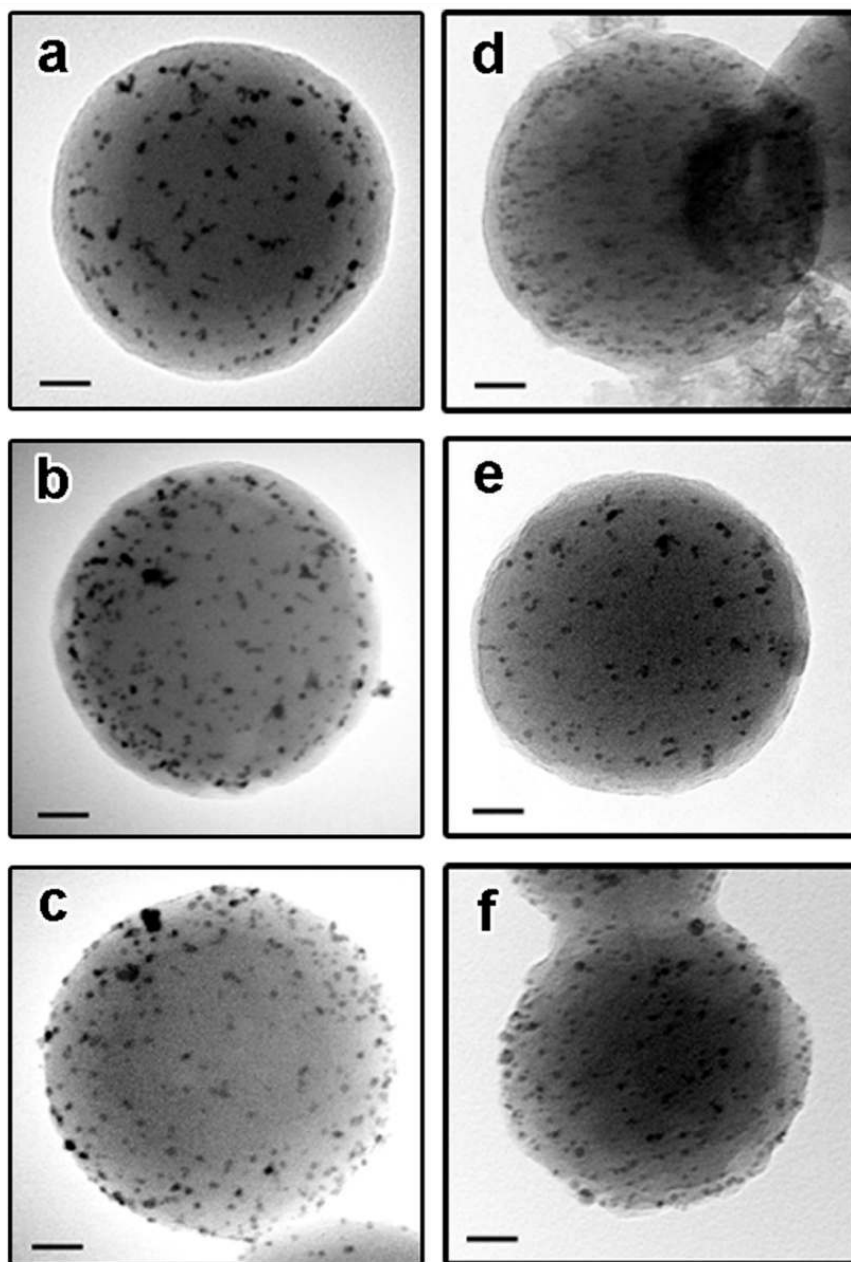


**Figure 3.9** (a-c) TEM images of  $\text{SiO}_2/\text{Pt}/\text{SiO}_2$  composite particles after etching for (a, d) 0 min, (b, e) 40 min, and (c, f) 60 min, before (a-c) and after (d-f) pretreatment following three oxidation-reduction cycles at 350 °C. All scale bars are 20 nm. Reproduced with permission from Ref. 100. Copyright © 2010 WILEY-VCH.

Carbon monoxide (CO) adsorption was used to test the accessibility of the Pt nanoparticles in these catalysts, by using a cell specifically designed for the *in-situ* characterization of catalysts using infrared absorption spectroscopy.<sup>125,126</sup> After drying at 150 °C, all the samples were treated by three oxidation-reduction cycles at 350 °C in order to clean the Pt surface by completely removing the residual organic species. Figures 3.9d-f show typical TEM images obtained for the thermally treated samples. Those images clearly show that the thermal treatment does not significantly change either the average size or the aggregation state of the Pt nanoparticles, already suggesting an enhanced thermal stability for such structures. After activation, equal amounts of each catalyst were made into thin disks and placed one at a time in the transmission IR cell for the CO adsorption experiments. After pumping, the samples were cooled down to below -150 °C, and then exposed to 10 Torr of CO for 5 min. Transmission IR spectra were taken at every 10 °C interval while the entire cell was warming up. Figure 3.10 shows the resulting IR spectra obtained this way for CO adsorbed on the catalysts consisting of Pt nanoparticles embedded in the composite structures. Of particular relevance here are the peaks seen at around 2090 cm<sup>-1</sup>, which correspond to the C–O stretching vibrational mode of CO molecules adsorbed linearly on-top of a single Pt atom. The data show that, with increasing temperature, the CO desorbs gradually until it has been removed completely from the surface by temperatures below 200 °C.

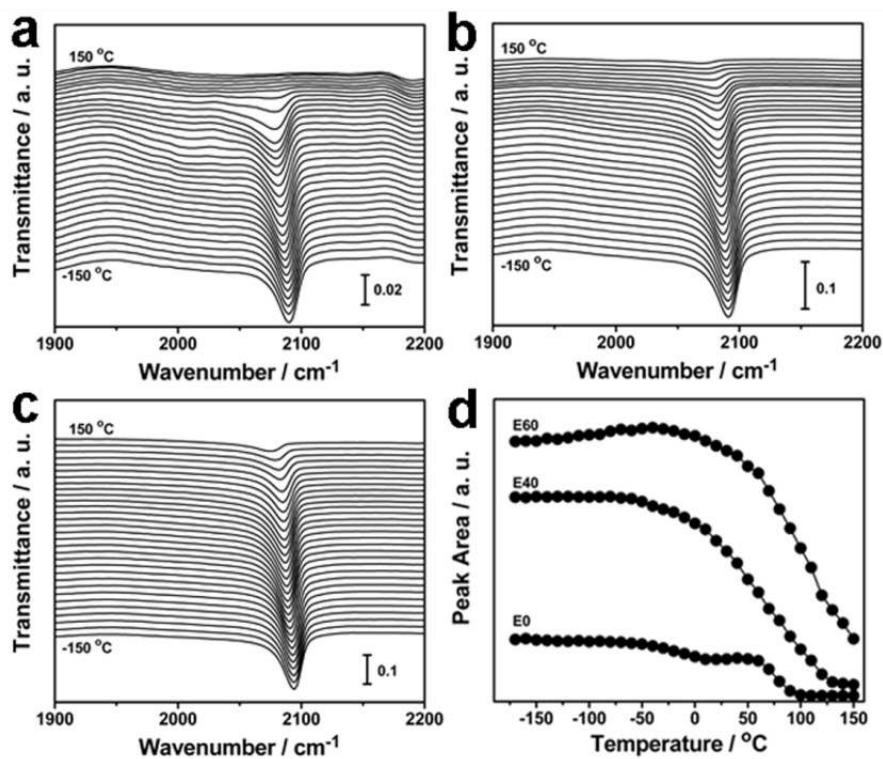


**Figure 3.10** (a-c) Transmission IR absorption spectra of CO adsorbed on Pt nanoparticles dispersed on silica beads and coated with a layer of mesoporous silica deposited afterwards, as explained in the text. Data are reported for the catalysts before etching (a, **E0**) and after etching for 40 min (b, **E40**) and 60 min (c, **E60**), respectively. (d) Peak areas of the peak due to the C–O stretching vibrational mode,  $\nu(\text{CO})$ , of CO adsorbed linearly on-top of single Pt atoms within the Pt nanoparticles. The peak area data are reported for all three catalysts as a function of catalyst temperature. Reproduced with permission from Ref. 100. Copyright © 2010 WILEY-VCH.

It is also seen that, at greater thicknesses, the silica coating can effectively limit the access of CO molecules to the surface of the catalysts: note the almost complete suppression of CO uptake on the catalyst where no etching was carried out. When the silica coating is made as thin as a few nanometers, however, it was found that CO can penetrate the silica shell and adsorb onto the Pt nanoparticle surface. The difference between the three samples studied here in terms of the total amount of adsorbed CO can be followed by the peak intensity of the CO IR adsorption band (Figure 3.10d). It is seen there that the low-temperature (-250 °C) CO uptake on the catalyst etched for 40 min is ~ 3 times higher than that on the unetched sample (Figure 3.10a, b), and further enhanced in the sample etched for 60 min (Figure 3.10c). The binding strength of the CO on the Pt surface, indicated by both the peak position of the CO IR absorption band and the temperature range where the signal decreases, is approximately the same in all three samples. The catalytic performance of these nanocatalysts was also tested for the promotion of the hydrogenation of 2-butenes, a model reaction for the study of activity and selectivity in non-demanding catalytic processes.<sup>127-130</sup> In this case, the initial rates for the hydrogenation of both *cis*- and *trans*-2-butene to butane have been followed for catalysts with Pt loadings of 1.0 wt%. The conversion efficiency of the catalyst on the silica beads without etching is always the lowest among the three samples (Figure 3.11), suggesting a lower accessibility due to the relatively dense coating of silica.

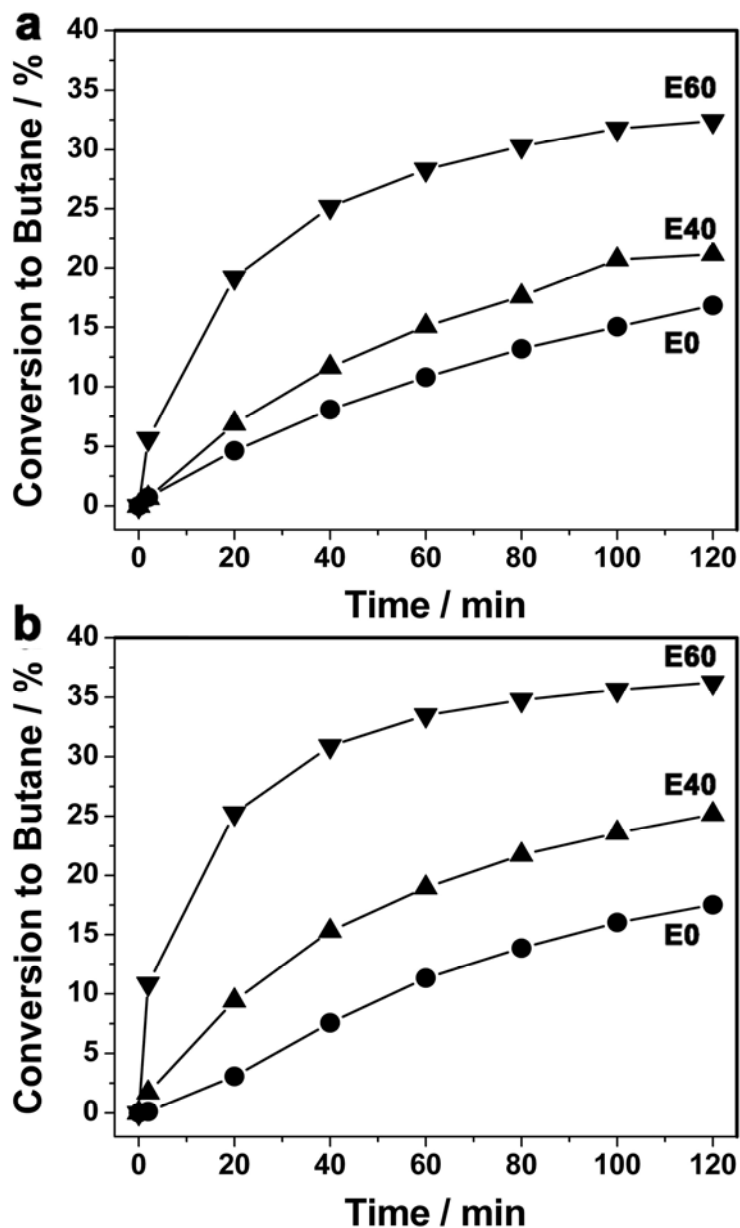


**Figure 3.11** Kinetics of hydrogenation for (a) *cis*-2-butene and (b) *trans*-2-butene to butane with our Pt catalysts, in the form of product accumulation in the batch reactor as a function of time of reaction. Data are provided for SiO<sub>2</sub>/Pt/SiO<sub>2</sub> catalysts unetched (E0), and after etching for 40 min (E40), and 60 min (E60), respectively. Reproduced with permission from Ref. 100. Copyright © 2010 WILEY-VCH.

After pretreatment using the surface-protected etching process, on the other hand, the silica shells became porous and more buried Pt nanoparticles were exposed to the reagent species, and the catalytic activity is enhanced appreciably: the initial catalytic activity for *cis*-2-butenes to butanes was increased from 0.35 mmol g<sup>-1</sup> s<sup>-1</sup> for **E0** catalyst to 3.02 mmol g<sup>-1</sup> s<sup>-1</sup> for **E60** catalyst, while that for *trans*-2-butenes to butanes was increased from 0.06 mmol g<sup>-1</sup> s<sup>-1</sup> for **E0** catalyst to 5.81 mmol g<sup>-1</sup> s<sup>-1</sup> for **E60** catalyst. It should be noted that, with the protection of a porous silica shell, the Pt nanoparticles are fixed to the silica network, and therefore prevented from agglomerating. These catalysts are therefore more thermally stable than those prepared by regular means (data not shown), yet similarly active for the promotion of catalytic reactions.

The effect of the addition of the mesoporous silica layer on the stability of the catalysts was tested. Figure 3.12 displays TEM images for "naked" (i.e., without any mesoporous silica layer) and covered catalysts, calcined at 300, 875, 975, and 1075 K. The differences between the two samples are striking. Specifically, it is clear that the Pt nanoparticles already start to coalesce on the naked silica beads at 875 K, and form large crystalline particles above ~ 1000 K. The protected catalyst, on the other hand, shows virtually no changes upon calcination at temperatures as high as 1075 K. It is clear that the mesoporous layer is quite effective at preserving the size and distribution of the Pt nanoparticles on these catalysts.



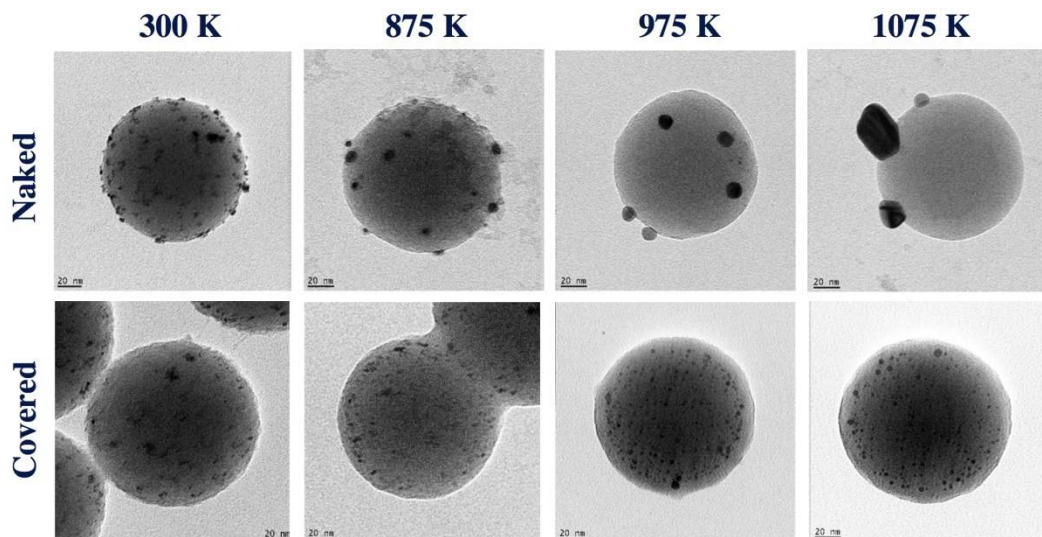


**Figure 3.12** TEM images of Pt nanoparticle/SiO<sub>2</sub> bead catalysts, "naked" (i. e., uncovered, top row) and covered with a layer of mesoporous silica (bottom row) after calcination at, from left to right, 300, 875, 975, and 1075 K. Sintering is already significant by 875 K in the naked samples, whereas no appreciable sintering is observed in the encapsulated samples even after calcination at 1075 K. Reproduced with permission from Ref. 131. Copyright © 2011 Tsinghua University Press and Springer-Verlag Berlin Heidelberg.

### 3.6 Conclusion

Catalysis has always been a very exciting research area for chemists and materials scientists, but has benefited immensely lately from the addition of the new nanoparticle synthesis methodologies. The activity/selectivity and stability of nanocatalysts are two fundamental and interconnected issues in catalysis. By utilizing the surface-protected etching method, we have successfully fabricated several nanostructured catalyst systems, in which metal nanocatalysts are stabilized by a porous shell. We have also demonstrated the ability to exert great control over the porosity of the silica shell and consequently the catalytic reaction rate of the nanoreactor systems. The relationship between the detailed structure of the metal/oxide nanocatalyst reactors and their catalytic behavior has been explored for several model reactions. Compared to unprotected metallic nanocatalysts, the as-obtained nanoreactors have consistently shown excellent stability during the catalytic reactions. The enhanced thermal stability of the metallic catalysts has been demonstrated in both gas- and liquid-phase processes.

The surface-protected etching process described here is a newly developed concept that deserves more research in order to broaden its applicability. We believe that this is a quite general approach that can be used to produce porous and hollow structures from many metal oxide materials: the key for extending its uses is the ability to identify a proper combination of protecting polymer ligands and etching agents applicable for the

oxide of interest. It is our belief that the principles outlined in this article can be potentially used to guide the synthesis of porous and hollow particles from other catalytically important metal oxides such as  $\text{CeO}_2$ ,  $\text{ZrO}_2$ ,  $\text{BaTiO}_3$ . In fact, the literature already contains reports on the dissolution of some of these oxide materials in polyol solvents.<sup>132-134</sup>

The unique structures produced by surface-protected etching can be further used to improve the understanding of the fundamental issues related to nanostructured catalysts, and eventually aid in the rational design of better catalytic systems. As we mentioned before, it has been difficult to differentiate between the contributions from Ostwald ripening and particle coalescence to sintering of metal nanoparticles during catalytic reactions. The encapsulation of catalyst nanoparticles individually within separate porous silica shells eliminates particle coalescence, thus allowing the isolation of one of the mechanisms of particle growth, Ostwald ripening, for systematic studies. An improved understanding of the ripening process may in turn help elucidate the relative contributions of the two competing mechanisms in catalysts without protective shells. Moreover, with catalyst nanoparticles encapsulated in an oxide shell, it will now be possible to rule out complications due to coalescence and conveniently monitor the shape evolution of individual particles, eventually elucidating the mechanism responsible for the changes in morphology seen in catalysts during reactions. In this context, it is

interesting to note that the total energy of metal nanoparticles has many local minima configurations corresponding to different shapes/structures.<sup>135</sup> When the energy barrier between different configurations is low, the nanoparticles may change their shape in response to variations in their size and surface properties,<sup>136,137</sup> and may assume different shapes as their size increases during Ostwald ripening.

More exciting perhaps is the fact that encapsulation of metal nanoparticles in mesoporous silica shells is likely to stabilize certain particle morphologies.<sup>83</sup> In particular, Yang et al. have found that Pt nanoparticles possess significantly higher shape thermal stability when they are supported on SiO<sub>2</sub> surfaces, largely due to the interfacial mixing of Pt and SiO<sub>2</sub> and the negative interface energy.<sup>138</sup> In addition to using metal-support interactions, future work may also explore the possible enhancement in shape stabilization via the deliberate inhibition of Ostwald ripening. Since Ostwald ripening is facilitated by the transport of atomic species, increasing the separation between neighboring nanoparticles may effectively suppress such process. Encapsulation of metal particles in porous shells provides a convenient method to control the average separation between nanoparticles. The presence of porous shells between the particles may also slow down the transport of atomic species among the particles. Therefore, by systematically varying the shell thickness and pore size one may eventually be able to optimize the stability of nanoparticle catalysts both in terms of size and shape.

### 3.7 Reference

- (1) Flanagan, K. A.; Sullivan, J. A.; Mueller-Bunz, H. *Langmuir* **2007**, *23*, 12508.
- (2) Narayanan, R.; El-Sayed, M. A. *J. Am. Chem. Soc.* **2003**, *125*, 8340.
- (3) Kidambi, S.; Dai, J.; Li, J.; Bruening, M. L. *J. Am. Chem. Soc.* **2004**, *126*, 2658.
- (4) Chauhan, B. P. S.; Rathore, J. S.; Bando, T. *J. Am. Chem. Soc.* **2004**, *126*, 8493.
- (5) Lowe, A. B.; Sumerlin, B. S.; Donovan, M. S.; McCormick, C. L. *J. Am. Chem. Soc.* **2002**, *124*, 11562.
- (6) Liu, Y.; Khemtong, C.; Hu, J. *Chem. Commun.* **2004**, 398.
- (7) Ley, S. V.; Mitchell, C.; Pears, D.; Ramarao, C.; Yu, J. Q.; Zhou, W. *Org. Lett.* **2003**, *5*, 4665.
- (8) Grubbs, R. B. *Polym. Rev.* **2007**, *47*, 197.
- (9) Zhao, M.; Sun, L.; Crooks, R. M. *J. Am. Chem. Soc.* **1998**, *120*, 4877.
- (10) Zhao, M.; Crooks, R. M. *Angew. Chem. Int. Ed.* **1999**, *38*, 364.
- (11) Crooks, R. M.; Zhao, M.; Sun, L.; Chechik, V.; Yeung, L. K. *Acc. Chem. Res.* **2001**, *34*, 181.
- (12) Li, Y.; Petroski, J.; El-Sayed, M. A. *J. Phys. Chem. B* **2000**, *104*, 10956.
- (13) Kralik, M.; Biffis, A. *J. Mol. Catal. A* **2001**, *177*, 113.
- (14) Kresge, C. T.; Leonowicz, M. E.; Roth, W. J.; Vartuli, J. C.; Beck, J. S. *Nature* **1992**, *359*, 710.
- (15) Davis, M. E. *Nature* **2002**, *417*, 813.
- (16) Zhao, D.; Feng, J.; Huo, Q.; Melosh, N.; Fredrickson, G. H.; Chmelka, B. F.; Stucky, G. D. *Science* **1998**, *279*, 548.
- (17) Zhao, D.; Huo, Q.; Feng, J.; Chmelka, B. F.; Stucky, G. D. *J. Am. Chem. Soc.* **1998**, *120*, 6024.
- (18) Kónya, Z.; Puentes, V. F.; Kiricsi, I.; Zhu, J.; Alivisatos, P.; Somorjai, G. A. *Catal. Lett.* **2002**, *81*, 137.
- (19) Song, H.; Rioux, R. M.; Hoefelmeyer, J. D.; Komor, R.; Niesz, K.; Grass, M.; Yang, P.; Somorjai, G. A. *J. Am. Chem. Soc.* **2006**, *128*, 3027.

- (20) Zhu, J.; Konya, Z.; Puentes, V. F.; Kiricsi, I.; Miao, C. X.; Ager, J. W.; Alivisatos, A. P.; Somorjai, G. A. *Langmuir* **2003**, *19*, 4396.
- (21) Rioux, R. M.; Song, H.; Hoefelmeyer, J. D.; Yang, P.; Somorjai, G. A. *J. Phys. Chem. B* **2005**, *109*, 2192.
- (22) Zhu, H.; Ma, Z.; Overbury, S.; Dai, S. *Catal. Lett.* **2007**, *116*, 128.
- (23) Niesz, K.; Koebel, M. M.; Somorjai, G. A. *Inorg. Chim. Acta* **2006**, *359*, 2683.
- (24) Bore, M. T.; Mokhonoana, M. P.; Ward, T. L.; Coville, N. J.; Datye, A. K. *Micropor. Mesopor. Mater.* **2006**, *95*, 118.
- (25) Gabaldon, J.; Bore, M.; Datye, A. *Top. Catal.* **2007**, *44*, 253.
- (26) Corma, A.; Garcia, H. *Adv. Synth. Catal.* **2006**, *348*, 1391.
- (27) Hata, H.; Kubo, S.; Kobayashi, Y.; Mallouk, T. E. *J. Am. Chem. Soc.* **2007**, *129*, 3064.
- (28) Budroni, G.; Corma, A. *Angew. Chem. Int. Ed.* **2006**, *45*, 3328.
- (29) Yan, W.; Mahurin, S. M.; Pan, Z.; Overbury, S. H.; Dai, S. *J. Am. Chem. Soc.* **2005**, *127*, 10480.
- (30) Yan, W.; Mahurin, S.; Overbury, S.; Dai, S. *Top. Catal.* **2006**, *39*, 199.
- (31) Fang, C. L.; Qian, K.; Zhu, J. H.; Wang, S. B.; Lv, X. X.; Yu, S. H. *Nanotech.* **2008**, *19*, 125601.
- (32) Pham-Huu, C.; Keller, N.; Charbonniere, L. J.; Ziessle, R.; Ledoux, M. J. *Chem. Comm.* **2000**, 1871.
- (33) Tessonnier, J. P.; Pesant, L.; Ehret, G.; Ledoux, M. J.; Pham-Huu, C. *Appl. Catal. A* **2005**, *288*, 203.
- (34) Yan, W. F.; Brown, S.; Pan, Z. W.; Mahurin, S. M.; Overbury, S. H.; Dai, S. *Angew. Chem. Int. Ed.* **2006**, *45*, 3614.
- (35) Ma, Z.; Yin, H. F.; Overbury, S. H.; Dai, S. *Catal. Lett.* **2008**, *126*, 20.
- (36) Ma, Z.; Zaera, F. *Encyclopedia of Inorganic Chemistry (King, R. B. Ed.)*; 2nd ed.; John Wiley & Sons: New York, 2005.
- (37) Wang, C. M.; Fan, K. N.; Liu, Z. P. *J. Phys. Chem. C* **2007**, *111*, 13539.
- (38) Bindra, P.; Clouser, S. J.; Yeager, E. J. *Electrochem. Soc.* **1979**, *126*, 1631.

- (39) Ferreira, P. J.; la O', G. J.; Shao-Horn, Y.; Morgan, D.; Makharia, R.; Kocha, S.; Gasteiger, H. A. *J. Electrochem. Soc.* **2005**, *152*, A2256.
- (40) Chen, Z.; Waje, M.; Li, W.; Yan, Y. *Angew. Chem. Int. Ed.* **2007**, *46*, 4060.
- (41) Antolini, E.; Salgado, J. R. C.; Gonzalez, E. R. *J. Power Sour.* **2006**, *160*, 957.
- (42) Joo, J. B.; Kim, P.; Kim, W.; Kim, Y.; Yi, J. *J. Appl. Electrochem.* **2009**, *39*, 135.
- (43) Takasu, Y.; Matsuyama, R.; Konishi, S.; Sugimoto, W.; Murakami, Y. *Electrochem. Solid State Lett.* **2005**, *8*, B34.
- (44) Colon-Mercado, H. R.; Popov, B. N. *J. Power Sour.* **2006**, *155*, 253.
- (45) Colon-Mercado, H. R.; Kim, H.; Popov, B. N. *Electrochem. Comm.* **2004**, *6*, 795.
- (46) Yu, P.; Pemberton, M.; Plasse, P. *J. Power Sour.* **2005**, *144*, 11.
- (47) Koh, S.; Leisch, J.; Toney, M. F.; Strasser, P. *J. Phys. Chem. C* **2007**, *111*, 3744.
- (48) Liu, Z. C.; Yu, C. F.; Rusakova, I. A.; Huang, D. X.; Strasser, P. *Top. Catal.* **2008**, *49*, 241.
- (49) Okada, T.; Ayato, Y.; Satou, H.; Yuasa, M.; Sekine, I. *J. Phys. Chem. B* **2001**, *105*, 6980.
- (50) Samuelson, L.; Liu, W.; Nagarajan, R.; Kumar, J.; Bruno, F. F.; Cholli, A.; Tripathy, S. *Synthetic Metals* **2001**, *119*, 271.
- (51) Ingert, D.; Pileni, M. P. *Adv. Funct. Mater.* **2001**, *11*, 136.
- (52) Dellinger, T. M.; Braun, P. V. *Scr. Mater.* **2001**, *44*, 1893.
- (53) Manziek, L.; Langenmayr, E.; Lamola, A.; Gallagher, M.; Brese, N.; Annan, N. *Chem. Mater.* **1998**, *10*, 3101.
- (54) Hingorani, S.; Shah, D. O.; Multani, M. S. *J. Mater. Res.* **1995**, *10*, 461.
- (55) Antonietti, M.; Grohn, F.; Hartmann, J.; Bronstein, L. *Angew. Chem. Int. Ed.* **1997**, *36*, 2080.
- (56) Forster, S.; Konrad, M. *J. Mater. Chem.* **2003**, *13*, 2671.
- (57) Bronstein, L. H.; Sidorov, S. N.; Valetsky, P. M.; Hartmann, J.; Colfen, H.; Antonietti, M. *Langmuir* **1999**, *15*, 6256.
- (58) Graff, A.; Winterhalter, M.; Meier, W. *Langmuir* **2001**, *17*, 919.

- (59) Nardin, C.; Thoeni, S.; Widmer, J.; Winterhalter, M.; Meier, W. *Chem. Comm.* **2000**, 1433.
- (60) Sangregorio, C.; Wiemann, J. K.; O'Connor, C. J.; Rosenzweig, Z. *J. Appl. Phys.* **1999**, *85*, 5699.
- (61) Balogh, L.; Tomalia, D. A. *J. Am. Chem. Soc.* **1998**, *120*, 7355.
- (62) Esumi, K. *Colloid Chemistry Ii* **2003**, 227, 31.
- (63) Ohmori, M.; Matijevic, E. *J. Colloid Interface Sci.* **1992**, *150*, 594.
- (64) Philipse, A. P.; van Bruggen, M. P. B.; Pathmamanoharan, C. *Langmuir* **1994**, *10*, 92.
- (65) Liz-Marzan, L. M.; Giersig, M.; Mulvaney, P. *Langmuir* **1996**, *12*, 4329.
- (66) Lu, Y.; Yin, Y.; Li, Z. Y.; Xia, Y. *Nano Lett.* **2002**, *2*, 785.
- (67) Arnal, P. M.; Comotti, M.; Schüth, F. *Angew. Chem.* **2006**, *118*, 8404.
- (68) Giersig, M.; Ung, T.; Liz-Marzan, L. M.; Mulvaney, P. *Adv. Mater.* **1997**, *9*, 570.
- (69) Ung, T.; Liz-Marzan, L. M.; Mulvaney, P. *Langmuir* **1998**, *14*, 3740.
- (70) Hah, H. J.; Um, J. I.; Han, S. H.; Koo, S. M. *Chem. Commun.* **2004**, 1012.
- (71) Kim, J. Y.; Yoon, S. B.; J.-S. Yu *Chem. Commun.* **2003**, 790.
- (72) Kim, M.; Sohn, K.; Na, H. B.; Hyeon, T. *Nano Lett.* **2002**, *2*, 1383.
- (73) Ikeda, S.; Ishino, S.; Harada, T.; Okamoto, N.; Sakata, T.; Mori, H.; Kuwabata, S.; Torimoto, T.; Matsumura, M. *Angew. Chem. Int. Ed.* **2006**, *45*, 7063.
- (74) Min, Y. L.; Wan, Y.; Liu, R.; Yu, S. H. *Chin. J. Inorg. Chem.* **2008**, *24*, 1172.
- (75) Zhang, Q.; Wang, W.; Goebel, J.; Yin, Y. *Nano Today* **2009**, *4*, 494.
- (76) Lee, J.; Park, J. C.; Song, H. *Adv. Mater.* **2008**, *20*, 1523.
- (77) Büchel, G.; Unger, K. K.; Matsumoto, A.; Tsutsumi, K. *Adv. Mater.* **1998**, *10*, 1036.
- (78) Tan, B.; Rankin, S. E. *Langmuir* **2005**, *21*, 8180.
- (79) Yin, Y.; Rioux, R. M.; Erdonmez, C. K.; Hughes, S.; Somorjai, G. A.; Alivisatos, A. P. *Science (Washington, DC, U. S.)* **2004**, *304*, 711.
- (80) Kim, S.; Yin, Y.; Alivisatos, A. P.; Somorjai, G. A.; Yates, J. T. *J. Am. Chem. Soc.* **2007**, *129*, 9510.



- (81) Lee, J.; Park, J. C.; Bang, J. U.; Song, H. *Chem. Mater.* **2008**, *20*, 5839.
- (82) Shi, Y. L.; Asefa, T. *Langmuir* **2007**, *23*, 9455.
- (83) Joo, S. H.; Park, J. Y.; Tsung, C.-K.; Yamada, Y.; Yang, P.; Somorjai, G. A. *Nature Mater.* **2009**, *8*, 126.
- (84) Zhang, T.; Ge, J.; Hu, Y.; Zhang, Q.; Aloni, S.; Yin, Y. *Angew. Chem. Int. Ed.* **2008**, *47*, 5806.
- (85) Hu, Y.; Ge, J.; Sun, Y.; Zhang, T.; Yin, Y. *Nano Lett.* **2007**, *7*, 1832
- (86) Zhang, Q.; Ge, J.; Goebel, J.; Hu, Y.; Lu, Z.; Yin, Y. *Nano Res.* **2009**, *2*, 583.
- (87) Zhang, T.; Zhang, Q.; Ge, J.; Goebel, J.; Sun, M. W.; Yan, Y.; Liu, Y.; Chang, C.; Guo, J.; Yin, Y. *J. Phys. Chem. C* **2009**, *113*, 3168.
- (88) Ge, J.; Zhang, Q.; Zhang, T.; Yin, Y. *Angew. Chem. Int. Ed.* **2008**, *47*, 8924.
- (89) Zhang, Q.; Ge, J.; Goebel, J.; Hu, Y.; Sun, Y.; Yin, Y. *Adv. Mater.* **2010**, *22*, 1905.
- (90) Loaiza, A.; Xu, M. D.; Zaera, F. *J. Catal.* **1996**, *159*, 127.
- (91) Aryafar, M.; Zaera, F. *Catal. Lett.* **1997**, *48*, 173.
- (92) Wilson, J.; Guo, H.; Morales, R.; Podgornov, E.; Lee, I.; Zaera, F. *Phys. Chem. Chem. Phys.* **2007**, *9*, 3830.
- (93) Jia, C. J.; Sun, L. D.; Yan, Z. G.; You, L. P.; Luo, F.; Han, X. D.; Pang, Y. C.; Zhang, Z.; Yan, C. H. *Angew. Chem. Int. Ed.* **2005**, *44*, 4328.
- (94) Lu, J.; Chen, D. R.; Jiao, X. L. *J. Colloid Interface Sci.* **2006**, *303*, 437.
- (95) Mao, B. D.; Kang, Z. H.; Wang, E. B.; Tian, C. G.; Zhang, Z. M.; Wang, C. L.; Song, Y. L.; Li, M. Y. *J. Solid State Chem.* **2007**, *180*, 489.
- (96) Li, L. L.; Chu, Y.; Liu, Y.; Dong, L. H. *J. Phys. Chem. C* **2007**, *111*, 2123.
- (97) Zeng, S. Y.; Tang, K. B.; Li, T. W.; Liang, Z. H.; Wang, D.; Wang, Y. K.; Zhou, W. W. *J. Phys. Chem. C* **2007**, *111*, 10217.
- (98) Jia, B. P.; Gao, L. *J. Phys. Chem. C* **2008**, *112*, 666.
- (99) Hench, L. L.; West, J. K. *Chem. Rev.* **1990**, *90*, 33.
- (100) Zhang, Q.; Lee, I.; Ge, J.; Zaera, F.; Yin, Y. *Adv. Funct. Mater.* **2010**, *20*, 2201.
- (101) Cohen Stuart, M. A.; Fleer, G. J.; Bijsterbosch, B. H. *J. Colloid Interface Sci.* **1982**, *90*, 321.

- (102) Nelson, A.; Jack, K. S.; Cosgrove, T.; Kozak, D. *Langmuir* **2002**, *18*, 2750.
- (103) Gun'ko, V. M.; Zarko, V. I.; Voronin, E. F.; Goncharuk, E. V.; Andriyko, L. S.; Guzenko, N. V.; Nosach, L. V.; Janusz, W. *J. Colloid Interface Sci.* **2006**, *300*, 20.
- (104) Cohen Stuart, M. A.; Fleer, G. J.; Bijsterbosch, B. H. *J. Colloid Interface Sci.* **1982**, *90*, 310.
- (105) Saegusa, T. *Pure Appl. Chem.* **1995**, *67*, 1965.
- (106) Zhang, Q.; Zhang, T.; Ge, J.; Yin, Y. *Nano Lett.* **2008**, *8*, 2867.
- (107) Grzelczak, M.; Correa-Duarte, Miguel A.; Liz-Marzán, Luis M. *Small* **2006**, *2*, 1174.
- (108) Liu, S.; Wong, Y.; Wang, Y.; Wang, D.; Han, M. Y. *Adv. Funct. Mater.* **2007**, *17*, 3147.
- (109) Arnal, P. M.; Comotti, M.; Schüth, F. *Angew. Chem. Int. Ed.* **2006**, *45*, 8224.
- (110) Panigrahi, S.; Basu, S.; Praharaj, S.; Pande, S.; Jana, S.; Pal, A.; Ghosh, S. K.; Pal, T. *J. Phys. Chem. C* **2007**, *111*, 4596.
- (111) Grzelczak, M.; Correa-Duarte, M. A.; Liz-Marzán, L. M. *Small* **2006**, *2*, 1174.
- (112) Comotti, M.; Della, P. C.; Matarrese, R.; Rossi, M. *Angew. Chem., Int. Ed.* **2004**, *43*, 5812.
- (113) Valdés-Solís, T.; Valle-Vigón, P.; Sevilla, M.; Fuertes, A. B. *J. Catal.* **2007**, *251*, 239.
- (114) Ge, J.; Huynh, T.; Hu, Y.; Yin, Y. *Nano Lett.* **2008**, *8*, 931.
- (115) Stevens, P. D.; Li, G.; Fan, J.; Yen, M.; Gao, Y. *Chem. Commun.* **2005**, 4435.
- (116) Wang, L.; Yang, Z.; Gao, J.; Xu, K.; Gu, H.; Zhang, B.; Zhang, X.; Xu, B. *J. Am. Chem. Soc.* **2006**, *128*, 13358.
- (117) Yi, D. K.; Lee, S. S.; Ying, J. Y. *Chem. Mater.* **2006**, *18*, 2459.
- (118) Jeong, U.; Teng, X.; Wang, Y.; Yang, H.; Xia, Y. *Adv. Mater.* **2007**, *19*, 33.
- (119) Xu, R.; Xie, T.; Zhao, Y.; Li, Y. *Nanotech.* **2007**, *18*, 055602.
- (120) Fletcher, D. *IEEE Trans. Magn.* **1991**, *27*, 3655.

- (121) Yavuz, C. T.; Mayo, J. T.; Yu, W. W.; Prakash, A.; Falkner, J. C.; Yean, S.; Cong, L.; Shipley, H. J.; Kan, A.; Tomson, M.; Natelson, D.; Colvin, V. L. *Science* **2006**, *314*, 964.
- (122) Ge, J.; Hu, Y.; Biasini, M.; Beyermann, W.; Yin, Y. *Angew. Chem. Int. Ed.* **2007**, *46*, 4342.
- (123) Ge, J.; Hu, Y.; Yin, Y. *Angew. Chem. Int. Ed.* **2007**, *46*, 7428.
- (124) Zhang, Q.; Ge, J.; Goebel, J.; Hu, Y.; Sun, Y.; Yin, Y. *Adv. Mater. (Weinheim, Ger.)* **2010**, *22*, 1905.
- (125) Zaera, F. *Int. Rev. Phys. Chem.* **2002**, *21*, 433.
- (126) Tiznado, H.; Fuentes, S.; Zaera, F. *Langmuir* **2004**, *20*, 10490.
- (127) Lee, I.; Zaera, F. *J. Am. Chem. Soc.* **2005**, *127*, 12174.
- (128) Brandt, B.; Ludwig, W.; Fischer, J. H.; Libuda, J.; Zaera, F.; Schauermaun, S. *J. Catal.* **2009**, *265*, 191.
- (129) Lee, I.; Zaera, F. *J. Catal.* **2010**, *269*, 359.
- (130) Albiter, M. A.; Zaera, F. *Appl. Catal. A* **2010**, submitted.
- (131) Lee, I.; Zhang, Q.; Ge, J.; Yin, Y.; Zaera, F. *Nano Res.* **2011**, *4*, 115.
- (132) Day, V. W.; Eberspacher, T. A.; Frey, M. H.; Klemperer, W. G.; Liang, S.; Payne, D. A. *Chem. Mater.* **1996**, *8*, 330.
- (133) Ksapabutr, B.; Gulari, E.; Wongkasemjit, S. *Mater. Chem. Phys.* **2004**, *83*, 34.
- (134) Phonthammachaia, N.; Rumruangwonga, M.; Gularib, E.; Jamiesonc, A. M.; Jitkarnkaa, S.; Wongkasemjita, S. *Colloid Surf. A* **2004**, *247*, 61.
- (135) Yacaman, M. J.; Ascencio, J. A.; Liu, H. B.; Gardea-Torresdey, J. *J. Vac. Sci. Tech. B* **2001**, *19*, 1091.
- (136) Qi, W. H. *Solid State Comm.* **2006**, *137*, 536.
- (137) Barnard, A. S.; Zapol, P. *J. Chem. Phys.* **2004**, *121*, 4276.
- (138) Yu, R.; Song, H.; Zhang, X. F.; Yang, P. *J. Phys. Chem. B* **2005**, *109*, 6940.

## Chapter 4

### Engineering TiO<sub>2</sub> Nanomaterials for Photocatalytic Applications

#### 4.1 Introduction

A grand challenge facing the research community in the area of solar energy harvesting is to develop materials capable of transforming solar photons efficiently into chemical or electrical work.<sup>1,2</sup> Since the discovery of its photocatalytic activity under UV light, titanium dioxide (TiO<sub>2</sub>) based materials have become widely studied as photocatalysts in applications such as water splitting and purification.<sup>3</sup> As we mentioned in Chapter 1, much effort has been devoted to prepare TiO<sub>2</sub>-base photocatalysts with high efficiency and low cost. It has been realized that higher photocatalytic activity can be achieved by improving many aspects of TiO<sub>2</sub>, including crystal phase, specific surface area, surface properties and crystallinity. From a crystalline phase point of view, although rutile phase titania has a lower band-gap energy, well-crystallized anatase is superior due to its intrinsic advantageous properties, including a higher reduction potential and a lower recombination rate of electron-hole pairs.<sup>4-6</sup> A high surface area is also critically important to increase the number density of red-ox reaction sites. However, direct use of TiO<sub>2</sub> nanocrystals synthesized through colloidal routes is often problematic due to the occupancy of the active sites by capping ligands

which are required for maintaining the colloidal stability.<sup>7-9</sup> One practical approach to producing high surface area titania is the creation of mesoscale porosity in the TiO<sub>2</sub> materials.<sup>10,11</sup> As diffusion is often a problem that limits the overall performance of bulk material during catalysis, it can be improved by making a catalyst in the form of mesoporous colloidal particles instead of a bulk powder. Additional improvement in mass transfer can be obtained by the removal of the core portion of a colloidal particle to produce a porous hollow shell that is expected to further reduce diffusion resistance and improve accessibility of the reactant to the active surface.<sup>12-17</sup>

However, there are great challenges in preparing mesoporous anatase TiO<sub>2</sub> which possesses both large surface area and high crystallinity. Although it has been possible to produce TiO<sub>2</sub> mesoporous materials with large surface area by carrying out the sol-gel process against surfactant templates, a heat treatment step is usually required to convert the products into crystalline anatase phase, which causes collapse of mesopores and seriously decreases the surface area. The typically reported value of BET surface area for mesoporous TiO<sub>2</sub> materials is around 100 m<sup>2</sup>/g,<sup>18,19</sup> which is much smaller than their amorphous counterpart. Additionally, due to the uncontrollable pore collapse during the heat treatment process, it is also difficult to control the pore size distribution, which is important in some catalysis applications.

As pristine TiO<sub>2</sub> only absorbs UV light, much effort has been devoted to developing visible-light-active TiO<sub>2</sub> photocatalysts that can make use of both UV and visible radiation. Many strategies, including metal ion<sup>20</sup> and non-metal doping<sup>21-25</sup>, have been proposed to extend the absorption of TiO<sub>2</sub> to the visible spectrum, but so far new materials have typically suffered from low doping concentration and/or low stability against photo-corrosion.<sup>24,26-28</sup> Noble-metal nanoparticles such as Au and Ag have also been used to enhance the activity of photocatalysts in visible light due to their plasmonic properties.<sup>29-31</sup> In any case, an improved absorption of photons may not necessarily guarantee significantly better photocatalytic performance because the efficiency of a photocatalyst is also determined by charge separation and transport. Due to the fast recombination of e<sup>-</sup>-h<sup>+</sup> pairs, most excited charges recombine and quench before reaching the surface. From this point of view, small grain size and high crystallinity would be desirable for enhancing charge separation efficiency; that would result in a reduced migration distance of charges and, consequently, in a lower recombination rate.<sup>32,33</sup> Additionally, metal decoration has also been shown to enhance charge separation in TiO<sub>2</sub> photocatalysts by serving as electron reservoirs.<sup>34</sup> It is therefore expected that a composite of small doped TiO<sub>2</sub> nanocrystals decorated with metal nanoparticles, by combining all the good features discussed above, may be a powerful photocatalyst. However, due to the incompatibility between the synthesis, doping, and decoration

procedures, the production of such nanocomposites has remained a great challenge. For example, although crystalline TiO<sub>2</sub> nanoparticles can be produced via colloidal synthesis in a hot organic solvent,<sup>35-37</sup> their nonmetal doping and metal nanoparticle decoration cannot be easily achieved.<sup>38</sup> Alternatively, TiO<sub>2</sub> particles can be produced from their sol-gel derived precursors, but their crystallization and subsequent nonmetal doping requires high temperature calcination, which typically causes sintering of both TiO<sub>2</sub> and metal nanoparticles.<sup>39</sup>

In this Chapter, we will focus on the engineering of TiO<sub>2</sub>-based nanomaterials for photocatalytic applications. In **Section 4.3**, we report a general strategy for the fabrication of mesoporous TiO<sub>2</sub> photocatalysts based on the self-assembly of TiO<sub>2</sub> nanocrystals. By optimizing the synthesis condition, i.e., calcination temperature, TiO<sub>2</sub> clusters with good photocatalytic activity has been obtained. In **Section 4.4**, we present the design and synthesis of a highly efficient, stable, and cost-effective TiO<sub>2</sub>-based photocatalyst with the desired properties by combining simple sol-gel and calcination processes. The new catalyst has a sandwich structure that comprises a SiO<sub>2</sub> core, a layer of gold nanoparticles (AuNPs), and a doped-TiO<sub>2</sub> nanocrystalline shell. The new photocatalysts shows excellent performance in degradation reactions of a number of organic compounds under UV, visible light, and direct sunlight. Finally, we conclude with a short summary in **Section 4.5**.

## 4.2 Materials and Methods

**Materials** Trioctylphosphine oxide (TOPO), sodium dodecyl sulfate (SDS), ammonium hydroxide solution (~28% NH<sub>3</sub> in water), tetraethyl orthosilicate (TEOS, 98%), 3-Aminopropyl-triethoxysilane (APTES, 99%), 2, 4-dichlorophenol (2, 4-DCP, 99%), and Rhodamine B (RhB, 99%) were purchased from Aldrich Chemical Co. Hydrogen tetrachloroaurate trihydrate (99.9+%), sodium citrate tribasic dihydrate (99%), and hydroxypropyl cellulose (HPC, Mw = 80,000) were obtained from Sigma-Aldrich. Tetrabutyl orthotitanate (TBOT) and titanium tetrachloride (TiCl<sub>4</sub>) were obtained from Fluka. Ethanol (denatured), toluene, sodium hydroxide, cyclohexane, acetone, 2-propanol (99.9%), commercial anatase TiO<sub>2</sub> powder and P25 aeroxide were obtained from Fisher Scientific. Absolute ethyl alcohol was purchased from Gold Shield Chemical. All chemicals were directly used as received without further treatment.

**Synthesis of TiO<sub>2</sub> nanocrystals** TiO<sub>2</sub> nanocrystals were prepared by a nonhydrolytic solution-based reaction.<sup>40</sup> Typically, TOPO (5 g) was heated at 150 °C for 5 minutes in vacuum to remove the low boiling point materials. After increasing the solution temperature to 200 °C under N<sub>2</sub> atmosphere, TBOT (1.4 mL) was injected into the hot solution. The resulting mixture was then heated up to 320 °C, followed by a rapid addition of 0.55 mL of TiCl<sub>4</sub>. The solution remained at 320 °C for 20 minutes to ensure the complete reaction. After cooling the system down to 80 °C, 10 mL of acetone was



added to yield a white precipitate, which was isolated by centrifugation and subsequently washed with a toluene/acetone mixture to remove extra surfactant. The resulting powder was re-dispersed in 10 mL of cyclohexane.

***Self-assembly of nanocrystals into clusters*** The clusters were formed by assembling nanocrystals in emulsion oil droplets and subsequent evaporating the low-boiling-point solvent (the oil phase). In a typical process, 1 mL of cyclohexane solution of nanocrystals was mixed with an aqueous solution of sodium dodecyl sulfate (SDS) (56 mg in 10 mL H<sub>2</sub>O) under sonication for 5 minutes. The mixture was then heated up to 70-72 °C in a water bath for 4 hours. A clear nanoparticle solution was obtained by evaporating cyclohexane. After cooled down to room temperature, the final products were washed with water for three times and re-dispersed in 3 mL of distilled water.

***Surface modification of the clusters*** TiO<sub>2</sub> nanocrystal clusters were coated with a layer of SiO<sub>2</sub> by using a modified Stöber process.<sup>41</sup> Typically, the above aqueous solution of TiO<sub>2</sub> clusters (3 mL) was first mixed with ethanol (20 mL) and ammonium hydroxide (1 mL, 28%) aqueous solution. Then TEOS (0.1 mL) was injected into the solution and reacted for 20 min under vigorous stirring. The core/shell colloids were collected by centrifugation and washed with ethanol three times. After drying under vacuum overnight, the precipitate was heated to the desired temperature at a rate of 1 °C/min and stayed for 1 hour in air to remove organic agents. In the cases where N-doping was

needed, the  $\text{TiO}_2@\text{SiO}_2$  core-shell particles were heated up under a  $\text{NH}_3/\text{Ar}$  flow in a Linderberg/Blue M tube furnace to the desired temperature at a rate of  $1\text{ }^\circ\text{C}/\text{min}$  and stayed for another hour to ensure the successful nitrogen doping and removal of organic compounds. Then the calcined particles were dispersed in aqueous NaOH solution (5 ml, 0.5 M) for 3~4 hours under stirring to dissolve the silica shell. The particles were collected by centrifugation and washed with distilled water for three times.

***Synthesis and modification of  $\text{SiO}_2$  spheres*** In a typical synthesis, 1 mL of TEOS was injected into a mixture of 4 mL of deionized  $\text{H}_2\text{O}$ , 1 mL of  $\text{NH}_3\cdot\text{H}_2\text{O}$  and 20 mL of isopropanol at room temperature under magnetic stirring. After reacting for 4 hours, the colloidal spheres were collected by centrifugation, re-dispersed in 8 mL of ethanol. After washing twice with ethanol by centrifugation and redispersion, the particles were transferred to a mixture of isopropanol (20 mL) and APTES (50  $\mu\text{L}$ ) and heated to  $80\text{ }^\circ\text{C}$  for 2 hours to functionalize the silica surface with  $-\text{NH}_2$  groups. The surface modified particles were washed with ethanol and dispersed in deionized water (8 mL).

***Synthesis of  $\text{SiO}_2/\text{Au}/\text{TiO}_2$***  In a separate reaction, Au nanoparticles were synthesized using the Turkevich method (Turkevich et al., *Discuss. Faraday Soc.* **1951**, 11, 55). Briefly, a solution of hydrogen tetrachloroaurate trihydrate was prepared in water and heated to reflux with magnetic stirring, followed immediately by addition of 1 mL of 3 wt% freshly prepared trisodium citrate-water solution, which initiated the reduction of the

hydrogen tetrachloroaurate trihydrate. The aurate-citrate solution was allowed to reflux for approximately 30 min. or until completion of the redox reaction as indicated by a change in the solution color from faint yellow to dark red. This method produces a stable, deep-red dispersion of gold particles with an average diameter of around 10 nm. The SiO<sub>2</sub>/Au particles were prepared by mixing a certain amount of the Au solution with modified SiO<sub>2</sub> spheres under sonication. After that, the particles were centrifuged, dispersed in H<sub>2</sub>O and stirred with hydroxypropyl cellulose (HPC) overnight. The sample was then centrifuged and washed twice with ethanol. The outer layer of TiO<sub>2</sub> was prepared using a method developed by Lee et al (Lee, J. W. et al *Microporous and Mesoporous Materials* **2008**, 116, 561.). Typically, the above SiO<sub>2</sub>/Au aqueous solution was mixed with 0.06 mL of distilled water, and 25 mL of absolute ethyl alcohol under vigorous magnetic stirring. An appropriate amount of tetrabutyl orthotitanate previously dissolved in 5 mL of ethanol was introduced drop by drop, followed by refluxing at 85 °C for 90 min. The final products were washed with ethanol several times, then dried in vacuum for 4 h and calcined in air at desired temperature.

**Characterization** A Tecnai T12 TEM was used to characterize the morphology of the colloids in each step. The crystalline structures of the samples were evaluated by X-ray diffraction (XRD) analyses, carried out on a Bruker D8 Advance Diffractometer with Cu K $\alpha$  radiation ( $\lambda = 1.5418 \text{ \AA}$ ). A Philips ESEM XL30 SEM equipped was used to

characterize the morphology of the as-obtained product. The XPS data were collected in an ultrahigh vacuum chamber equipped with an Al K $\alpha$  X-ray excitation source and a Leybold EA11 electron energy analyzer with multichannel detection. A constant band pass energy of 100.8 eV was used, corresponding to a spectral resolution of  $\approx 2.0$  eV. The porosity of the products was measured by the nitrogen adsorption–desorption isotherm and BJH methods on a Micromeritics ASAP 2020M system. UV/Vis-NIR diffuse reflectance spectra were measured on a Shimadzu UV 3101PC spectrophotometer. A probe-type Ocean Optics HR2000CG-UV-NIR spectrometer was used to measure the UV-Vis absorption spectra of the solution to monitor the concentration of RhB at different time intervals.

***Photocatalytic activity measurement*** Photocatalytic reactions for degradation of Rhodamine B (RhB) were carried out in a 100 mL beaker, containing 50 mL of reaction slurry. The aqueous slurry, prepared with catalysts and  $1.0 \times 10^{-5}$  M RhB was stirred in the dark for 30 min to ensure that the RhB was adsorbed to saturation on the catalysts. For UV irradiation, a 15 W UV lamp (254 nm, XX-15G, USA), 6 cm above the reaction slurry, was used as the UV radiation source. The concentration of titania was about 200 mg/L for all the runs. For visible light irradiation, a 150 W tungsten lamp was used as the light source, and a cutoff filter was used to block the UV light ( $< 400$  nm). For the natural sunlight reaction, the reaction flasks were exposed to natural sunlight directly.

### **4.3 Self-Assembled TiO<sub>2</sub> Nanocrystal Cluster and Its Photocatalytic Applications**

Recently, we and other groups reported a general strategy for the fabrication of novel porous nanostructured materials based on the self-assembly of nanocrystals.<sup>42-44</sup> We have demonstrated that the as-prepared mesoporous nanocrystal clusters could be used for selective enrichment of peptides and proteins from complex biological samples.<sup>44-46</sup> From the perspective of photocatalysis, there are also several unique features about these materials, including clean surface, high crystallinity, small grain size and large surface area even after high temperature treatment, good water dispersity, and controllable pore size distribution by simply tuning the initial nanocrystal size and shape. Herein, we report their use as highly efficient and stable photocatalysts by taking advantage of these unique features. Hydrophobic anatase TiO<sub>2</sub> nanocrystals were synthesized first through a nonhydrolytic solution-based reaction. An emulsion-based bottom-up assembly approach was then used to self-assemble the colloidal nanocrystals to densely packed clusters by evaporating the low-boiling-point oil phase. After coating with a layer of silica shell, the as-obtained clusters were calcined at high temperature to improve its crystalline and remove the organic ligands. Further etching of SiO<sub>2</sub> shell through alkaline solution can remove the outer silica layer and grant the TiO<sub>2</sub> cluster a hydrophilic surface which allows better water accessibility to the pores. Thanks to the calcination, the mesoporous TiO<sub>2</sub> cluster can keep their porous structure after the etching

step. By optimizing the synthesis condition, i.e., calcination temperature, TiO<sub>2</sub> clusters with good photocatalytic activity has been obtained. It is believed that the enhanced photocatalytic performance comes from the unique cluster structure and the post-treatment of silica coating and etching process that offers small grains of TiO<sub>2</sub> cluster (~5 nm), large surface area, and hydrophilic surface. N-doping process was further done successfully to make the clusters be visible light active. The degradation of organic pollutants under UV, visible light and direct sunshine was carried out using rhodamine B (RhB) as a model compound to explore the catalytic activities of the mesoporous photocatalysts.

The synthesis of TiO<sub>2</sub> nanocrystals involved a solution phase nonhydrolytic reaction between the two precursors of TBOT and TiCl<sub>4</sub>, with TOPO as both the solvent and surfactant.<sup>40</sup> Figure 4.1a shows a TEM image of a typical sample of TiO<sub>2</sub> nanocrystals with an average diameter of 5 nm. The hydrophobic nanocrystals were dissolved in cyclohexane and then dispersed in water to form an oil-in-water emulsion with SDS acting as the surfactant. Upon evaporation of the low-boiling-point solvent (cyclohexane in this case), the nanocrystals confined in the oil droplets self-assembled into microspheres, with size controllable by adjusting the nanocrystal concentration or the extent of ultra-sonication during emulsification (Figure 4.1b).

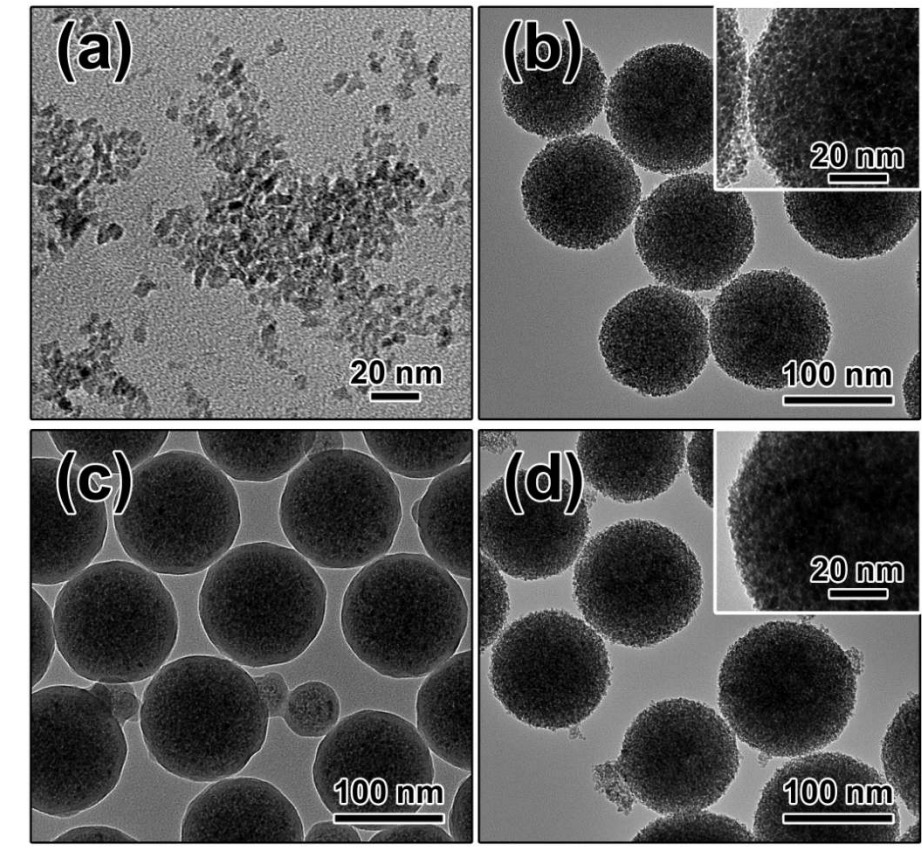


**Figure 4.1** TEM images showing the preparation process of TiO<sub>2</sub> nanocrystal clusters: (a) TiO<sub>2</sub> nanoparticles; (b) self-assembled TiO<sub>2</sub> clusters; (c) SiO<sub>2</sub> coated TiO<sub>2</sub> clusters; (d) TiO<sub>2</sub> clusters after calcination of (c) at 400 °C for 1 hour and subsequently removal SiO<sub>2</sub> shell by etching in NaOH. The insets in b and d are higher magnification images of nanocrystal clusters. Reproduced with permission from Ref. 33. Copyright © 2011 Tsinghua University Press and Springer-Verlag Berlin Heidelberg.

Generally, the lower concentration of TiO<sub>2</sub> nanocrystals and the longer sonication time, the smaller size of the as-obtained TiO<sub>2</sub> clusters. The inset in Figure 4.1b shows an enlarged TEM image of a single cluster, from which one can clearly appreciate the porous nature of the structure. The clusters were then successfully coated with a silica layer through a modified sol-gel process, as confirmed by the TEM measurement (Figure 4.1c). The thickness of the coated silica layer could be easily controlled by adjusting the amount of TEOS. Calcination of the obtained TiO<sub>2</sub>/SiO<sub>2</sub> core-shell structure in air removes the organic ligands and improves the crystallinity as well as the mechanical stability. Finally, the silica layer was etched away to re-expose TiO<sub>2</sub> clusters by using a dilute solution of NaOH. The clusters can still keep their spherical shape and porous nature after the calcination and etching treatments (Figure 4.1d), suggesting good mechanical stability which is preferred in photocatalytic applications.

The crystallographic phases of the as-prepared catalysts were studied by XRD patterns. As shown in Figure 4.2, all reflection peaks of the TiO<sub>2</sub> clusters could be indexed as pure anatase structure with cell parameters  $a = b = 3.78 \text{ \AA}$ ,  $c = 9.51 \text{ \AA}$ , which are in good agreement with the literature value (JCPDS card No. 21-1272). The broad peaks of the product indicate that the obtained clusters are composed of small nanocrystals, which is consistent with our TEM observation in Figure 4.1.



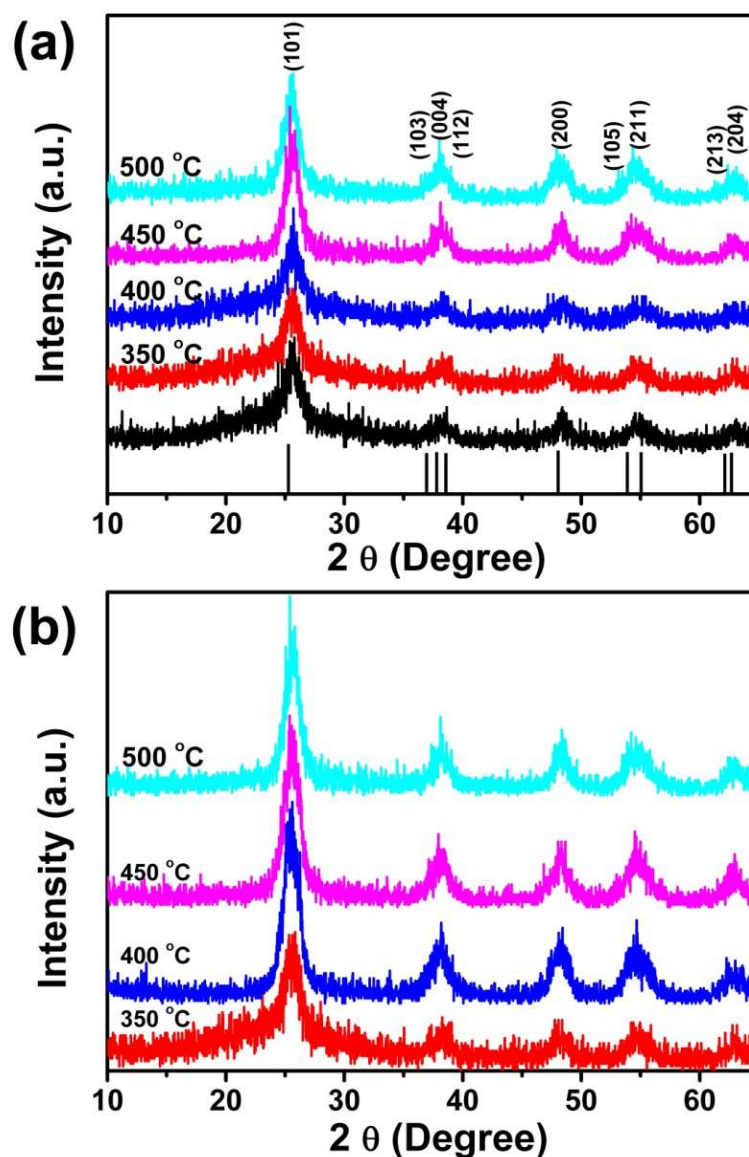


**Figure 4.2** (a) XRD patterns of self-assembled  $\text{TiO}_2$  clusters after calcination at different temperatures: 350 °C (TC350), 400 °C (TC400), 450 °C (TC450), and 500 °C (TC500). The black curve was measured from a sample prepared without calcination. All samples were prepared by sequential steps of self-assembly in emulsion droplets, silica coating, calcination, and silica etching. (b) XRD patterns of self-assembled  $\text{TiO}_2$  clusters calcined at different temperatures without silica protection. Reproduced with permission from Ref. 33. Copyright © 2011 Tsinghua University Press and Springer-Verlag Berlin Heidelberg.

For all the samples, calcination at higher temperatures did not change the crystallographic phase of the as-prepared clusters, while the grain size of such clusters slightly increased during the calcination process. The Scherrer formula was used to estimate the average grain sizes of the TiO<sub>2</sub> clusters:

$$D = \frac{0.89\lambda}{\beta \cos \theta} \quad (1)$$

where  $D$  is the diameter of grain size,  $\lambda$  the X-ray wavelength in nanometers ( $\lambda = 0.15418$  nm in this case),  $\beta$  the width of the XRD peak at the half-peak height in radians, and  $\theta$  the angle between the incident and diffracted beams in degrees. Figure 4.2a shows the XRD patterns of TiO<sub>2</sub> clusters after silica coating, calcination at different temperatures, and then silica etching. It is found that the grain size of the TiO<sub>2</sub> nanocrystals gradually increased from initial value of 4.8 nm to about 5.5 nm for the sample calcined at 500 °C for 1 hour. In contrast, as shown in Figure 4.2b, the TiO<sub>2</sub> nanocrystal clusters without silica protection during calcination drastically increased their grain sizes, which became 8.4 nm at 500 °C, clearly suggesting a protecting effect of the silica shell. The limited size increase of the nanocrystals in silica-protected clusters during calcination is beneficial for retaining them in the anatase phase even after high-temperature treatments, as the grain size is still well below the critical value of 14 nm at which the anatase phase transforms to the rutile phase.<sup>47,48</sup>

As the surface-to-volume ratio of catalysts is critical for their overall catalytic efficiency, the surface area and porosity of the TiO<sub>2</sub> clusters after calcination at different temperatures were investigated by using nitrogen adsorption-desorption isotherms. Figure 4.3a shows a representative nitrogen adsorption/desorption isotherms and the corresponding pore size distribution of the TiO<sub>2</sub> clusters calcined at 400 °C (TC400). The average pore diameter, as determined by using the Barrett–Joyner–Halenda (BJH) method from the desorption branch of the isotherm (inset of Figure 4.3), increases slightly from 2.1 nm to 2.3 nm and 2.4 nm after calcination at 350, 400, and 500 °C. The BET surface areas also changed slightly, from 277 m<sup>2</sup>/g for sample treated at 350 °C to 268 m<sup>2</sup>/g at 400 °C and 253 m<sup>2</sup>/g at 500 °C. Both changes could be ascribed to the gradual increase in the grain size during calcination. We note that silica coating can help to maintain the mesoporous structure and therefore the large surface area of the clusters. As shown in Figure 4.3b, although the clusters without silica coating can still keep their mesoporous structure after calcination at 400 °C for 1 hour, their surface area drastically decreased to 137 m<sup>2</sup>/g, which is consistent with the significant grain growth of the unprotected samples during calcination.

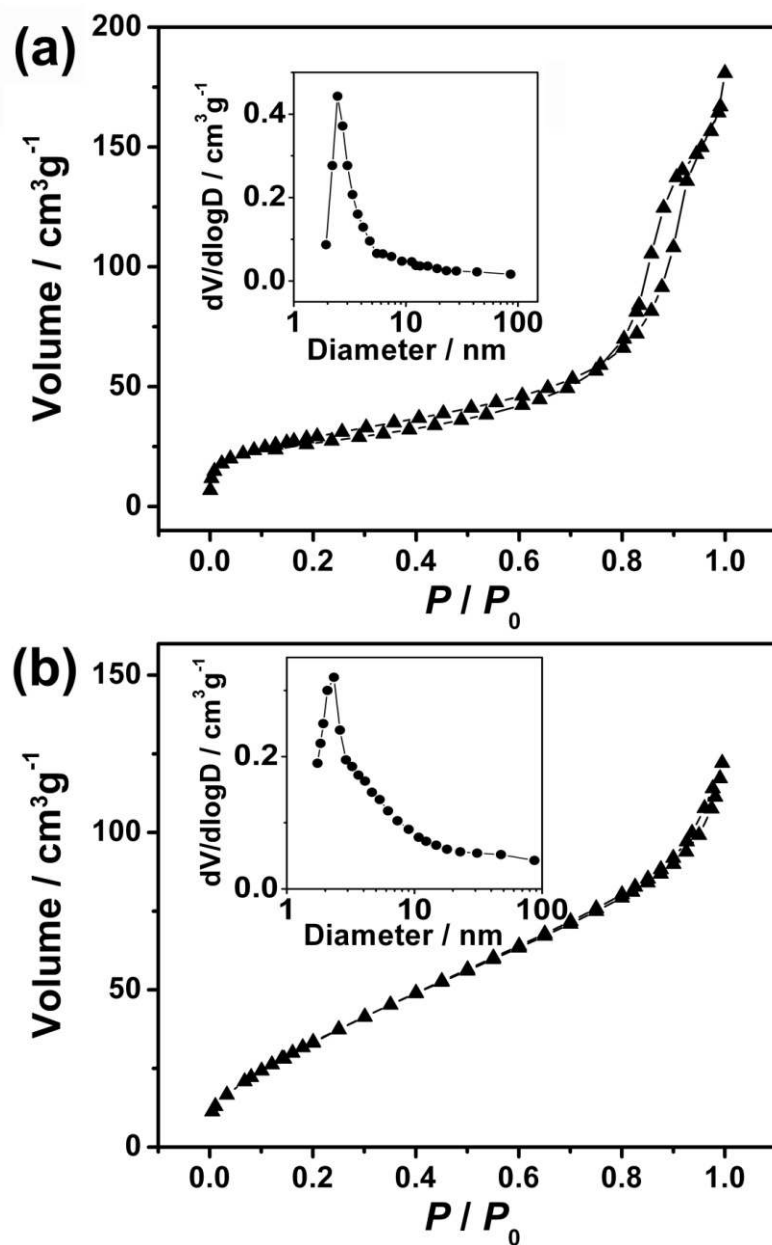


**Figure 4.3** Nitrogen adsorption-desorption isotherms of TiO<sub>2</sub> clusters after calcination at 400 °C: (a) a layer of silica was coated on the clusters before calcination, and removed afterwards; (b) clusters were calcined without the silica treatment. The insets show the BJH pore size distribution of the corresponding samples. Reproduced with permission from Ref. 33. Copyright © 2011 Tsinghua University Press and Springer-Verlag Berlin Heidelberg.

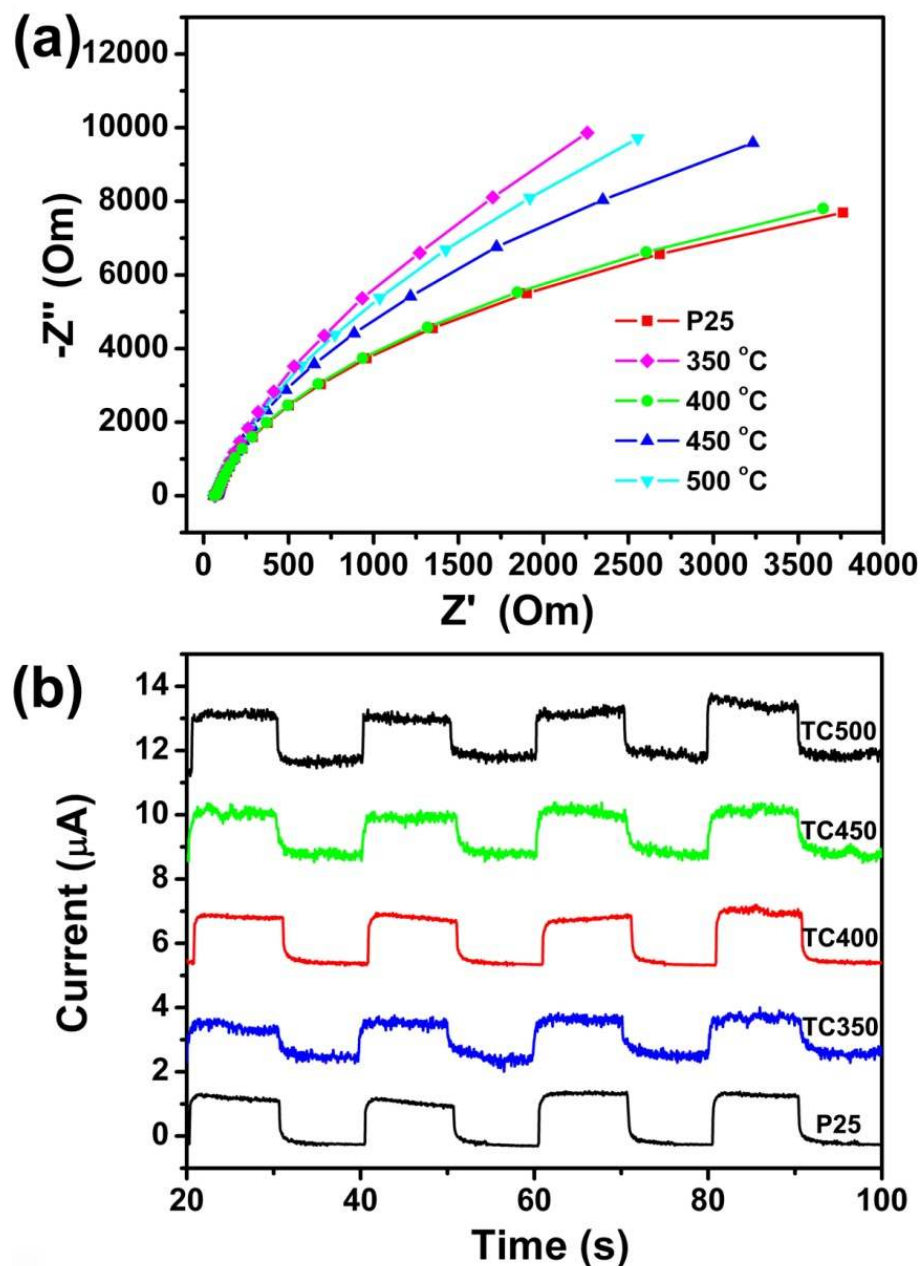


**Figure 4.4** (a) Nyquist plots for each photocatalyst nanoparticle in aqueous solution of RhB under UV light illumination. Symbols and lines indicate the experimental data and fitted curves, respectively. (b) Chronoamperometry study of P25 and TiO<sub>2</sub> clusters calcined at different temperatures. Reproduced with permission from Ref. 33. Copyright © 2011 Tsinghua University Press and Springer-Verlag Berlin Heidelberg.

Electrochemical characterization was carried out to investigate the potential use of the TiO<sub>2</sub> nanocrystal clusters in photocatalysis. Electrochemical impedance spectroscopy (EIS) was performed to characterize electrochemical interfacial reactions, in which the photocatalytic decomposition of RhB was used as the model reaction. A three electrode system was utilized to measure the EIS spectrum by using Ag/AgCl as the reference electrode, Pt wire as the counter electrode, and ITO glass with the deposition of TiO<sub>2</sub> catalysts as the working electrode. RhB and Na<sub>2</sub>SO<sub>4</sub> aqueous solution was used as the electrolyte. Figure 4.4a shows the EIS Nyquist plots of P25 and TiO<sub>2</sub> clusters under UV irradiation. It is well accepted that a smaller arc radius of an EIS Nyquist plot implies a higher efficiency of charge separation. In the five samples, P25 TiO<sub>2</sub> and TC400 show similarly the smallest arc radius, suggesting the highest charge separation efficiency. The relative charge separation efficiency is in the order of TC350<TC500<TC450<TC400.

Chronoamperometry (CA) experiments were used to characterize the photo-generated current density under a potential of 0.8 V and a periodic illumination of UV light. The photo-generated current density is usually regarded as equivalent to photocatalytic activity. As shown in Figure 4.4b, one can clearly notice the photo-generated current for all of the five samples, indicating their active response to the UV irradiation. The shape of such CA curves can be well maintained after many cycles of light illumination,

implying good photocatalytic stability. The current densities measured on P25 and TiO<sub>2</sub> cluster samples are consistent with the EIS measurements, with TC400 still showing the highest value ( $\sim 1.5 \mu\text{A}/\text{cm}^2$ ).

The catalytic activity of the photocatalysts was evaluated by measuring degradation rates of RhB under light irradiation. Figure 4.5a shows typical absorption spectra of an aqueous solution of RhB exposed to UV light for various time periods by using TC400 as the catalyst. The strong absorption peak at 553 nm gradually diminished as the UV irradiation prolonged, and completely disappeared after 30 min, suggesting the complete photo-degradation of the organic dye. The changes in RhB concentration ( $C$ ) over the course of the photocatalytic degradation reaction by using different photocatalysts are summarized in Figure 4.5b. The photocatalysts were first illuminated by UV light for 1 hour to rule out the influence of organic residue in cluster structure. To compare the photocatalytic activities, the total amount of TiO<sub>2</sub> was kept the same. The calcination temperature appears to be a critical parameter in determining the photocatalytic activity. The adsorption of RhB decreases for TiO<sub>2</sub> clusters treated at higher temperatures, while P25 shows the lowest adsorption due to its smallest surface area ( $\sim 50 \text{ m}^2/\text{g}$ ). This is consistent with the BET measurements, with dropping surface area after calcination of the samples at increasing temperatures. However, the photocatalytic activity didn't follow this simple trend. Although it shows the highest adsorption, the photocatalytic

activity of TC350 is the lowest, probably due to the relatively lower crystallinity. TC400 presents the highest photocatalytic activity which is equivalent to that of commercial P25, while TC450 shows similar activity to TC400 under UV irradiation in spite of the lower adsorption ability. Calcination at even higher temperature may lower the efficiency, as evidenced by the performance of TC500. Generally, the higher photocatalytic activity is favored by the larger surface area and the higher crystallinity of the catalyst. As pointed out above, higher calcination temperature could improve the crystallinity by removing the defects in nanocrystals but it also leads to a smaller surface area. It is apparent that calcination at 400 °C is the optimal condition for preparing mesoporous TiO<sub>2</sub> cluster with large surface area and relatively high crystallinity. The overall photocatalytic performance of the TiO<sub>2</sub> clusters is consistent with the results of electrochemical measurements.

We have also studied the effect of the silica coating/removing process on the catalytic performance of the TiO<sub>2</sub> nanocrystal clusters. Compared to the samples with silica treatment, clusters without silica protection during calcination show much lower adsorption of RhB, as shown in Figure 4.5c. During the initial adsorption process, ~30% of RhB could be absorbed by the silica treated clusters, while only 20% of RhB could be absorbed by the clusters without silica treatment. We have pointed out previously that the silica coating and etching processes could effectively enhance the surface charge and



water dispersity of such clusters,<sup>44</sup> which was also confirmed by this experiment. Without silica coating/removing treatment, the calcined TiO<sub>2</sub> clusters would be in the form of large aggregations and could not be well dispersed in water even after 10 min of sonication, while silica treated clusters could be well dispersed in water. Furthermore, as discussed above, silica coating can help to maintain the mesoporous structure and therefore the large surface area of the clusters, which also favors a higher photocatalytic activity.

The porous structure of the TiO<sub>2</sub> nanocrystal clusters allows convenient nitrogen doping at desired temperatures under NH<sub>3</sub>/Ar gas flow. After the nitrogen doping process, the white powder became yellowish, suggesting the successful N-doping, which was further confirmed by measuring the diffuse reflectance UV-Vis spectra. Figure 4.6 shows the UV-Vis spectra of three samples: P25, TiO<sub>2</sub> clusters before and after N-doping (NTC400). Compared with P25 and the un-doped TiO<sub>2</sub> clusters that absorb only UV light, a noticeable shift of absorption edge to the visible region was observed for the N-doped sample. To quantitatively study the influence of N-doping process, the band gap energy change has been studied. As TiO<sub>2</sub> is a crystalline semiconductor of indirect transition, the band gap energy of un-doped and N-doped TiO<sub>2</sub> clusters can be estimated from the following equation:

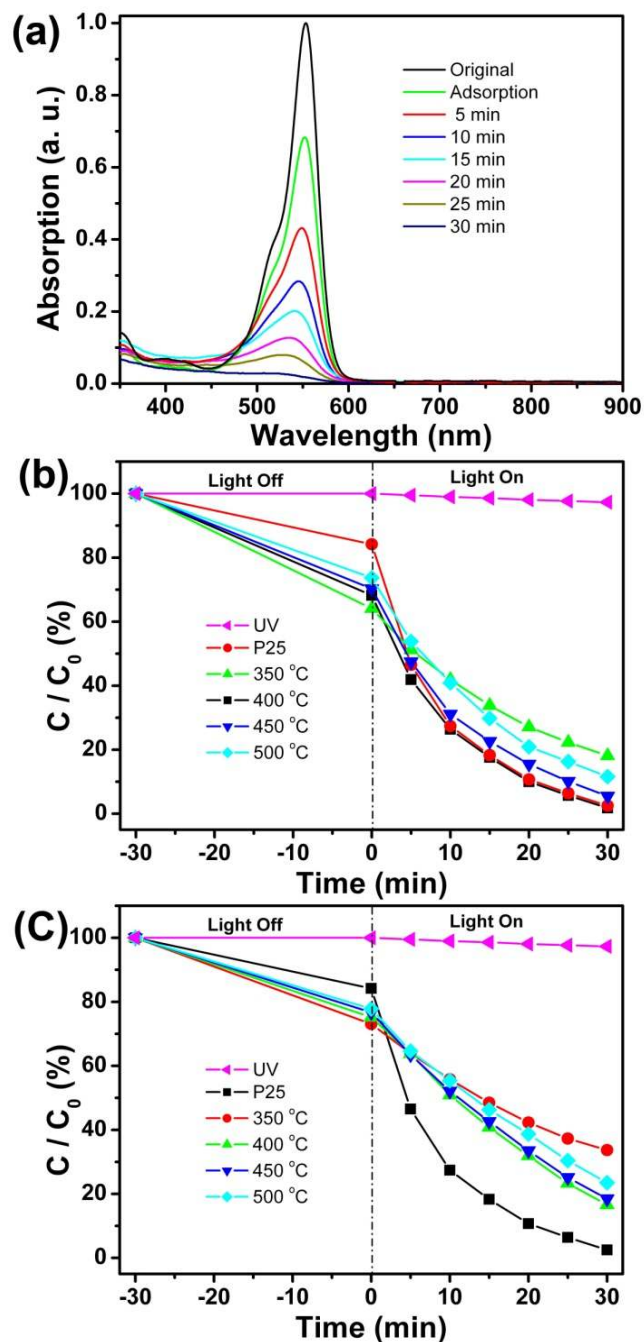


**Figure 4.5** (a) Absorption spectra showing the decomposition of RhB under UV irradiation. (b, c) Photocatalytic conversion of RhB under UV irradiation using TiO<sub>2</sub> clusters and P25 as the photocatalysts. The TiO<sub>2</sub> clusters in (b) were coated with a layer of silica before calcination, while the clusters in (c) were calcined without the silica treatment. Reproduced with permission from Ref. 33. Copyright © 2011 Tsinghua University Press and Springer-Verlag Berlin Heidelberg.

$$\alpha hv = A(hv - E_g)^\gamma \quad (2)$$

where  $\alpha$  is the absorption coefficient,  $h\nu$  the energy of the incident photon,  $A$  a constant,  $E_g$  the optical energy gap of the material, and  $\gamma$  the characteristic of the optical transition process which depends on whether the transition is symmetry allowed or not.<sup>49,50</sup> The calculation result shows that N-doping process not only red-shifts the absorption edge, as evidenced by the second gap at 2.85 eV, but also lowers down the main band edge from 3.2 eV to about 3.05 eV.

The degradation of RhB under visible light illumination was used again as the model system to study the catalytic performance of such catalysts, as shown in Figure 4.7a. Upon illuminated by visible light ( $\lambda > 400$  nm) for 5 hours, there was almost no change in the concentration of RhB if no catalyst was present, ruling out the possible sensitization process of RhB molecules under visible light irradiation. The calcination temperature also shows a great influence on the photocatalytic activity, which is in good agreement with the previous study. Due to the existence of rutile titania that can absorb visible light, the conversion percentage using P25 as the catalyst is about 40% in an irradiation period of 5 hours. Consistent with the cases for undoped samples, NTC400 shows the highest efficiency among all the calcined samples under the same condition due to its optimal crystallinity and surface area:  $\sim 50\%$  of the organic pollutants can be effectively removed in the same period.

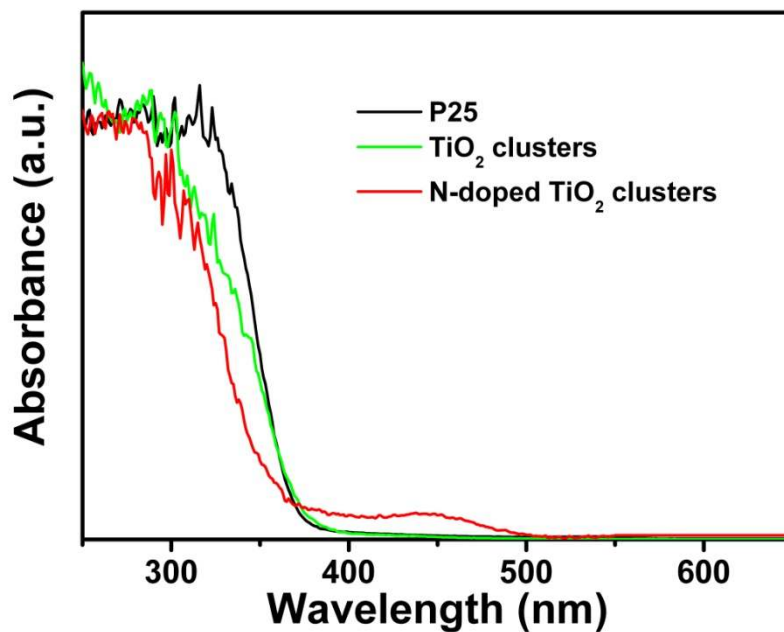


**Figure 4.6** UV-Vis diffuse reflectance absorption spectra of P25, TiO<sub>2</sub> clusters (TC400), and N-doped TiO<sub>2</sub> clusters (calcined at 400 °C, named NTC400). Reproduced with permission from Ref. 33. Copyright © 2011 Tsinghua University Press and Springer-Verlag Berlin Heidelberg.

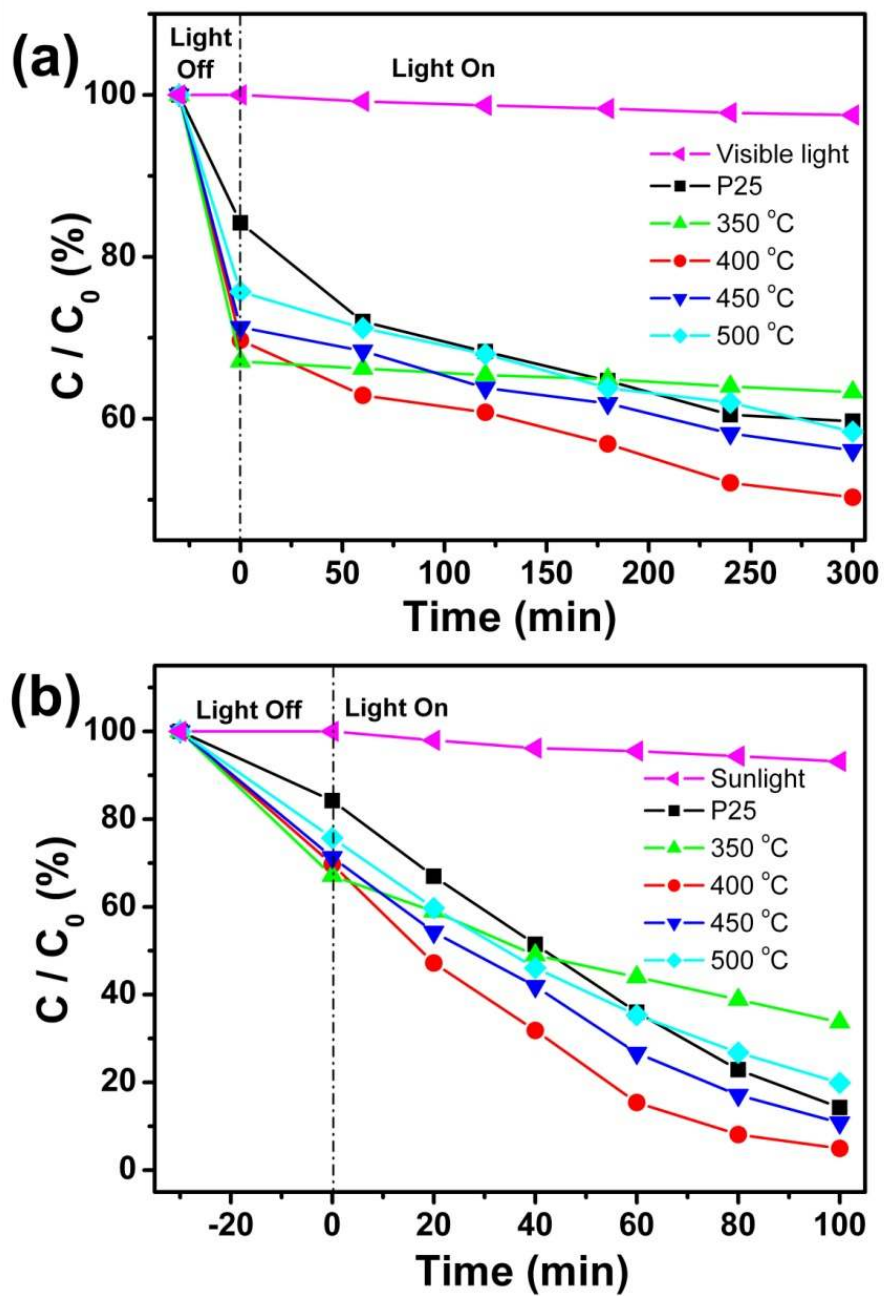


**Figure 4.7** Photocatalytic conversion of RhB under (a) visible light irradiation ( $\lambda > 400$  nm) and (b) direct sunshine illumination by using no catalyst, P25 aerioxide and N-doped  $\text{TiO}_2$  cluster as the photocatalysts. Reproduced with permission from Ref. 33. Copyright © 2011 Tsinghua University Press and Springer-Verlag Berlin Heidelberg.

To explore the photocatalytic activity of the as-prepared product for real applications, the photo-degradation of organic pollutant, i.e., RhB, was investigated under natural sunshine. As shown in Figure 4.7b, no sensitization process of RhB molecules under natural sunshine illumination has been found. Commercial P25 shows relatively higher activity due to the contribution of the UV component in the natural sunshine. With the aid of cluster-structured photocatalysts, the sunlight can efficiently decompose the RhB molecules. As shown in Figure 4.7b, the decomposition reaction can be completed within 100 min by using NTC400 as the photocatalyst, which is much shorter than the time required under illumination of the visible light. Consistent with the previous study, NTC350 shows the lowest activity, while NTC450 and NTC500 show decreasing activities. The cluster-structured photocatalysts can be recovered to catalyze multiple reactions under the direct sunshine. Photocatalysis was performed in an aqueous solution for many cycles by repeatedly adding RhB and irradiating with natural sunshine. To ensure that RhB was completely removed and had no influence on next cycle, further direct sunshine irradiation for 1 hour was conducted after each cycle. Centrifugation was used to recover the photocatalyst from the aqueous solution. As shown in Figure 4.8, the catalyst did not exhibit significant loss of photocatalytic activity after seven cycles. The slight differences in the decomposition rate of the RhB molecules in different cycles might be caused by the variation of the intensity of the sunlight.

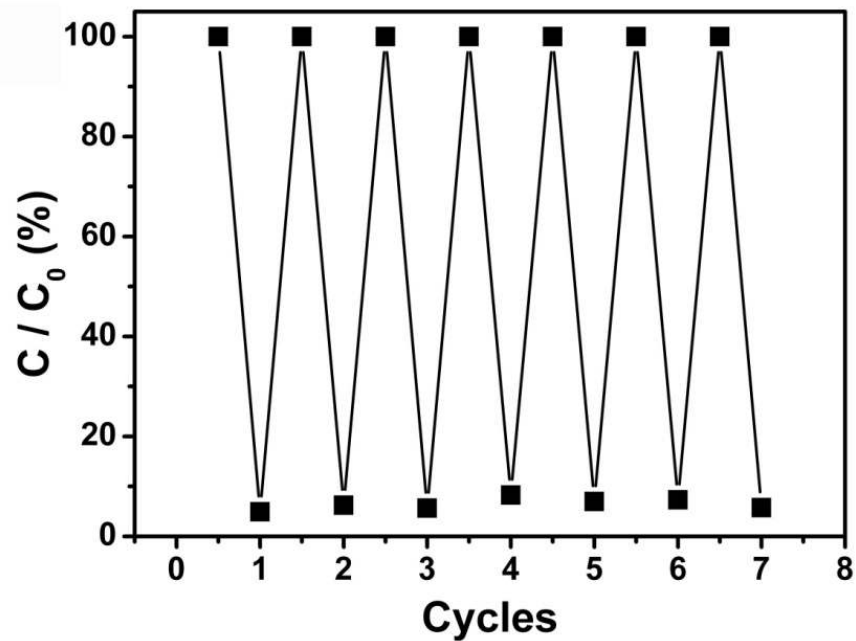


**Figure 4.8** Seven cycles of photocatalytic degradation of RhB in the presence of NTC400 clusters under direct irradiation of sunshine. Reproduced with permission from Ref. 33. Copyright © 2011 Tsinghua University Press and Springer-Verlag Berlin Heidelberg.

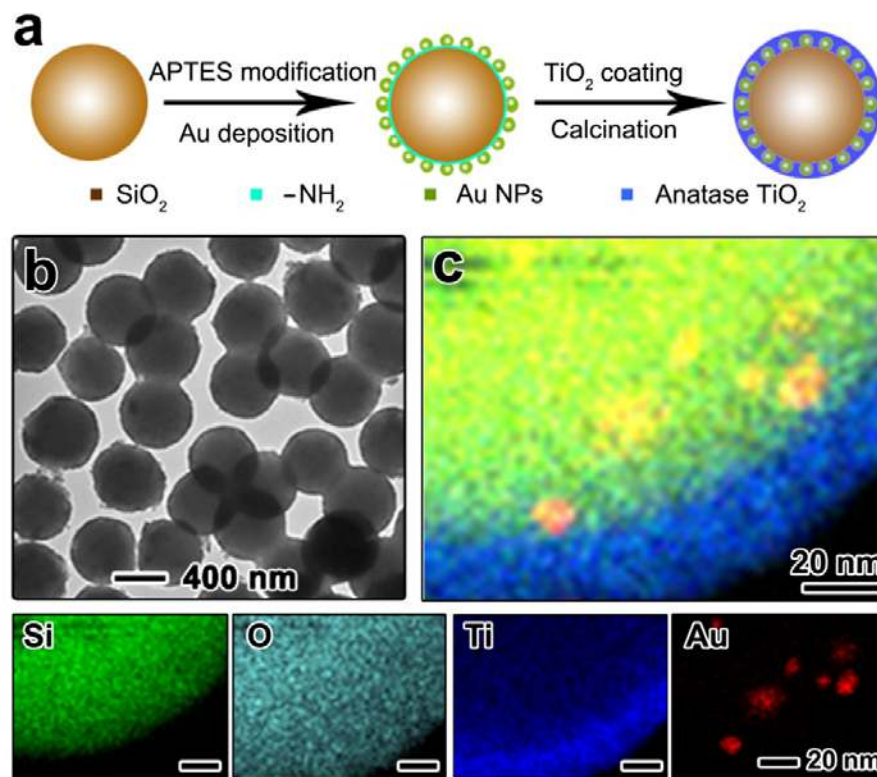
#### **4.4 Highly Active TiO<sub>2</sub>-Based Visible-Light Photocatalysts with Nonmetal Doping and Plasmonic Metal Decoration**

We report here the design and synthesis of a highly efficient, stable, and cost-effective TiO<sub>2</sub>-based photocatalyst with the desired properties mentioned above by combining simple sol-gel and calcination processes. The new catalyst has a sandwich structure that comprises a SiO<sub>2</sub> core, a layer of gold nanoparticles (AuNPs), and a doped-TiO<sub>2</sub> nanocrystalline shell. The sol-gel process allows for the convenient incorporation of AuNPs into the catalyst with controlled loading and location. TiO<sub>2</sub> is doped with both N and C using an unconventional method that involves introducing 3-aminopropyltriethoxysilane (APTES), which originally acts as a ligand for immobilization of AuNPs on the surface of the SiO<sub>2</sub> support but upon subsequent decomposition at high temperature serves as a source of both N and C for doping. Compared to traditional Au/TiO<sub>2</sub> composites in which AuNPs are loosely attached to the surface of TiO<sub>2</sub> such that they are unstable during calcination and subsequent photocatalysis, the sandwich structures with the AuNPs embedded inside a TiO<sub>2</sub> matrix protects the former from moving together and coagulating.<sup>51-53</sup> The encapsulation also increases the contact area between the AuNPs and the TiO<sub>2</sub> matrix, and therefore allows for more efficient electron transfer. A third advantage of our nanoarchitecture is that the pre-contact of Au with a TiO<sub>2</sub> surface can significantly increase the N loading by stabilizing the doped N inside

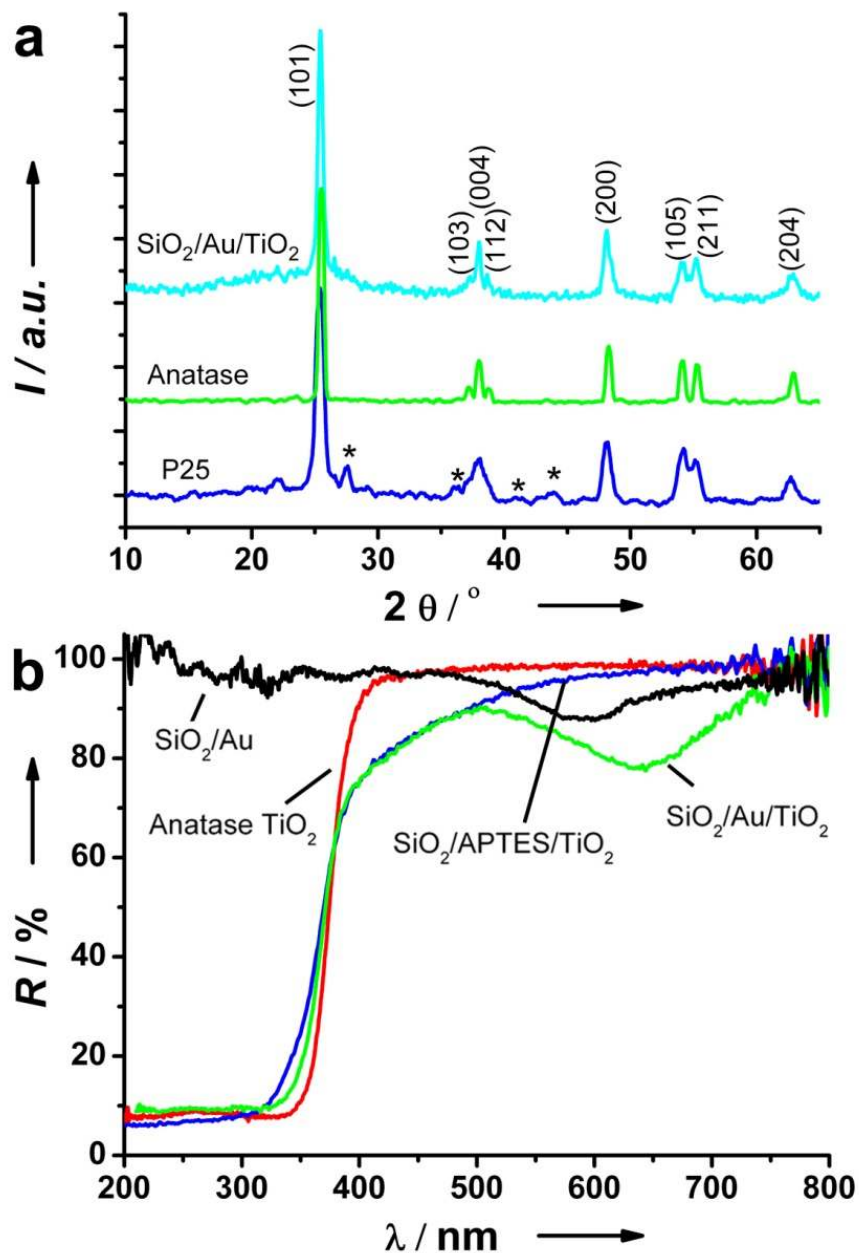


the oxide, and the doped N in turn can enhance the adhesion of AuNPs on the oxide surface through an electron transfer process.<sup>54</sup> As discussed later, only a relatively small quantity of AuNPs is required for optimal catalytic performance, making this catalyst feasible for large-scale practical applications.

The fabrication of the sandwich-structures is depicted in Figure 4.9a. SiO<sub>2</sub> particles were first synthesized through the Stöber method,<sup>55</sup> then surface-modified with a monolayer of the coupling agent APTES. AuNPs could then be adsorbed onto the silica surface through a strong chemical affinity towards primary amines. In the presence of hydroxypropyl cellulose, the Au/SiO<sub>2</sub> composite colloids were over-coated with a layer of amorphous TiO<sub>2</sub> by hydrolyzing tetrabutyl orthotitanate in ethanol solution.<sup>32,56,57</sup> The reddish composite was finally calcined at 500 °C for 2 hours under ambient conditions, producing a blue powder of uniform spheres with an average diameter of ~430 nm, as shown in Figure 4.9b. Energy dispersive X-ray (EDX) elemental mapping of a single sphere (Figure 4.9c) clearly confirms the expected sandwich structure. Observation under TEM at higher magnification reveals that the outer TiO<sub>2</sub> shell is composed of small nanoparticle grains with sizes of ~8-15 nm, which are optimal for anatase photocatalysts.<sup>32,58-60</sup> Nitrogen adsorption-desorption isotherm measurements on this sample suggest an average BET surface area of ~45.1 m<sup>2</sup>/g, confirming the porous nature of the TiO<sub>2</sub> shell.



**Figure 4.9** (a) Schematic illustration of the fabrication process of sandwich-structured SiO<sub>2</sub>/Au/TiO<sub>2</sub> photocatalyst. (b) Typical TEM image of the composite photocatalyst. (c) Elemental mapping of a single particle with the distribution of individual elements shown in the bottom row. Reproduced with permission from Ref. 61. Copyright © 2011 WILEY-VCH Verlag GmbH & Co. KGaA, Weinheim.



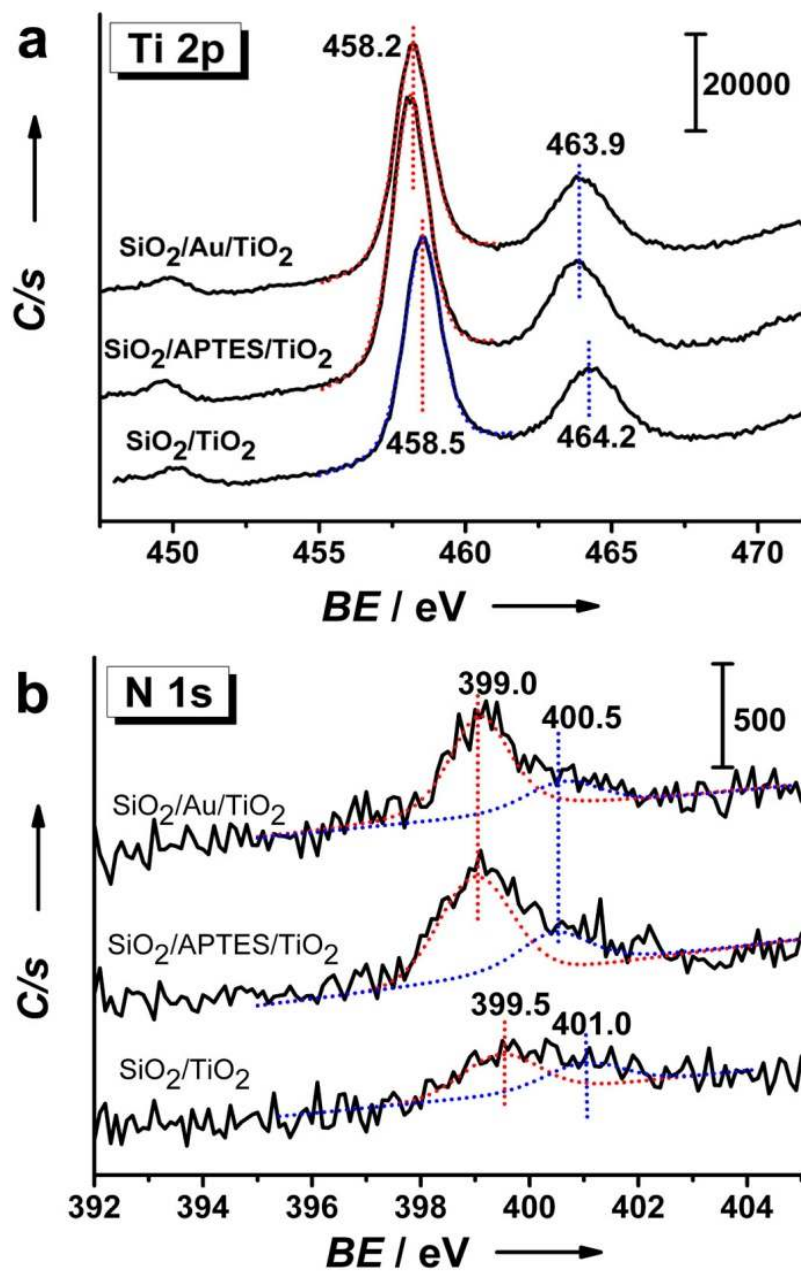
**Figure 4.10** (a) XRD patterns of the  $\text{SiO}_2/\text{Au}/\text{TiO}_2$  photocatalyst, commercial anatase  $\text{TiO}_2$  and P25 aerioxide. The star "\*" denotes rutile phase  $\text{TiO}_2$ . (b) UV-visible diffuse reflectance spectra of the three  $\text{TiO}_2$ -based photocatalysts and a control sample of AuNP-decorated silica particles. Reproduced with permission from Ref. 61. Copyright © 2011 WILEY-VCH Verlag GmbH & Co. KGaA, Weinheim.

Figure 4.10 shows X-ray diffraction (XRD) data used to identify the crystallographic phases of the titania in the as-prepared sandwich-structured catalysts, along with two reference samples including commercial anatase TiO<sub>2</sub> powder and P25 aerioxide. As it can be seen in Figure 4.10a, the sandwich structures show all the characteristic diffraction peaks also found in commercial anatase TiO<sub>2</sub>, with cell parameters  $a = b = 3.78 \text{ \AA}$ ,  $c = 9.51 \text{ \AA}$  (JCPDS card No. 73-1764). The peak broadening of the sandwich-structures suggests that the shells are composed of small nanocrystalline grains, which is consistent with our TEM observation. No characteristic peaks of crystallized gold can be found in our sample due to its very low concentration. As expected, P25 was found to be a mixture of anatase and rutile phases.<sup>32</sup>

Diffuse reflectance UV-Vis spectroscopy was used to study the optical properties of the sandwich-structured photocatalyst and contrast those with the reference samples (Figure 4.10b). While the commercial anatase sample strongly absorbs light only in the UV region, noticeable absorption in the visible region can be observed for all SiO<sub>2</sub>/APTES/TiO<sub>2</sub> structures, even in the absence of AuNPs. This confirms doping of TiO<sub>2</sub> with N and/or C as reported by Sato and others.<sup>62,63</sup> Moreover, with AuNPs, another absorption band at  $\sim 650 \text{ nm}$  appears, which can be mainly ascribed to the surface plasmon resonance of AuNPs. Compared to a reference sample consisting of AuNPs-decorated SiO<sub>2</sub> spheres, which shows an absorption band at  $\sim 590 \text{ nm}$ , the new

absorption band in the SiO<sub>2</sub>/APTES/Au/TiO<sub>2</sub> structure is red shifted, a difference that can be attributed to the high refractive index of the TiO<sub>2</sub> (n = 2.488 for pure anatase TiO<sub>2</sub>) surrounding the AuNPs,<sup>31</sup> suggesting a good contact between AuNPs and TiO<sub>2</sub> grains.

X-ray photoelectron spectroscopy (XPS) was used to investigate the C and/or N doping in the TiO<sub>2</sub> shells. Without doping, for the simple TiO<sub>2</sub>-coated SiO<sub>2</sub> sample, Ti exhibits a 2p<sub>3/2</sub> peak at 458.5 eV, which corresponds to the binding energy of Ti<sup>4+</sup> in TiO<sub>2</sub> (Figure 4.11a).<sup>64</sup> Once APTES is introduced between the SiO<sub>2</sub> core and the TiO<sub>2</sub> shell, however, the Ti 2p peak shifts to a lower binding energy, 458.2 eV. This shift is indicative of the incorporation of N and/or C into the TiO<sub>2</sub> lattice.<sup>65</sup> Due to the low loadings used and the TiO<sub>2</sub> overcoating, the XPS signals for N and C are relatively weak. As shown in Figure 4.11b, all the samples display a weak and broad N 1s XPS peak around 400.5-401.0 eV, which can be attributed to adsorbed N<sub>2</sub> molecules.<sup>66</sup> Nitrogen-doped TiO<sub>2</sub> has recently been reported to exhibit a peak at 396 eV in the N 1s XPS data,<sup>66-69</sup> due to the substitutionally doped N<sup>3-</sup> component of Ti-N, but we could not detect any signal at this position with our SiO<sub>2</sub>/APTES/TiO<sub>2</sub> and SiO<sub>2</sub>/Au/TiO<sub>2</sub> samples, probably because of the limited doping at the vicinity of SiO<sub>2</sub>/TiO<sub>2</sub> interface. Instead, we observed a peak at 399.0 eV which may be produced by jointly-bonded C-N in TiO<sub>2-x-y</sub>N<sub>x</sub>C<sub>y</sub> films.<sup>70</sup> The existence of additional carbon resulted from the decomposition of APTES has also been confirmed by the C 1s spectra.<sup>70-75</sup>



**Figure 4.11** XPS measurements for the as-obtained  $\text{SiO}_2/\text{Au}/\text{TiO}_2$  photocatalyst: (a) Ti 2p, and (b) N 1s. All the XPS data have been calibrated with the binding energy of Si-O from  $\text{SiO}_2$  at 103.4 eV. Reproduced with permission from Ref. 61. Copyright © 2011 WILEY-VCH Verlag GmbH & Co. KGaA, Weinheim.

The photocatalytic activity was evaluated by measuring the degradation rate of rhodamine B (RhB), by monitoring its characteristic absorption band at 553 nm. Unlike many prior reports in which the incorporation of a metal to TiO<sub>2</sub> degrades catalytic performance in the UV region,<sup>76</sup> the sandwiched structures show performance comparable to P25 under UV irradiation, attesting to the overall positive impact of the non-metal doping and gold decoration on the catalytic activity. Moreover, under visible light irradiation ( $\lambda > 400$  nm), the SiO<sub>2</sub>/Au/TiO<sub>2</sub> nanostructures display significantly higher efficiency than that of P25. The sandwich-structured photocatalyst can decompose ~ 96% of RhB in 5 hours, while P25 containing an equivalent amount of TiO<sub>2</sub> can convert only ~ 42% of RhB under identical conditions (Figure 4.12a). The commercial anatase is essentially inactive. We also compared the performance of the SiO<sub>2</sub>/Au/TiO<sub>2</sub> to SiO<sub>2</sub>/TiO<sub>2</sub> and SiO<sub>2</sub>/APTES/TiO<sub>2</sub> composites synthesized under similar conditions. Before catalysis, the TiO<sub>2</sub> in all samples was identified as pure anatase by XRD. As shown in Figure 4.12a, without the modification of APTES, the SiO<sub>2</sub>/TiO<sub>2</sub> core-shell structures show very low activity under visible light irradiation. However, after C/N doping, the core-shell photocatalyst becomes active, showing 48% degradation of RhB in 5 hours. This is already an improvement over the widely recognized P25 aerioxide photocatalyst.<sup>77</sup> Additional decoration of the SiO<sub>2</sub>/TiO<sub>2</sub> interface with 0.1% of AuNPs further doubles the decomposition rate.

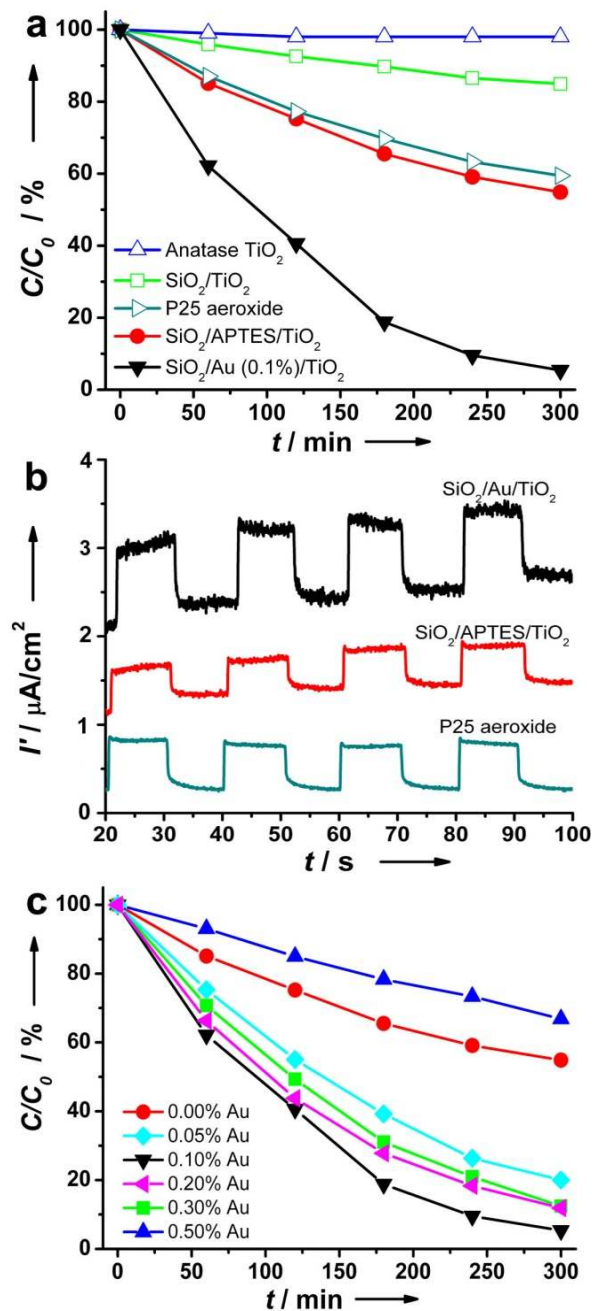


**Figure 4.12** (a) Photodegradation of RhB using anatase,  $\text{SiO}_2/\text{TiO}_2$ , P25,  $\text{SiO}_2/\text{APTES}/\text{TiO}_2$  and  $\text{SiO}_2/\text{Au}/\text{TiO}_2$  under visible light. (b) Chronoamperometry measurements of P25,  $\text{SiO}_2/\text{APTES}/\text{TiO}_2$ , and  $\text{SiO}_2/\text{Au}/\text{TiO}_2$  under periodic illumination of visible light. (c) The influence of AuNPs loading on the catalytic activity of  $\text{SiO}_2/\text{Au}/\text{TiO}_2$  sandwich structures studied by using the decomposition of RhB as the model system. Reproduced with permission from Ref. 61. Copyright © 2011 WILEY-VCH Verlag GmbH & Co. KGaA, Weinheim.



Chronoamperometry (CA) measurements were performed to characterize the photo-generated current density under a potential of 0.8 V and periodic illumination of visible light ( $\lambda > 400$  nm). As indicated in Figure 4.12b, photo-generated currents were seen for all samples, but SiO<sub>2</sub>/Au/TiO<sub>2</sub> showed a significantly higher value ( $\sim 0.80 \mu\text{A}/\text{cm}^2$ ) than P25 ( $\sim 0.45 \mu\text{A}/\text{cm}^2$ ) and SiO<sub>2</sub>/APTES/TiO<sub>2</sub> ( $\sim 0.40 \mu\text{A}/\text{cm}^2$ ). The shape of the CA curves is well maintained after many cycles of light illumination, implying very good photocatalytic stability.

It is clear that decoration of titania-based photocatalysts with AuNPs is an important factor to achieve the high catalytic efficiency. A systematic study was carried out to assess this effect by varying the loading of AuNPs from 0 to 0.5 wt% in six otherwise identical samples (Figure 4.12c). Interestingly, the visible-light activity of the samples peaks at 0.1 wt% loading of AuNPs. It is generally understood that AuNPs supported on TiO<sub>2</sub> have three probable functions in photocatalysis: one, to help harvest the visible light energy, thanks to its plasmonic property,<sup>31</sup> second, to enhance charge separation by serving as an electron reservoir,<sup>34,78,79</sup> and third, to act as recombination center, which negatively affects catalytic activity.<sup>80</sup> When the loading of AuNPs is low, their primary function is to enhance the charge separation and hence promote the oxidation of organic molecules under visible light. However, excessive amounts of metal particles may also deteriorate the catalytic performance by increasing the occurrence of exciton

recombination,<sup>80</sup> with the reaction rate gradually decreasing when the loading of AuNPs exceeds 0.1 wt%. The low loading (0.1 wt%) of the AuNPs required for achieving high catalytic performance also has practical significance in terms of cost: many prior reports on Au/TiO<sub>2</sub> composite photocatalysts require Au loading of ~1-5 wt%, which has prevented their large scale application.<sup>79</sup>

In addition to the effects on light harvesting and charge separation, the AuNPs may also contribute to the enhancement in nonmetal doping for TiO<sub>2</sub>. Sanz et al. have demonstrated both theoretically and experimentally that Au pre-adsorption on TiO<sub>2</sub> surfaces can significantly stabilize implanted N, increase the reachable amount of N loading in the oxide, and enhance Au-surface adhesion energy due to an electron transfer from the Au 6s orbitals to the partially occupied N 2p orbitals.<sup>54</sup> As the non-metal doping process usually requires annealing at elevated temperatures, which may cause the AuNPs to sinter, the unique sandwich structure proposed in this work represents an ideal system to overcome sintering: AuNPs are unable to move within the TiO<sub>2</sub> matrix, thus prevents coagulation during calcination, ensures high stability, and improves Au/TiO<sub>2</sub> surface contact.

To explore the photocatalytic activity of our samples for real applications, the photo-degradation of organic compounds was investigated under natural sunshine, which contains both UV, visible, and IR light. As shown in Figure 4.13a, sunlight can completely decompose RhB molecules within 40 min with the aid of sandwich-structured photocatalysts, while the conversion only reaches ~ 38% with P25 and ~ 27% with the commercial anatase sample during the same period. We also tested the SiO<sub>2</sub>/Au/TiO<sub>2</sub> catalyzed degradation of other organic molecules under sunlight, including rhodamine 6G (R6G), methylene blue (MB), and 2, 4-dichlorophenol (2, 4-DCP), at the same initial concentration. As shown in Figure 4.13b, all of those molecules can be decomposed almost completely (> 93%) within 40 min. As shown in Figure 4.13c, these photocatalysts are also mechanically robust and chemically stable: they can be recovered and reused to catalyze multiple cycles of degradation reactions under direct sunlight.

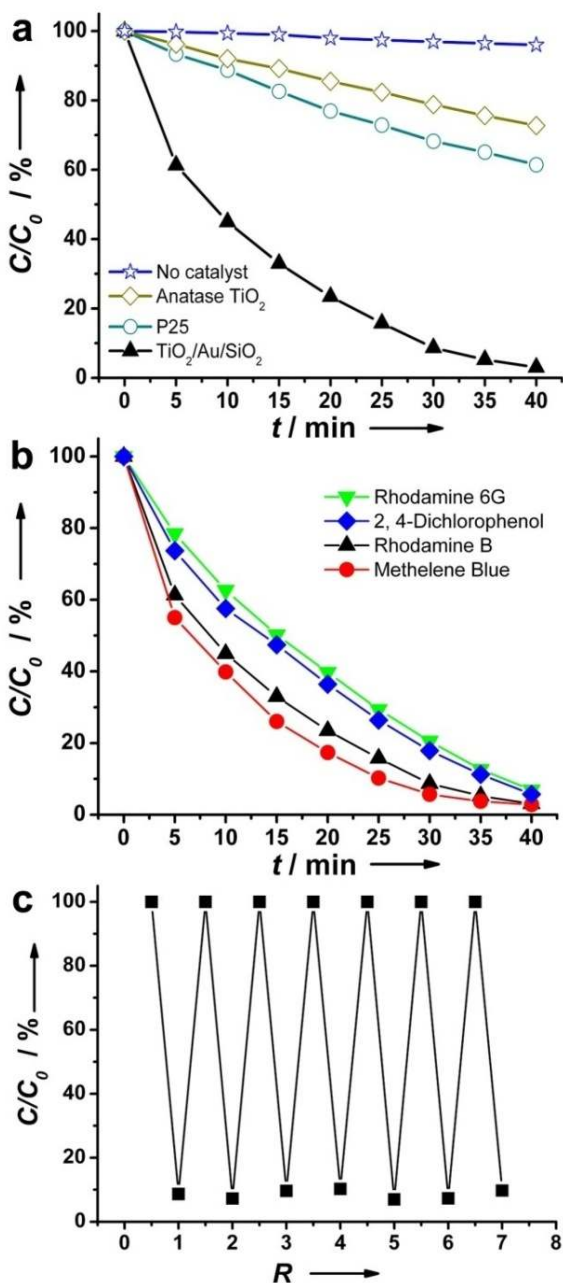


**Figure 4.13** (a) Photodegradation of RhB without catalyst and with anatase, P25, and SiO<sub>2</sub>/Au/TiO<sub>2</sub> under direct sunlight. (b) Photodegradation of various organic dyes, including RhB, R6G, methylene blue, and 2, 4-dichlorophenol with sandwich-structured catalyst under direct sunlight. (c) 7 cycles of the degradation of RhB with SiO<sub>2</sub>/Au/TiO<sub>2</sub> photocatalyst under sunlight illumination, demonstrating the stability and recyclability of the catalyst. The duration of sunlight exposure in each cycle is 30 min. Reproduced with permission from Ref. 61. Copyright © 2011 WILEY-VCH Verlag GmbH & Co. KGaA, Weinheim.

## 4.5 Conclusion

In summary, we have focused on the engineering of TiO<sub>2</sub>-based nanomaterials for photocatalytic applications. First, we have demonstrated the preparation of mesoporous anatase TiO<sub>2</sub> nanocrystal clusters with large surface area and enhanced photocatalytic activity. The synthesis involves the self-assembly of hydrophobic TiO<sub>2</sub> nanocrystals into submicron clusters in emulsion droplets, coating of these clusters with a silica layer, thermal treatment at high temperature to remove organic ligands and improve the crystallinity of clusters, and finally etching of the silica to reveal the mesoporous catalyst. The initial silica coating helps the clusters maintain their small grain size and high surface area after calcination at high temperatures, while the eventual removal of the silica renders the clusters high dispersibility in water. TiO<sub>2</sub> nanocrystal clusters with optimal balance of high crystallinity and large surface area can be produced at a calcination temperature of 400 °C, which ensures an enhanced photocatalytic activity as demonstrated by the high charge separation efficiency in electrochemical characterizations, and the efficient decomposition of organics under illumination of UV light. The porous structure of the TiO<sub>2</sub> nanocrystal clusters also allows convenient nitrogen doping, which further promotes the photocatalytic performance in visible light and natural sunlight. We believe that organizing nanocrystals into mesoporous clusters

represents a versatile and useful strategy for designing photocatalysts with enhanced activity and stability.

Additionally, we have demonstrated a sandwich-structured  $\text{SiO}_2/\text{Au}/\text{TiO}_2$  photocatalyst that shows high efficiency in catalyzing decomposition of organic compounds under illumination of UV, visible light, and natural sunlight. The structural design of the photocatalyst takes advantage of the synergetic interaction between adsorbed gold and implanted nitrogen, and produces stable nonmetal-doped anatase nanoparticles with precisely controlled AuNPs decoration. The excellent photocatalytic efficiency can be attributed to the interfacial non-metal doping, which improves visible light activity, to the plasmonic metal decoration, which enhances light harvesting and charge separation, and to the small grain size of anatase nanocrystals, which reduces recombination rate of excitons.

## 4.6 References

- (1) Oregan, B.; Gratzel, M. *Nature* **1991**, 353, 737.
- (2) An, C.; Peng, S.; Sun, Y. *Adv. Mater.* **2010**, 22, 2570.
- (3) Fujishima, A.; Honda, K. *Nature* **1972**, 238, 37.
- (4) Linsebigler, A. L.; Lu, G.; Yates, J. T., Jr. *Chem. Rev. (Washington, D. C.)* **1995**, 95, 735.
- (5) Fox, M. A.; Dulay, M. T. *Chem. Rev.* **1993**, 93, 341.
- (6) Fujishima, A.; Zhang, X. T.; Tryk, D. A. *Surf Sci Rep* **2008**, 63, 515.
- (7) Trentler, T. J.; Denler, T. E.; Bertone, J. F.; Agrawal, A.; Colvin, V. L. *J. Am. Chem. Soc.* **1999**, 121, 1613.
- (8) Wu, B. H.; Guo, C. Y.; Zheng, N. F.; Xie, Z. X.; Stucky, G. D. *J Am Chem Soc* **2008**, 130, 17563.
- (9) Yang, H. G.; Sun, C. H.; Qiao, S. Z.; Zou, J.; Liu, G.; Smith, S. C.; Cheng, H. M.; Lu, G. Q. *Nature* **2008**, 453, 638.
- (10) Lee, J.; Christopher Orilall, M.; Warren, S. C.; Kamperman, M.; DiSalvo, F. J.; Wiesner, U. *Nature Materials* **2008**, 7, 222.
- (11) Liu, X.; Gao, Y.; Cao, C.; Luo, H.; Wang, W. *Langmuir* **2010**, 26, 7671.
- (12) Lou, X. W.; Yuan, C.; Archer, L. A. *Small* **2007**, 3, 261.
- (13) Moon, H. G.; Shim, Y.-S.; Jang, H. W.; Kim, J.-S.; Choi, K. J.; Kang, C.-Y.; Choi, J.-W.; Park, H.-H.; Yoon, S.-J. *Sensors and Actuators B: Chemical* **2010**, 149, 116.
- (14) Yin, Y.; Rioux, R. M.; Erdonmez, C. K.; Hughes, S.; Somorjai, G. A.; Alivisatos, A. P. *Science* **2004**, 304, 711.
- (15) Li, G.; Kang, E. T.; Neoh, K. G.; Yang, X. *Langmuir* **2009**, 25, 4361.
- (16) Li, X.; Xiong, Y.; Li, Z.; Xie, Y. *Inorganic Chemistry* **2006**, 45, 3493.
- (17) Joo, J. B.; Kim, P.; Kim, W.; Kim, J.; Kim, N. D.; Yi, J. *Current Applied Physics* **2008**, 8, 814.
- (18) Chen, D. H.; Huang, F. Z.; Cheng, Y. B.; Caruso, R. A. *Adv. Mater.* **2009**, 21, 2206.

- (19) Kim, Y. J.; Lee, M. H.; Kim, H. J.; Lim, G.; Choi, Y. S.; Park, N. G.; Kim, K.; Lee, W. I. *Adv. Mater.* **2009**, *21*, 3668.
- (20) Choi, W. Y.; Termin, A.; Hoffmann, M. R. *J. Phys. Chem.* **1994**, *98*, 13669.
- (21) Asahi, R.; Morikawa, T.; Ohwaki, T.; Aoki, K.; Taga, Y. *Science* **2001**, *293*, 269.
- (22) Sakthivel, S.; Kisch, H. *Angew. Chem. Int. Ed.* **2003**, *42*, 4908.
- (23) Khan, S. U. M.; Al-Shahry, M.; Ingler, W. B. *Science* **2002**, *297*, 2243.
- (24) Emeline, A.; Kuznetsov, V.; Rybchuk, V.; Serpone, N. *Int. J. Photoenergy* **2008**, *2008*, 1.
- (25) Chen, X.; Liu, L.; Yu, P. Y.; Mao, S. S. *Science* **2011**, *331*, 746.
- (26) Graciani, J.; Alvarez, L. J.; Rodriguez, J. A.; Sanz, J. F. *J. Phys. Chem. C* **2008**, *112*, 2624.
- (27) Batzill, M.; Morales, E. H.; Diebold, U. *Phys. Rev. Lett.* **2006**, *96*, 026103.
- (28) Nambu, A.; Graciani, J.; Rodriguez, J. A.; Wu, Q.; Fujita, E.; Sanz, J. F. *J. Chem. Phys.* **2006**, *125*, 094706.
- (29) Furube, A.; Du, L.; Hara, K.; Katoh, R.; Tachiya, M. *J. Am. Chem. Soc.* **2007**, *129*, 14852.
- (30) Naya, S.; Inoue, A.; Tada, H. *J. Am. Chem. Soc.* **2010**, *132*, 6292.
- (31) Awazu, K.; Fujimaki, M.; Rockstuhl, C.; Tominaga, J.; Murakami, H.; Ohki, Y.; Yoshida, N.; Watanabe, T. *J. Am. Chem. Soc.* **2008**, *130*, 1676.
- (32) Ye, M.; Zhang, Q.; Hu, Y.; Ge, J.; Lu, Z.; He, L.; Chen, Z.; Yin, Y. *Chem. Eur. J.* **2010**, *16*, 6243.
- (33) Zhang, Q.; Joo, J.-B.; Lu, Z.; Dahl, M.; Oliveira, D.; Ye, M.; Yin, Y. *Nano Res.* **2011**, *4*, 103.
- (34) Corma, A.; Serna, P. *Science (Washington, DC, U. S.)* **2006**, *313*, 332.
- (35) Trentler, T. J.; Denler, T. E.; Bertone, J. F.; Agrawal, A.; Colvin, V. L. *J. Am. Chem. Soc.* **1999**, *121*, 1613.
- (36) Lu, Z.; Ye, M.; Li, N.; Zhong, W.; Yin, Y. *Angew. Chem. Int. Ed.* **2010**, *49*, 1862.
- (37) Kwon, S. G.; Hyeon, T. *Acc. Chem. Res.* **2008**, *41*, 1696.
- (38) Chen, X.; Mao, S. S. *Chem. Rev.* **2007**, *107*, 2891.



- (39) Tian, B. Z.; Li, C. Z.; Gu, F.; Jiang, H. B. *Catal. Comm.* **2009**, *10*, 925.
- (40) Trentler, T. J.; Denler, T. E.; Bertone, J. F.; Agrawal, A.; Colvin, V. L. *J. Am. Chem. Soc.* **1999**, *121*, 1613.
- (41) Stober, W.; Fink, A.; Bohn, E. *J. Colloid Interface Sci.* **1968**, *26*, 62.
- (42) Bai, F.; Wang, D. S.; Huo, Z. Y.; Chen, W.; Liu, L. P.; Liang, X.; Chen, C.; Wang, X.; Peng, Q.; Li, Y. D. *Angew. Chem. Int. Ed.* **2007**, *46*, 6650.
- (43) Wang, D. S.; Xie, T.; Peng, Q.; Li, Y. D. *J. Am. Chem. Soc.* **2008**, *130*, 4016.
- (44) Lu, Z.; Ye, M.; Li, N.; Zhong, W.; Yin, Y. *Angew. Chem. Int. Ed.* **2010**, *49*, 1862.
- (45) Lu, Z.; Duan, J.; He, L.; Hu, Y.; Yin, Y. *Anal. Chem.* **2010**, *82*, 7249.
- (46) Lu, Z.; He, L.; Yin, Y. *Chem. Commun.* **2010**, *46*, 6174.
- (47) Gribb, A. A.; Banfield, J. F. *Am. Miner.* **1997**, *82*, 717.
- (48) Zhang, H. Z.; Banfield, J. F. *J. Mater. Chem.* **1998**, *8*, 2073.
- (49) Gao, Y. F.; Masuda, Y.; Peng, Z. F.; Yonezawa, T.; Koumoto, K. *J. Mater. Chem.* **2003**, *13*, 608.
- (50) Tang, H.; Prasad, K.; Sanjines, R.; Schmid, P. E.; Levy, F. *J. Appl. Phys.* **1994**, *75*, 2042.
- (51) Zhang, Q.; Lee, I.; Ge, J.; Zaera, F.; Yin, Y. *Adv. Funct. Mater.* **2010**, *20*, 2201.
- (52) Ge, J.; Zhang, Q.; Zhang, T.; Yin, Y. *Angew. Chem. Int. Ed.* **2008**, *47*, 8924.
- (53) Lee, I.; Zhang, Q.; Ge, J.; Yin, Y.; Zaera, F. *Nano Res.* **2011**, *4*, 115.
- (54) Graciani, J.; Nambu, A.; Evans, J.; Rodriguez, J. A.; Sanz, J. F. *J. Am. Chem. Soc.* **2008**, *130*, 12056.
- (55) Stober, W.; Fink, A.; Bohn, E. *J. Colloid Interface Sci.* **1968**, *26*, 62.
- (56) Lee, J. W.; Othman, M. R.; Eom, Y.; Lee, T. G.; Kim, W. S.; Kim, J. *Microporous Mesoporous Mater.* **2008**, *116*, 561.
- (57) Ye, M.; Zorba, S.; He, L.; Hu, Y.; Maxwell, R. T.; Farah, C.; Zhang, Q.; Yin, Y. *J. Mater. Chem.* **2010**, *20*, 7965.
- (58) Anpo, M.; Shima, T.; Kodama, S.; Kubokawa, Y. *J. Phys. Chem.* **2002**, *91*, 4305.
- (59) Chae, S. Y.; Park, M. K.; Lee, S. K.; Kim, T. Y.; Kim, S. K.; Lee, W. I. *Chem. Mater.* **2003**, *15*, 3326.

- (60) Wang, C.-C.; Zhang, Z.; Ying, J. Y. *Nanostruct. Mater.* **1997**, *9*, 583.
- (61) Zhang, Q.; Lima, D. Q.; Lee, I.; Zaera, F.; Chi, M. F.; Yin, Y. D. *Angew. Chem. Int. Ed.* **2011**, *50*, 7088.
- (62) Sato, S. *Chem. Phys. Lett.* **1986**, *123*, 126.
- (63) Livraghi, S.; Paganini, M. C.; Giamello, E.; Selloni, A.; Di Valentin, C.; Pacchioni, G. *J. Am. Chem. Soc.* **2006**, *128*, 15666.
- (64) Diebold, U.; Madey, T. *Surf. Sci. Spect.* **1996**, *4*, 227.
- (65) Wang, J.; Tafen, D. N.; Lewis, J. P.; Hong, Z. L.; Manivannan, A.; Zhi, M. J.; Li, M.; Wu, N. Q. *J. Am. Chem. Soc.* **2009**, *131*, 12290.
- (66) Saha, N. C.; Tompkins, H. G. *J. Appl. Phys.* **1992**, *72*, 3072.
- (67) Irie, H.; Watanabe, Y.; Hashimoto, K. *J. Phys. Chem. B* **2003**, *107*, 5483.
- (68) Sano, T.; Negishi, N.; Koike, K.; Takeuchi, K.; Matsuzawa, S. *J. Mater. Chem.* **2004**, *14*, 380.
- (69) Diwald, O.; Thompson, T. L.; Zubkov, T.; Goralski, E. G.; Walck, S. D.; Yates, J. T. *J. Phys. Chem. B* **2004**, *108*, 6004.
- (70) Yang, J.; Bai, H. Z.; Tan, X. C.; Lian, J. S. *Appl. Surf. Sci.* **2006**, *253*, 1988.
- (71) Wu, K. R.; Hung, C. H. *Appl. Surf. Sci.* **2009**, *256*, 1595.
- (72) Kamisaka, H.; Adachi, T.; Yamashita, K. *J. Chem. Phys.* **2005**, *123*, 084704.
- (73) Iucci, G.; Dettin, M.; Battocchio, C.; Gambaretto, R.; Di Bello, C.; Polzonett, G. *Mater. Sci. Eng. C* **2007**, *27*, 1201.
- (74) Ren, W. J.; Ai, Z. H.; Jia, F. L.; Zhang, L. Z.; Fan, X. X.; Zou, Z. G. *Appl. Catal. B* **2007**, *69*, 138.
- (75) Xiao, Q.; Zhang, J.; Xiao, C.; Si, Z. C.; Tan, X. O. *Solar Energy* **2008**, *82*, 706.
- (76) Liu, Z.; Hou, W.; Pavaskar, P.; Aykol, M.; Cronin, S. B. *Nano Lett.* **2011**, *11*, 1111.
- (77) Hurum, D. C.; Agrios, A. G.; Gray, K. A.; Rajh, T.; Thurnauer, M. C. *J. Phys. Chem. B* **2003**, *107*, 4545.
- (78) Subramanian, V.; Wolf, E. E.; Kamat, P. V. *J. Am. Chem. Soc.* **2004**, *126*, 4943.
- (79) Primo, A.; Corma, A.; Garcia, H. *Phys. Chem. Chem. Phys.* **2011**, *13*, 886.
- (80) Wu, Y. M.; Liti, H. B.; Zhang, J. L.; Chen, F. *J. Phys. Chem. C* **2009**, *113*, 14689.

## **Chapter 5**

### **Conclusion and Outlook**

#### **5.1 Conclusion of this Dissertation**

Catalysis has been widely used in the human society for thousands of years. Since the establishment of the first industrialized catalytic process in 1913, catalysis has been of critical importance to the modern society.<sup>1-4</sup> Nowadays, catalysis has been used in many fields, such as oil refining, food processing, and pollution control. It is highly desirable that catalysts with high efficiency and high selectivity could be prepared in a large scale and in a cost-effective manner. It is believed that nanotechnology could significantly change the research in catalysis, since nanomaterials have many advantages over their bulk counterparts, including more active sites, higher catalytic activity, high selectivity etc. More importantly, the development of nanotechnology allows people to design and fabricate catalysts in the atomic scale, which may give rise to more precise control over the properties of nanomaterials.

Although impressive progress has been achieved since the rise of nanotechnology in the 1990s, there are still many challenges remained in the research field. For example, it is still a great challenge to design and prepare nanomaterials with desired morphology, due to the fact that most of the existing systems are based on empirical data. Another

major challenge for the use of nanostructured materials as catalysts is their chemical and structural stability, owing to the large surface area and, as a result, the high surface energy of such nanomaterials. Additionally, how to scale up the lab results, usually milligram-scale production, to industrialized scale (ton scale production) is a big challenge facing the researchers. This Dissertation has discussed our efforts in the engineering of nanomaterials and their applications in catalysis. We are trying to shed some light on the development of nanotechnology and catalysis research.

By using Ag nanoplates as a model system, we attempt to outline the key components that determine the formation of nanomaterials, clarify the roles of each reagent, provide highly reproducible recipes for synthesis, and therefore take a significant step towards the complete understanding of the mechanism behind the experimental phenomena.<sup>5-7</sup> Using this understanding, Ag nanoplates with various aspect ratios and widely tunable SPR bands have been successfully obtained.<sup>8</sup> We have further demonstrated that the optical properties of Ag nanoplates can be precisely tuned in a wide range through a UV light induced reconstruction process.<sup>9</sup> The as-obtained product shows improved stability against long time aging process.

One of the major challenges for the use of nanostructured materials as catalysts is their chemical and structural stability.<sup>10-19</sup> In the second stage, by embedding nanocatalysts within a mesoporous metal oxide shell, we are able to prepare nanocatalysts with

enhanced stability in both gas and aqueous phase reactions. A general strategy, called the “surface-protected etching” process, has been developed as the major synthetic tool for producing mesoporous shells for the stabilization of noble metal nanocatalysts. Through the physical confinement, metal nanocatalysts show superior stability over unprotected nanocatalysts. A sandwich-like structure was further proposed, in which multi-functional materials could be incorporated to make recyclable and highly efficient catalysts.

For practical applications, TiO<sub>2</sub>-based nanomaterials have been used as the model system to investigate the factors that determine the preparation of efficient photocatalysts.<sup>20-24</sup> Mesoporous TiO<sub>2</sub> photocatalysts with high surface area and high photocatalytic activity have been prepared through a self-assembly approach. Based on our improved understanding of photocatalysts, we have designed and synthesized a highly efficient, stable, and cost-effective TiO<sub>2</sub>-based photocatalyst by combining both non-metal doping and noble metal decoration. The new photocatalysts show excellent performance in degradation reactions of a number of organic compounds under the irradiation of UV, visible, and direct sunlight.

## 5.2 Outlook and Future Work

With the development of nanotechnology, people will be able to design nanocatalysts with computer-based software. By completely interpreting the underlying mechanisms of the synthesis of nanomaterials, some general understandings will be established, which give rise to the fabrication of standard building units of nanocatalysts. The preparation of nanocatalysts will become very easy as people will be able to generate nanocatalysts quickly and reliably by joining those small building units together. Nanocatalysts with desired morphology as well as desired properties, such as high efficiency and high selectivity, could be obtained in large-volume production and in a low cost manner by tailoring their geometry and composition.

In the future, my research will be mainly focused on the preparation of  $\text{TiO}_2$ -based photocatalysts. It has been pointed out that the facets of nanomaterials could determine its photocatalytic activity. Based on our experience in the controllable synthesis of nanocrystal, we will study this system in-depth and try to improve the photocatalytic efficiency by interpreting the shape-dependent property. Additionally, the composition of  $\text{TiO}_2$  is of critical importance. Our efforts will also be devoted to developing visible-light active photocatalysts by engineering its composition.

### 5.3 References

- (1) Zaera, F. *J. Phys. Chem. Lett.* **2010**, *1*, 621.
- (2) Somorjai, G. A.; Tao, F.; Park, J. Y. *Top. Catal.* **2008**, *47*, 1.
- (3) Somorjai, G. A.; Frei, H.; Park, J. Y. *J. Am. Chem. Soc.* **2009**, *131*, 16589.
- (4) Somorjai, G. A. *Appl. Surf. Sci.* **1997**, *121/122*, 1.
- (5) Zhang, Q.; Li, N.; Goebel, J.; Lu, Z. D.; Yin, Y. D. *J Am Chem Soc* **2011**, *133*, 18931.
- (6) Li, N.; Zhang, Q.; Quinlivan, S.; Goebel, J.; Gan, Y.; Yin, Y. *ChemPhysChem* **2012**, DOI: 10.1002/cphc.201101018.
- (7) Goebel, J.; Zhang, Q.; He, L.; Yin, Y. D. *Angew Chem Int Edit* **2012**, *51*, 552.
- (8) Zhang, Q.; Hu, Y. X.; Guo, S. R.; Goebel, J.; Yin, Y. D. *Nano Letters* **2010**, *10*, 5037.
- (9) Zhang, Q.; Ge, J. P.; Pham, T.; Goebel, J.; Hu, Y. X.; Lu, Z.; Yin, Y. D. *Angew Chem Int Edit* **2009**, *48*, 3516.
- (10) Zhang, T.; Ge, J.; Hu, Y.; Zhang, Q.; Aloni, S.; Yin, Y. *Angew. Chem., Int. Ed.* **2008**, *47*, 5806.
- (11) Zhang, Q.; Zhang, T.; Ge, J.; Yin, Y. *Nano Lett.* **2008**, *8*, 2867.
- (12) Ge, J.; Zhang, Q.; Zhang, T.; Yin, Y. *Angew. Chem., Int. Ed.* **2008**, *47*, 8924.
- (13) Zhang, T.; Zhang, Q.; Ge, J.; Goebel, J.; Sun, M.; Yan, Y.; Liu, Y.-s.; Chang, C.; Guo, J.; Yin, Y. *J. Phys. Chem. C* **2009**, *113*, 3168.
- (14) Zhang, Q.; Wang, W.; Goebel, J.; Yin, Y. *Nano Today* **2009**, *4*, 494.
- (15) Zhang, Q.; Ge, J.; Goebel, J.; Hu, Y.; Lu, Z.; Yin, Y. *Nano Res.* **2009**, *2*, 583.
- (16) Zhang, Q.; Lee, I.; Ge, J.; Zaera, F.; Yin, Y. *Adv. Funct. Mater.* **2010**, *20*, 2201.
- (17) Zhang, Q.; Ge, J.; Goebel, J.; Hu, Y.; Sun, Y.; Yin, Y. *Adv. Mater.* **2010**, *22*, 1905.
- (18) Lee, I.; Zhang, Q.; Ge, J.; Yin, Y.; Zaera, F. *Nano Res.* **2011**, *4*, 115.
- (19) Lee, I.; Albitzer, M. A.; Zhang, Q.; Ge, J. P.; Yin, Y. D.; Zaera, F. *Phys Chem Chem Phys* **2011**, *13*, 2449.
- (20) Zhang, Q.; Lima, D. Q.; Lee, I.; Zaera, F.; Chi, M. F.; Yin, Y. D. *Angew Chem Int Edit* **2011**, *50*, 7088.

- (21) Zhang, Q.; Joo, J.-B.; Lu, Z.; Dahl, M.; Oliveira, D. Q. L.; Ye, M.; Yin, Y. *Nano Res.* **2011**, *4*, 103.
- (22) Ye, M.; Zhang, Q.; Hu, Y.; Ge, J.; Lu, Z.; He, L.; Chen, Z.; Yin, Y. *Chem.--Eur. J.* **2010**, *16*, 6243.
- (23) Joo, J. B.; Zhang, Q.; Lee, I.; Dahl, M.; Zaera, F.; Yin, Y. D. *Adv Funct Mater* **2012**, *22*, 166.
- (24) Joo, J. B.; Zhang, Q.; Dahl, M.; Lee, I.; Goebel, J.; Zaera, F.; Yin, Y. D. *Energ Environ Sci* **2012**, *5*, 6321.